Technische Universität München
Fakultät für Medizin

Iodine Concentration of Healthy Lymph Nodes of the Neck, Axilla and Groin in Dual Energy Computed Tomography

Anna Sophie Gertrud Ostmeier

Vollständiger Abdruck der von der Fakultät für Medizin der Technischen Universität München zur Erlangung des akademischen Grades einer Doktorin der Medizin genehmigten Dissertation.

Vorsitzender:	apl. Prof. Dr. Stefan Thorban
Prüfer*innen der Dissertation:	1. Prof. Dr. Daniela Pfeiffer
	2. Priv-Doz. Dr. Jonathan Nadjiri

Die Dissertation wurde am 10.01.2022 bei der Technischen Universität München eingereicht und durch die Fakultät für Medizin am 15.03.2022 angenommen.

Table of Contents

List of abbreviations

AUC : Area Under the Curve

CI : 95% Confidence Interval

CoV : Coefficient of Variation

CT : Computed Tomography

CTDI : Computed Tomography Dose Index

DICOM : Digital Imaging and Communication in Medicine

DL-DECT : Dual Layer-Dual Energy Computed Tomography

DLP : Dose-Length Product

DS-DECT : Dual Source-Dual Energy Computed Tomography

FDG : Fluorodesoxyglucose

F-FDG : F18-Fluordesoxyglucose

GFR : Glomerula Filtration Rate

Gy : Gray

HU : Hounsfield Units

keV : kilo electron Volt

kVp : kilo Volt peak

KVS-DECT : Kilo Volt Switching–Dual Energy Computed Tomography

MDCT : Multi-Detector Computed Tomography

MRI : Magnetic Resonance Imaging

PET-CT : Positron Emission Tomography - Computed Tomography

QIB : Quantitative Image Biomarker

ROC : Receiver Operating Characteristic

ROI : Region of Interest

SCAPIS : Swedish Cardiopulmonary Bioimage Study

SD : Standard Deviation

SECT : Single Energy Computed Tomography

SI : Système International, International System of Units

Sv : Sievert

TSH : Thyroid-Stimulating Hormone

Z : Atomic Number

1 Introduction

As part of the immune system, lymph nodes play a seminal role in the pathophysiology of many inflammatory and malignant diseases. Therefore, alterations in lymph nodes are of crucial diagnostic importance in clinical practice. Currently, the imaging technology of computed tomography (CT) is used to depict morphological changes of lymph nodes. A relatively new concept of CT, called Dual Energy Computed Tomography (DECT), reveals quantitative imaging parameters with in-depth information about the tissue composition which no longer dependent on any CT system, tube voltage settings, or underlying tissue HU parameters. However, the lack of empirical knowledge to utilize quantitative imaging parameters has hindered their integration into widespread clinical practice. The aim of the dissertation is to address this obstacle by introducing a possible reference value of a functional parameter provided by DECT for lymph nodes.

The following pages will investigate and discuss reference values for the iodine concentration of healthy lymph nodes of the neck, axilla and groin in DECT. The iodine originates from exogenous iodine, administered intravenously during a CT examination and its concentration is measured via an iodine map obtained through DECT. Exogenous iodine can be considered as a quantitative parameter for the level of perfusion of a lymph node at a certain time after administration. The level of perfusion may change, particularly when lymph nodes are affected by diseases that involve the immune system. In order to better differentiate healthy lymph nodes from those that are affected by a particular disease, a reference value for healthy lymph nodes is an important pre-requisite for such comparisons. This study comprises an example for an application of such a reference value, cut-off value, its validity and utility in a clinical setting.

The first part of the introduction delineates general principles of CT technology and its applications. The second part provides further background information about the development of the DECT technology and its practicality as a clinical tool. Thirdly, the physiology of lymph nodes as secondary immune organs and their appearance in CT and DECT imaging are highlighted. Lastly, the emerging concept of quantitative imaging biomarkers (QIB) is introduced along with future opportunities of iodine quantification in clinical practice.

1.1 Computed Tomography

Tomography (derived from Greek tomḗ = "cut" and gráphein = "write") is defined as an imaging process that reproduces desired objects as sectional images. The term “computed” tomography alludes data processing that reconstructs sectional images from recorded data (Hünerbein 2017). For medical applications, these sectional images can depict a patient’s anatomy at various angles in three dimensions allowing for the assessment of an organ or region of interest without obstruction from proximal structures.

CT technology is based on X-rays (see chapter 1.1.1). In 1901, W. C. Roentgen received the first physics nobel prize for the description of X-rays, paving the way for the invention of medical X-ray imaging (Kaye 1934; The Nobel Foundation). A. M. Cormack and G. N. Hounsfield further developed conventional X-ray imaging into sectional imaging and were conferred with the nobel prize in physiology or medicine in 1979 for “*The development of computer-assisted tomography*” (Hounsfield 1980; Kaye 1934; The Nobel Foundation 1979). In 1990 the introduction of a spiral CT, followed by the multi-detector CT in 2004 (see chapter 1.1.1) are key leaps in CT technology. However, already in 1976, the theoretical basis of using two X-ray beam energies in CT to enable chemical and physical analysis of pathological processes, in vivo, has been described (Rutherford, Pullan, and Isherwood 1976; Alvarez and Macovski 1976; Millner et al. 1979). The clinical implementations of the dual-energy technology has not been reached until the Dual Source CT in 2005 and the Dual Layer CT Detector in 2013 (see chapter 1.2) (Healthineers Siemens 2021). Just recently, another advancement, namely the first clinical Photon-counting Detector CT System, has been introduced in January 2021 promising further improvement of spectral data and spatial resolution (Rajendran et al. 2021).

In current clinical routine, CT enhances imaging diagnostics for tissue with a remarkable sensitivity offering deepened insight into the patient’s anatomy, physiology and pathology. CT is widely integrated into clinical routine for diagnosing, monitoring and providing a prognosis of diseases (Rubin 2014). This central role in medicine is reflected by the number of CT examinations conducted in German hospitals, rising by approximately 250.000 per year since 2005 and exceeding 6 million in 2017 (Figure 1) (Schmidt 2019).

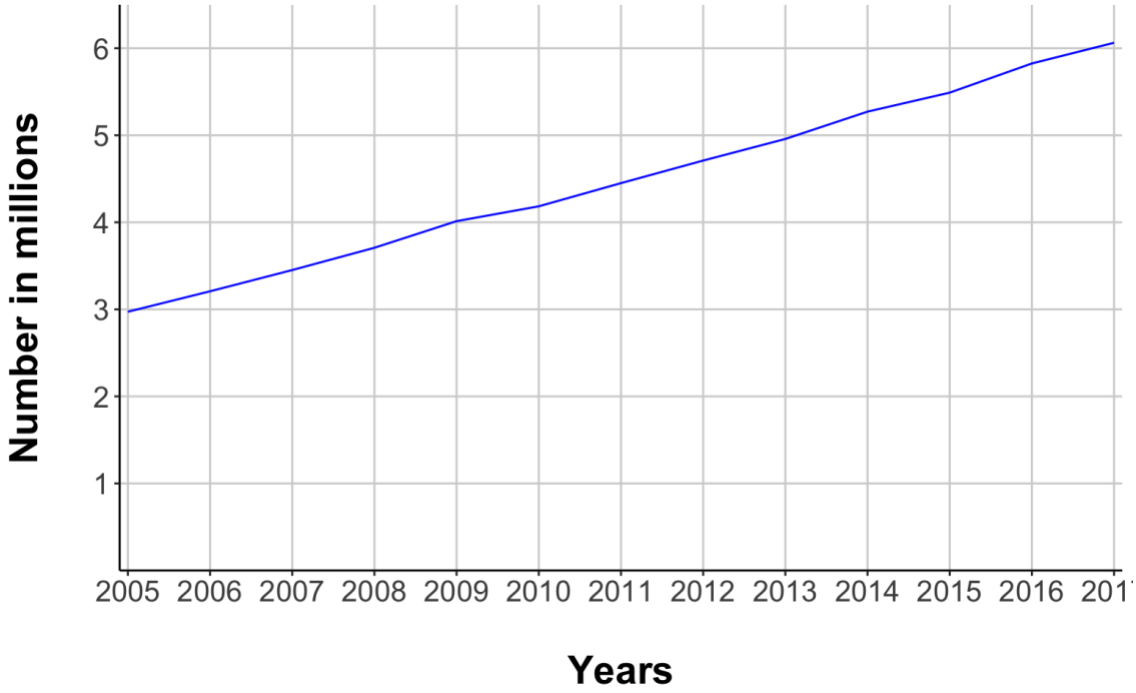

Figure 1: Number of computed tomography (CT) scan examinations conducted in hospitals in Germany from 2005 to 2017. Data set imported from statista.com (Schmidt 2019).

These numbers are justified considering the broad spectrum of medical indications for which CT can be of diagnostic value. With a high spatial and temporal resolution, CT is highly beneficial in emergency medical care, as the whole body can be scanned for various pathologies in a short time frame (3 minutes). Hence, CT is the gold standard for primary imaging of polytraumatic patients (Deutsche Gesellschaft für Unfallchirurgie 2016). Not only does emergency medical care benefit from these features of CT, but also the field of oncology applies this imaging resource to screen and stage malignant diseases, e.g. bronchial cancer, pancreatic cancer and multiple other neoplasms (Griesinger 2017; Oettle 2017). Due to the short image acquisition time, CT is advantageous particularly for advanced stage cancer patients that may have trouble to hold their breath or to keep still (Kuno et al. 2018). Furthermore, CT imaging is suitable for visualizing vascular-associated diseases, e.g. the assessment of the brain parenchyma in case of an acute stroke to differentiate between an acute brain hemorrhage and ischemia. Furthermore, CT angiography can be performed to analyze vascular pathologies such as cerebral artery aneurysm, peripheral arterial disease (Masuhr, Masuhr, and Neumann 2013; Herold 2019).

Aside from the diagnostic value of CT, the potential infliction of harm to the patient by X-rays must be considered, e.g. teratogenicity and carcinogenicity (see chapter 1.1.2). In combination with contrast agent, serious complications such as anaphylaxis, kidney failure or thyroid toxic crisis can occur (see chapter 0) (Hendee and O'Connor 2012; Chen et al. 2008). No absolute contraindications exist in a case of emergency, but due to the exposure to ionizing radiation a "justifying indication" is mandatory for every CT examination. Relative contraindications include pregnancy, young age and claustrophobia (Hünerbein 2017).

1.1.1 CT Technology

The general procedure of a CT examination starts with the patient lying on a motorized table that moves through a circular opening of a so-called gantry (Figure 2). Inside the gantry, an X-ray source is located on a ring with a digital X-ray detector on the opposite side of the source (Figure 3)(Maximilian Reiser 2017). During a CT scan, the source rotates around the patient emitting X-rays in the direction of the patient's body from 360° while the table with the patient moves through the gantry of the CT scanner. The X-ray beams are attenuated by the patient's body and registered by detectors that rotate around the patient correspondingly to the source (Figure 3). The detector transforms the incoming beams energy into an electric signal, which is further processed by a computer for CT reconstruction.

Figure 3: IQon Spectral CT. This model was used for this study. Based on (www.philips.co.uk 2017).

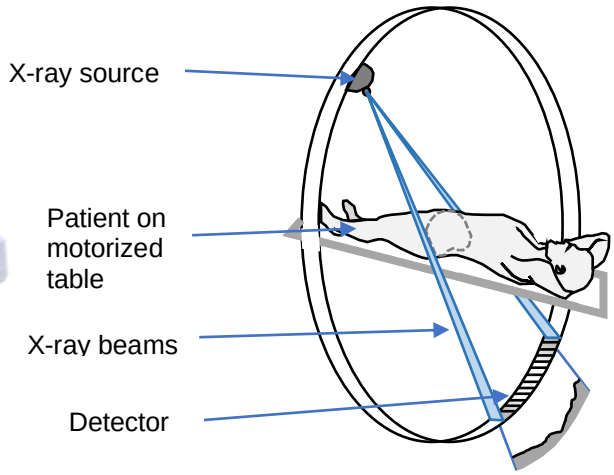

Figure 2: Image acquisition in CT. Adapted from (Maximilian Reiser 2017).

Generation of X-rays

X-rays are part of the electromagnetic spectrum and can be seen as particles – so-called photons – and electromagnetic waves at the same time (Feynman, Leighton, and Sands 1989; Purcell and Morin 2013). Electromagnetic waves are characterized by their energy, frequency, or according to their wavelength, which ranges from 10 pm to 10 nm for X-rays (Cervantes 2016). However, the overlap to gamma rays and ultraviolet radiation is continuous. Electromagnetic radiation with such extremely short wavelengths can penetrate matter, which constitutes the application of X-rays in medical imaging. Other commonly known electromagnetic waves such as radio waves or visible light are characterized by much longer wavelengths (e.g. visible light from 380 to 780 nm). The energy values of X-rays used for medical applications usually range from about 25 keV (kilo electron volt) in mammography up to 140 keV in CT (Figure 5) (Percuoco 2014).

The X-ray source technology in CT is based on an X-ray tube, which consists of an evacuated glass cylinder with two electrodes (Figure 4). The cathode is typically made from a tungsten wire, referred to as filament, while the anode is typically a rotating tungsten plate. When applying a certain heater current to the filament, shell electrons from the atom are released. The heater current is proportional to the number of electrons released over time and determines the mAs-value of the X-ray source, thus the dose (see chapter 1.1.2). With the application of an acceleration voltage – the tube voltage – between the

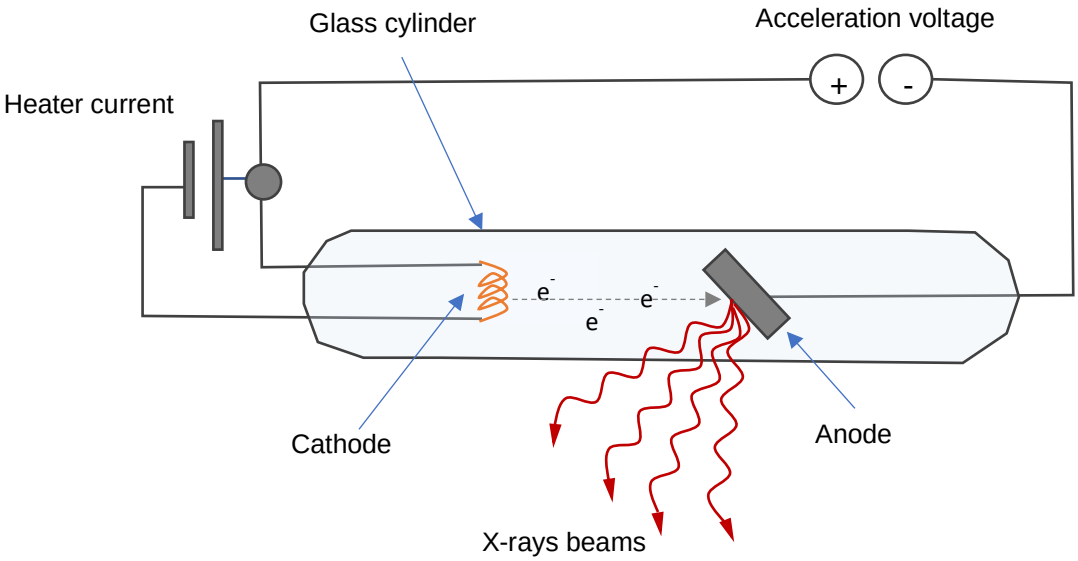

Figure 4: X-ray tube, modified, based on (Maximilian Reiser 2017; Cervantes 2016).

cathode and anode, electrons released from the cathode are accelerated towards the anode. When the electrons impact and penetrate the superficial layer of the anode, they lose kinetic energy, 99% of which is converted to thermal energy. Therefore, the anode is constructed to withstand thermal strain by implementing a rotating plate set in cooling fluid and a focal point path on the plate (Zink 1997; Flohr 2011). About 1% of the electron's kinetic energy is transformed into X-ray energy – so-called bremsstrahlung – consisting of a photon energy spectrum from 0 keV up to a maximum numerically equal to the accelerating electric potential (peak kilovoltage). Thus, the spectrum of bremsstrahlung that is released from the anode depends on the acceleration voltage and the anode's material. The acceleration voltage can be altered to produce different photon energy spectra (Figure 5, low-energy 70 kVp, high-energy 140kVp, clinical energy 120kVp). The depicted peaks in Figure 5, named characteristic material

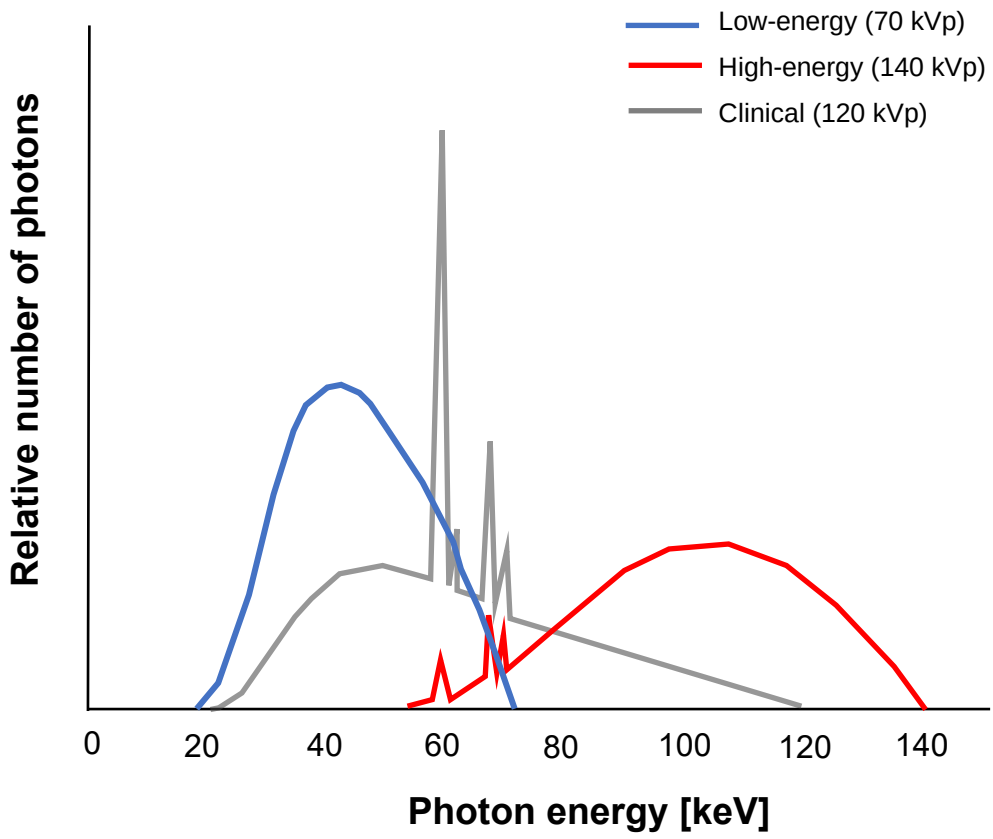

Figure 5: Schematic drawing of spectral distribution of three imaging beams in comparison. The grey line represents SECT energy spectrum most used in clinical practice. The Low-Energy and High-energy curve resemble the energy level in Dual-Energy, which is explained in chapter 1.2.1. more closely. Based on and modified from (Menten et al. 2015).

dependent lines, emerge through material-specific interaction between the incoming electron and tungsten plate (Kalender 2021).

Attenuation of X-rays

When the X-rays penetrate an irradiated object the change of intensity depends on the initial intensity of the beam, the thickness and the attenuation coefficient of the object. For monochromatic X-rays, the extant intensity of beams penetrating a homogenous object can be described with the Lambert-Beer's law (Equation 1).

$$I = I_o e^{-\mu d}$$

Equation 1: Lambert-Beer's law for the Intensity *I* of monochromatic X-rays with an initial X-ray intensity I_0 , the thickness *d* of a homogenous object and an attenuation coefficient μ .

For heterogeneous materials like the human body, the exponential of Lambert-Beer's law is expressed as a line integral, which is the sum of all attenuation in one beam direction. For diagnostic X-rays, the photoelectric effect as well as Compton scattering (Figure 8) define the attenuation coefficient μ. The differences in the attenuation coefficient from e.g., bone and soft tissue then form the contrast observed in CT images.

Detection of X-rays

Most modern CT scanners have an integrated solid-state detector. In general, a solid-state detector has three essential layers: a scintillator, photodiode and a substrate to provide the mechanical and electrical infrastructure. A scintillator is a luminescent material (e.g. $CdWO_4$ (Ronda CR 2008)) converting X-ray energy into visible light, the photodiode layer transforms the visible light into an electric current while the substrate amplifies the signal and carries the signal to analog-to-digital converters. Subsequently, the electrical signal is transmitted from the detector system to a computer (Shefer et al. 2013).

The intensity of X-ray beams that is registered by the detector in proportion to the beams emerging from the patient, reveals the geometric efficiency of the

detector, which is used when comparing generations and models of detectors (Prokop and Engelke 2007).

State of the art CT detectors include several rows of detectors (2 - 256 or more) next to each other referred to as multi-detector CT (MDCT). MDCT records more than one slice per rotation around the patient enabling faster CT examination of a greater volume. Benefits include a reduction of scan time, motion artefacts and slice thickness as well as the possibility of reconstruction in any spatial dimensions which is the basis for CT-angiography and 3D-images. The ratio of the patient table shift per detector width and slice thickness is called pitch factor which varies between CT scanners. The image quality and radiation exposure are inversely proportional to the pitch factor (Bashir and Bell 2012; Silverman, Kalender, and Hazle 2001; Maximilian Reiser 2017).

The CT scanner, IQon by Phillips, used for the present study, has a NanoPanel prism detector introduced in 2013. The technological features and its geometric efficiency are discussed in detail in Chapter 1.2..

Image reconstruction

The computer processes the detector's signal into a cross-sectional image by tomographic reconstruction. The measured intensity *I* (see chapter 1.1.1 "Attenuation of X-rays", Equation 1) is first transformed to a set of line integrals for each measured gantry rotation angle known as sinogram. There are many different reconstruction algorithms like analytical, iterative or hybrid versions, which also differ between CT manufacturers. Detailed explanation on reconstruction algorithms is beyond the scope of this thesis. For more information on CT reconstruction see e.g. (Kak and Slaney 2001; Buzug 2008; Zeng 2010).

The reconstructed image data consists of voxels. The physical voxel size is determined by the CT geometry and the detector pixel size. The contrast between the voxels is given by grey shades which depends on the extent of the attenuation of the X-rays and is contingent upon the linear attenuation coefficient μ of the investigated tissue (see chapter 1.1.1 "Attenuation of X-rays", Equation 1). Voxels of a tissue which strongly attenuates X-rays (= high μ) are shown in bright shades, conversely voxels of a tissue with low X-ray attenuation (= low μ) are displayed in darker shades. The attenuation values are calculated to Hounsfield units (HU) using water and air as reference (Equation 2):

$$\text{CT number} = \frac{\mu\,(\text{object}) - \mu\,(\text{water})}{\mu\,(\text{water}) - \mu\,(\text{air})} \times 1000\ HU$$

Equation 2: Calculation of Hounsfield units. Attenuation coefficient μ

Water is thereby defined to be 0 HU and air to be -1000 HU (Stolzmann and Götti 2011; Hünerbein 2017).

Since the human eye can only distinguish a limited number of grey shades at a time, windowing is applied to attain the desired contrast depending on the clinical question. A window setting encompasses a center and a range of HU. Voxels with HU above the window range are set to be white and below the window range black. To enhance the contrast of specific organ structures default window settings can be applied e.g. the lung window, soft tissue, or bone window (Figure 6)(Hünerbein 2017).

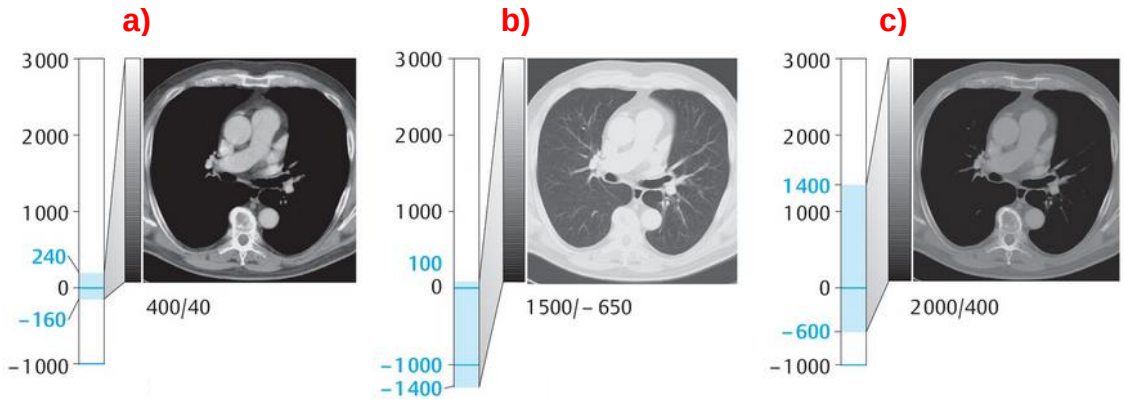

Figure 6: a) Soft tissue window, b) Lung tissue window, c) Bone window, adapted from (Hünerbein 2017).

The Hounsfield scale enables a contrast through computation of different tissue attenuation of a photon energy spectrum relative to water. Quantitative statements about the investigated tissue in HU maps are limited, contrary to DECT, as will be described in Chapter 1.4.3.

1.1.2 Radiation Exposure

As briefly mentioned in chapter 1.1.1, the patient's body is irradiated by X-ray beams during a CT examination, which is termed radiation exposure (Stolzmann 2011). As short-wave electromagnetic radiation, X-ray beams

transfer much more energy compared to visible light. The absorbed ionizing energy per mass is defined as dose. The unit of dose is Gray (Gy), which is equivalent to 1 J/kg (Bundesamt für Strahlenschutz).

Ionizing radiation inflicts a destructive effect on cells by breaking bonds and ejecting electrons from molecules within the cell (water, proteins, DNA). The resulting chemically reactive molecule type, named radicals, lead to cell damage by reacting with other molecules (Bundesamt für Strahlenschutz). In general, a distinction is drawn between deterministic and stochastic radiation damage (Bundesamt für Strahlenschutz).

Deterministic radiation damage describes direct tissue damage caused by ionizing radiation, mostly immediately after exposure. If a dose threshold is exceeded deterministic radiation damage occurs. The severity of deterministic radiation damage intensifies proportionally with increasing dose. Examples are erythema or radiation necrosis (Bundesamt für Strahlenschutz).

Stochastic radiation damage describes changes in the genetic material of cells that are caused by ionizing radiation. Stochastic radiation damage occurs with a certain probability mostly delayed by several years after exposure. The probability for stochastic radiation damage increases proportionally to the dose whereas the severity of damage itself does not correlate with the dose necessarily, in contrast to the deterministic damage mentioned above. Induction of malignant diseases such as leukemia are examples of the potential effects of stochastic radiation damage.

The extent of radiation exposure depends on the absorbed radiation dose, the type of radiation and the affected organ or body tissue. In order to estimate the radiation exposure of a CT examination, the computed tomography dose index (CTDI) is applied as the primary dose measurement concept. CTDI represents the absorbed dose of one rotation of the X-ray tube (x-y-axis) along the movement of the table (z-axis) and theoretically approximated the average dose within the scan volume (CTDIvol) in mGy. The total absorbed dose of a specific scan protocol can be further specified with the dose-length product (DLP) by multiplying CTDIvol with the scan length of the particular protocol (Equation 3) (Cynthia McCollough 2008).

$$\text{DLP (mGy x cm)} = \text{CTDIvol (mGy) x scan length (cm)}$$

Equation 3: Dose-Length Product (Cynthia McCollough 2008)

Furthermore, particular attention should be directed towards tissue-specific vulnerability to ionizing radiation. Hence, a dose needs to be weighted with a conversion factor *k*, which is specific for a part of the body. For example, abdominal CT scans have a higher dose than CT scans of the extremities and therefore referred to as the effective dose. The physical unit of the effective dose is Sievert (Sv). The effective dose of a CT examination can be calculated by multiplying DLP with the conversion factor *k* in $\frac{mSv}{mGy \times cm}$ (Cynthia McCollough 2008).

The effective dose of one CT chest exam is roughly equivalent to 4 years of natural radiation exposure and is 80 times higher than that of a chest X-ray in two planes (Bundesamt für Strahlenschutz 2016). Table 1 provides doses of typical medical imaging exams (Cynthia McCollough 2008). The average radiation exposure of a patient included in this study was estimated by a random sample and is described in the methods section (see Chapter 3.3.).

Table 1: Typical effective dose values for the CT imaging exams compared to non-CT imaging exams, mainly based on (Cynthia McCollough 2008).

CT Typical Effective Dose Values (mSv)		**Non-CT Typical Effective Dose Values (mSv)**	
Head CT	1−2	Chest radiograph	0.1−0.2
Chest CT	5−7	Mammogram	0.3−0.6
Abdomen CT	5−7	Coronary angiogram (diagnostic)	5−10
Abdomen & pelvis CT	3−4	Radiation from naturally occurring sources in Germany (Bundesamt für Strahlenschutz)	2.1

1.1.3 Contrast Agent

Typical contrast agents used for CT imaging are chemical solutions with ions of high molecular weight, e.g iodine or barium. Contrast agents are introduced in various parts of the body, e.g. orally, rectally, intrathecally or intravenously before a CT scan (Stevenson 2010; Hünerbein 2017). The contrast agent-containing body part displays with a higher level of attenuation of X-rays due to the increased density through the higher molecular weight.

Intravenous contrast agent follows the blood flow and increases the differences in density between more and less perfused tissue. For example, iodine is an element with an atomic number of 53, which is higher compared to soft tissue elements (e.g. hydrogen, carbon). Therefore, iodine atoms of the contrast agent enhance the contrast between structures with high perfusion and adjacent tissues with lower perfusion (Lusic and Grinstaff 2013). Depending on the protocol, the image is taken at certain times after the contrast agent is administered defined as a phase. Commonly used phases are the arterial phase (approximately 20 seconds after intravenous injection), when the contrast agent reaches the large arterial vessels and the portal venous phase (approximately 70 seconds after injection), when the contrast agent reaches the portal venous vein.

Different intravenous contrast agents exist for different imaging technologies and indications (Gadolinium, Iodine etc.). As mentioned before, a common contrast agent used in conventional CT imaging is iodine (Lusic and Grinstaff 2013). Modern iodine-based contrast media for intravascular application are mostly soluble in water, non-ionic, low-osmolar and have a relatively low viscosity. The elimination process involves the kidneys, to a lesser extent the intestine, the hepatobiliary system and the salivary glands (Hünerbein 2017). If an intravenous administration of iodinated contrast agent is required, the following risks must be considered and appropriate precautions must be taken (Table 2).

Possible risks and recent concerns arising from studies about the toxicity of contrast agents (Mehran, Dangas, and Weisbord 2019) need to be individually juxtaposed with diagnostic benefits mentioned above and in following chapters.

Table 2: Risks of iodine contrast agents and possible precautions to limit risks

Risks	Precautions
Acute kidney failure, deterioration in kidney function	Taking a medical history about kidney diseases, checking of creatinine or GFR level
contrast agent nephropathy	dose-dependent side effect
thyrotoxic crisis	Taking a medical history about thyroid diseases, evaluation of thyroid function with TSH level
allergic reaction	Taking a medical history about previous exposure to CT contrast agent and allergic reactions
Local infection of vein catheter	Aseptic working
Local tissue damage by vein access	Checking flow before using vein catheter to exclude leakage of contrast agent

1.1.4 Image Assessment and Clinical Report

Radiologists identify and define deviations from normal anatomy and summarize findings in a complete, structured and comprehensive clinical report. The clinical report is an essential vehicle to convey diagnostic information to the patient, physicians and potential research studies (Radiological Society of North America 2020).

The general structure of a complete report starts off with the patient's general information, principal and secondary diagnoses, clinical information, indication, technique (region, kind and amount of contrast agent) and radiation exposure (CTDI, DLP). Prior reports and images serve as a base line to the present exam in order to judge progression or remission of potential diseases.

For a neck CT with contrast agent, a clinical report would encompass aspects of the pharyngeal mucosa, oral cavity, larynx, salivary glands, thyroid, vessels, carotid space bones and cervical, supra- and partially infraclavicular lymph nodes (Radiological Society of North America 2020).

For a chest CT with contrast agent, findings of the lower neck, pulmonary parenchyma, airways processes, pleural fluid or thickening, cardiac chambers,

pericardial fluid or thickening, mediastinal processes, thoracic vascular abnormalities, pathologic osseous or soft-tissue processes and upper abdomen are included besides partially supra- and infraclavicular, sternal, mediastinal, hilar, pulmonary and axillary lymph nodes (Radiological Society of North America 2020).

For a pelvic CT with contrast agent areas investigated include the groin, reproductive organs, ureters, bladder, bowel, peritoneum, vessels, bones, iliac and inguinal lymph nodes (Radiological Society of North America 2020).

When interpreting a transverse sectional image, the observer always looks at the body's structures from a caudal direction. Thus, the viewers right side is the left side of the imaged body part and vice versa. Areas where the X-rays are attenuated relatively less by the tissue are described as hypodense. These structures appear dark (e.g. lung tissue). Areas where X-rays are attenuated relatively stronger appear bright and are described as hyperdense (e.g. bones) (see chapter 1.1.1).

1.2 Dual Energy CT Technology

The most widely used CT technology still is single energy computed tomography (SECT). SECT uses one photon energy spectrum and displays degrees of tissue attenuation relative to water using the Hounsfield scale (see chapter 1.1.1). However, materials that show similar attenuation of X-ray beams have similar HU value and can hardly be distinguished in SECT (Phan et al. 2012). Further developments of CT technology provide more detailed tissue information by utilizing two different photon energy levels (Figure 5) referred to as dual energy or spectral CT. Images types exclusively derived from DECT are virtual monoenergetic images (VMI), effective atomic number or electron density images, virtual non-contrast and material decomposition maps e.g. iodine maps (Table 3). The latter is based on the principal of two X-ray energy spectra allowing to separate attenuation shares attributed to the photon energy level-dependent photoelectric effect and Compton scattering (see chapter 1.2.1)(Alvarez and Macovski 1976). Different technical concepts of DECT are introduced in Chapter 1.2.2..

Table 3: Types of images from the detector-based spectral CT scanner, adapted from (Rassouli et al. 2017).

Image type	Mechanism of generation	Clinical uses
Conventional (routine diagnostic)	Data from both layers considered as a single detector	Routine diagnostic use for all cases
Iodine density (iodine map)	Material decomposition with pixels representing iodine	Visualization and quantification of iodine in vessels and organs of interest
Virtual non-contrast	Material decomposition and removal of iodine containing pixels	Characterization of lesions such as renal cysts/masses, adrenal nodules, lung nodules, etc. Radiation dose saving by eliminating need for true non-contrast
Uric acid pair	Material decomposition; depiction of pixels containing uric acid	Urinary calculus characterization
Effective atomic number	Material decomposition; color coding depending on atomic number	Tissue characterization
Virtual monoenergetic	Linear combination of basic pair images (40–200 keV)	Low monoenergetic: enhanced vascular contrast High monoenergetic: decreased artefacts
Equivalent monoenergetic	Linear combination of basic pair, with attenuation values equivalent to conventional images	Higher image quality, with lower noise

1.2.1 Basic Principles of Material Decomposition in DECT

The input of attenuation values from two photon energy spectra enables the calculation of material decomposition maps. Energy-related attenuation characteristics focus on the interactions between photons and tissue, which depend on the incident beam energy, the mass density and atomic number of the absorber, e.g. a patient's body (Patino et al. 2016). The atomic number is defined as the number of protons in the nucleus of an atom of a given element and corresponds to the number of electrons surrounding the nucleus. Within photon energy spectra used in clinical CT imaging (70-140 kVp), the types of interactions between photons and tissue are Compton scattering, predominantly at higher photon energy levels and the photoelectric effect at lower photon energy levels (Figure 7) (Patino et al. 2016). Both together constitute nearly the total attenuation at the respective photon energy level. The shares of the Compton effect and the photoelectric effect can be computed generating the spectral basis images (also see Figure 7) (Rassouli et al. 2017).

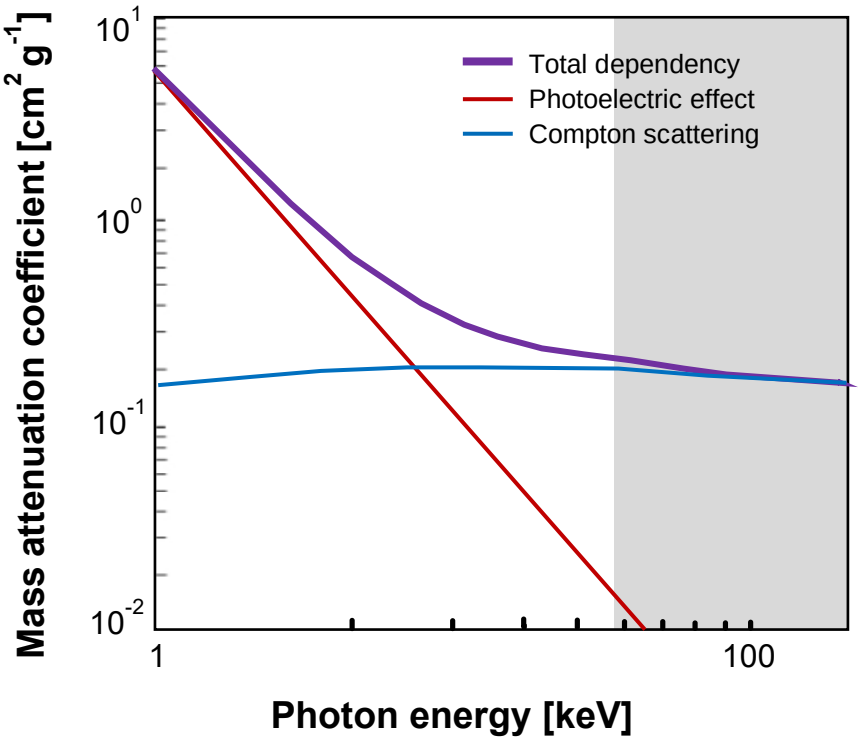

Figure 7: Energy dependence of the mass attenuation coefficient in soft tissue (example muscle tissue). For lower photon energies, the photoelectric effect is a more prominent interaction type. The grey area approximates the photon energy range, which is used in clinical imaging. Modified, based on (Kieranmaher 2001)

The Compton effect is described as the transfer of energy from a photon to an electron, that results in a decrease of energy and a change in the direction of the photon (Figure 8: a)). This inelastic scattering process is proportional to the atomic number, but less affected by the original energy of the photon (Figure 7: horizontal blue line).

The photoelectric effect refers to the ejection of an electron from the innermost shell of an atom (the K-shell) in case a photon transmits a greater energy amount than the binding energy of the K-shell (K-edge). The energy needed to liberate the electron from its K-shell is specific to the element's atomic number (Z). The residual photon energy transfers to kinetic energy of the ejected electron. At a specific energy level, the incoming photon is fully absorbed by the electron, which results in an abrupt increase of attenuation (Figure 8: b), Figure 9: "iodine K-edge")(Danad et al. 2015). Subsequently, the photoelectric effect depends on both the individual energy of the photon and the unique K-shell energy of the electron, thus the atomic number.

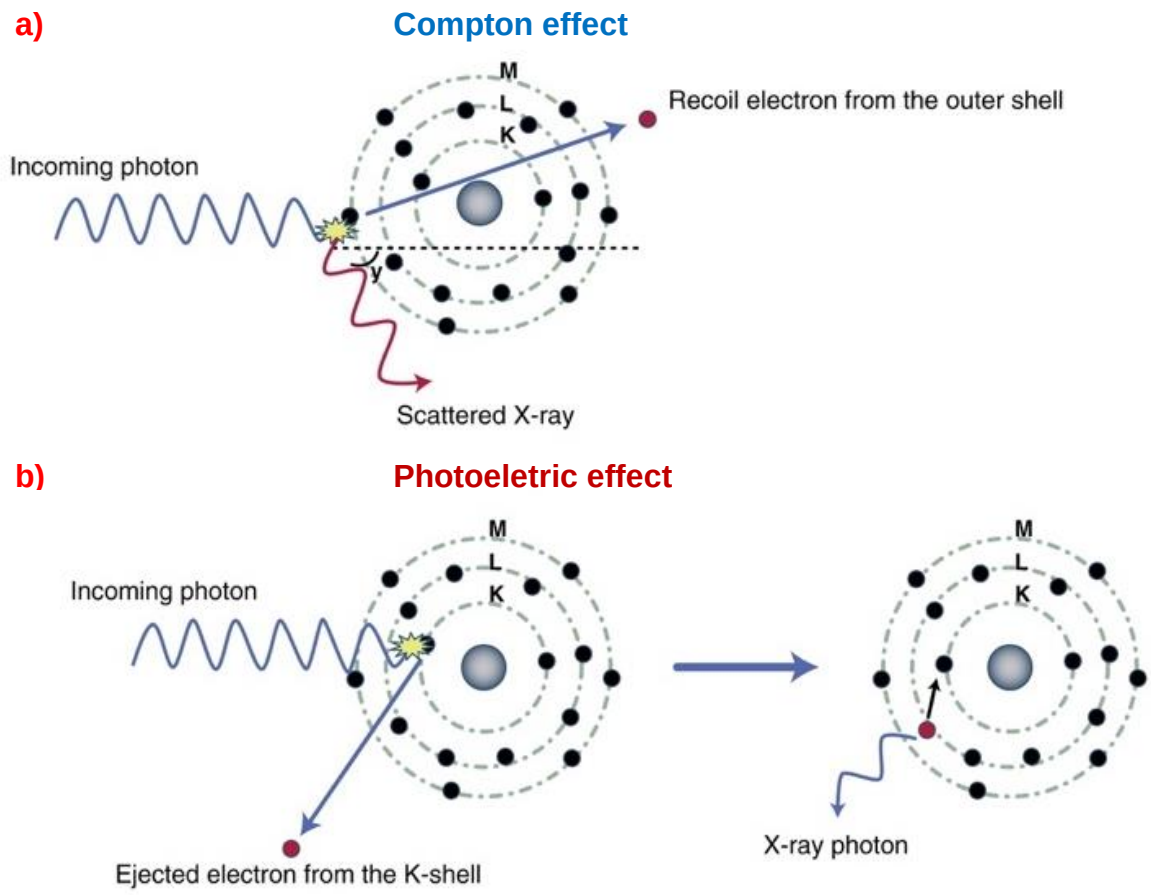

Figure 8: Schematic illustration of the two prominent types of interactions between photons and atoms of the tissue attenuating the X-ray beams a) Compton effect and b) photoelectric effect. Adapted from (Danad et al. 2015).

The principles of DECT extensively draw upon the photoelectric effect, because of its dependency on the incoming photon energy. In a more general sense, the exposure to two different energy levels unveils unique energy-related attenuation characteristics of a material according to their effective atomic number and mass attenuation coefficient as a prerequisite to decompose elements within the tissue (Alvarez and Macovski 1976; Danad et al. 2015).

Material decomposition algorithms identify the object's chemical composition by using two approaches: the two-material decomposition in projection data (pre-reconstruction) and the three-material decomposition in the image-space data (post-reconstruction). For the two-material decomposition, a pair of materials with known dissimilar energy-related attenuation is chosen (e.g. iodine and water, Figure 9).

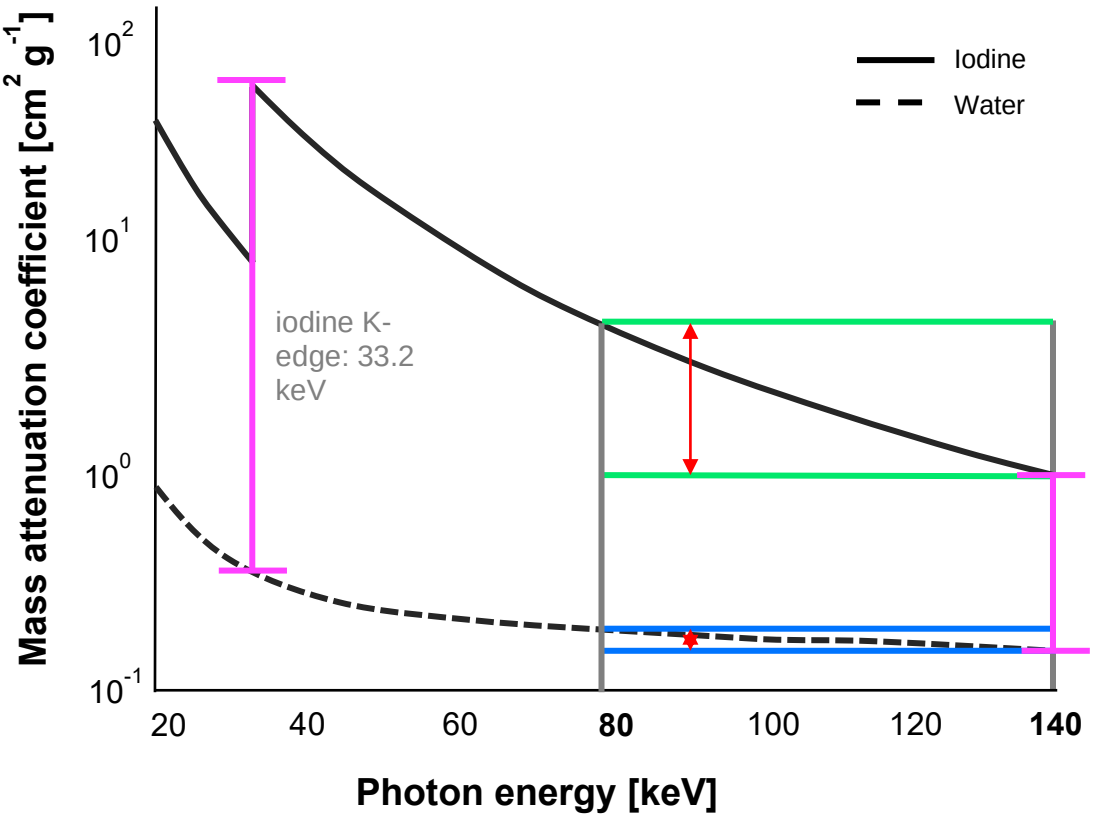

Figure 9: Mass attenuation coefficients of iodine (black line) and water (dashed line) as a function of energy. Differences in attenuation are greater at lower energies, as the photon energy approaches the unique binding energy (iodine k-edge) of each material (pink lines). The green lines mark the difference of mass attenuation coefficients for iodine at photon energy levels of 80 and 140 keV compared to the much smaller difference for water (blue lines). Modified, based on (Burton, Cunningham, and Mayo 2015).

The two materials can be randomly selected, as long as the difference of their atomic number and corresponding K-edge is sufficient enough. For example, soft tissue mostly consists of hydrogen, oxygen, carbon and nitrogen with lower atomic numbers (Z < 10) compared to calcium and exogenously administered materials such as barium, iodinated contrast agent and gadolinium with higher atomic numbers (Z < 50) (Kuhn and Klapötke 2014). The elementary dissimilarity between the basis pair materials defines their energy-related attenuation behavior. The desired mass fraction of both materials in a voxel can be mathematically identified with an algorithm that approximates the integral of the measured linear attenuation coefficients. Inserting the precomputed mass-attenuation coefficient and atomic number the algorithm can be solved for the mass fraction (Alvarez and Macovski 1976). Every other third material's mass fraction with a different attenuation behavior in the investigated voxel (Figure 10: turquoise line) is seen as a combination of the selected basis pair materials (Figure 10: blue and green lines) (Danad et al. 2015).

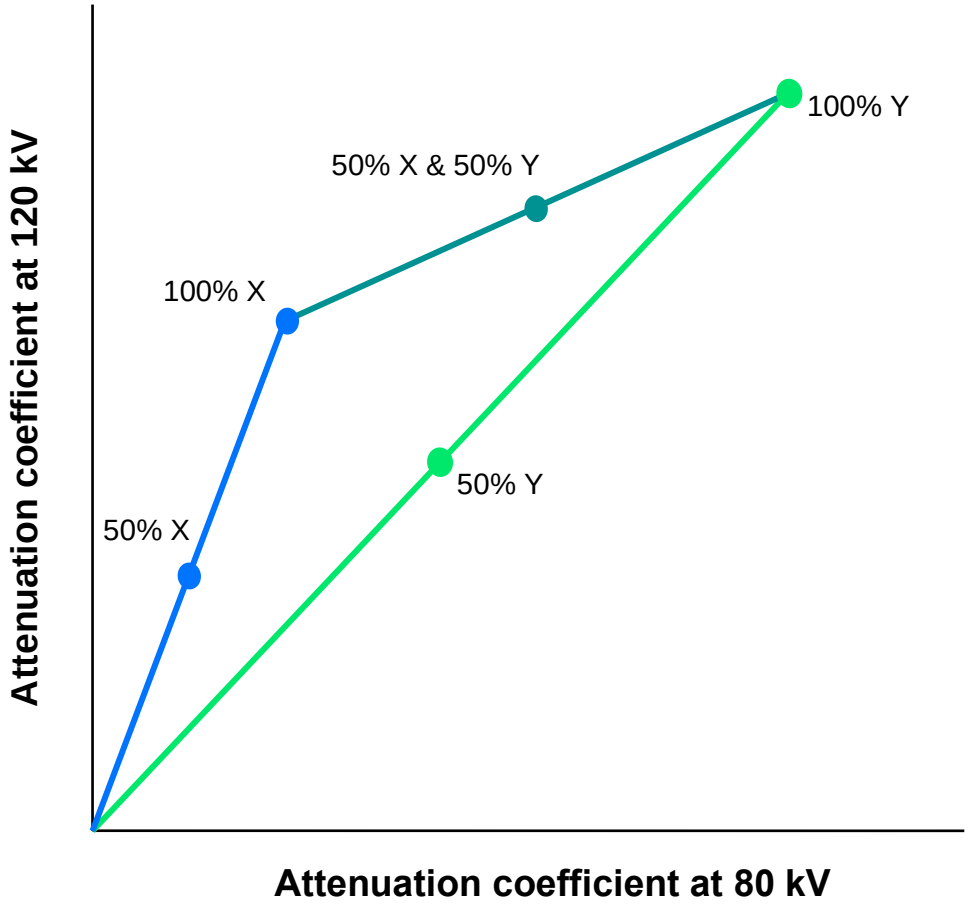

Figure 11: Linear attenuation coefficients of materials X e.g. water (blue line) and Y e.g. iodine (green line) and combination of materials X + Y (turquoise line). Modified, based on (Danad et al. 2015).

For three-material decomposition, the algorithm needs to be solved for another mass fraction, which initially seems to be an unsolvable problem with only two measurements obtained at high and low energy levels for in total three unknowns. However, by incorporating additional information, such as physical constraints, the algorithm can still be solved for three mass fractions. Supporting physical constraints are the mass or volume conservation, i.e. the third component can be calculated knowing the total mass or volume, respectively (Liu et al. 2009). Therefore, the third fraction of a particular material (e.g. iodine) other than the basis pair materials can be selectively calculated (Marin et al. 2014).

DECT provides the spectral differentiation of attenuation data and can provide the concentration of iodine in a voxel regardless of the inherent attenuation, which SECT is not capable of (Liu et al. 2009). Furthermore, the iodine map can be subtracted from the total attenuation image and virtual non-contrast images can be rendered (see Figure 12). Advanced concepts and algorithms facilitate the characterization of complex substances, such as uric acid, fat and different constituents of kidney stones (Patino et al. 2016). The technique of iodine image generation and the extraction of the iodine concentration within a region of interest (ROI) will be explained more closely for detector based DECT, which is relevant to the understanding of the present study (Chapter 1.2.2).

1.2.2 Technical Realization of Dual Energy Principal

In order to provide two photon energy spectra in clinical application, the following three practical concepts of DECT technology are most commonly used (Figure 12). The promising concept of photon counting CT detector with its intrinsic spectral sensitivity has only been freshly implemented in 2021 (Healthineers Siemens 2021). Apart from clinical applications, DECT is likely to emerge in material science (Patino et al. 2016; Sellerer et al. 2019).

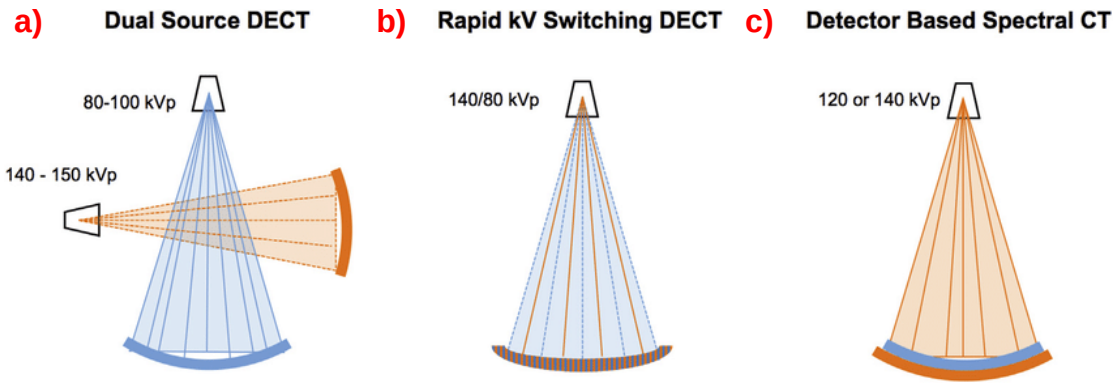

Figure 12: a) Dual source DECT (DS-DECT) includes two X-ray sources with different photon energy levels and two corresponding detectors for each source. b) Rapid kV switching DECT uses one X-ray tube and one detector with a rapid alteration between high and low tube voltage (KVS-DECT). c) Detector based spectral DECT or dual-layer DECT (DL-DECT) uses one X-ray source with a constant photon energy level but a sandwich or dual layer detector that distinguishes between high and low energy levels of incoming photons. Based on (Grajo and Sahani 2018).

Table 4 comprises advantages and disadvantages of the different practical DECT concepts in clinical use.

Table 4: Advantages and limitations of DECT concepts. Modified, based on (Patino et al. 2016).

	Advantages	**Disadvantages**
DS-DECT	- Enhanced contrast-to-noise ratios in material-specific images because of better separation between two energy spectra - Ability to alter voltage of low energy tube (80-100 kV) for examination in large patients - Decreased rotation time, enhancing sharpness of images especially in cardiological questions	- Variation between high and low energy data due to the difference in angles (90°-95°) - Requirement of specialized scatter correction, simultaneous emission of beams leads to scattered photons registered by the detector designed for the photons of the other tube
KVS-DECT	- More simultaneous acquisition of the high- and low-energy dataset	- High overlap of the energy spectra
DL-DECT	- Acquisition of the high- and low-energy datasets at the exact same time - Generation of material-specific imaging from all image datasets regardless of the scanning protocol - No additional imaging dose compared to a conventional scan - No restrictions related to field of view, gantry rotation time or cross-scatter	- High overlap of the energy spectra

As shortly mentioned in Chapter 1.1.1, the IQon Scanner manufactured by PHILIPS Healthcare and used in the present study incorporates a DL-DECT concept (Figure 12 c)), which is premised on a detector with two optically separated solid-state scintillator layers that are read by a photodiode on the side. The so-called NanoPanel prism detector contains a top layer made of yttrium-based garnet and a bottom layer made of gadolinium-oxysulphide. High- and low-energy photons reaching the detector are detected simultaneously. However, low-energy photons are registered by the top layer and high-energy photons by the bottom layer (Grajo and Sahani 2018). The detector thickness, distance and geometric efficiency are comparable if not superior to SECT detectors (Rassouli et al. 2017; Grajo and Sahani 2018; Romman et al.).

Subsequently, DL-DECT can offer spectral image data on demand according to clinical desideratum, enhanced image quality and no change in workflow. The ability to provide both conventional and spectral images in the same scan using a standard protocol rests on the retrospective distinction between the two energy levels, contrary to DS-DECT and KVS-DECT (Figure 12, Table 4). A prospective distinction requires selecting patients who need DECT and altering protocols beforehand (Romman et al. 2014).

The combined data of both photon energy levels forms the basis for the generation of conventional HU images. For material decomposition, a high and low energy data input is imperative, as described in Chapter 1.2.1. The quantification of iodine in vessels and organs are exclusively derived from iodine-only images, which represents the basis of the present study. Voxels containing iodine appear bright, whereas voxels lacking iodine appear dark. The concentration of iodine within a voxel is expressed in mg/ml (Rassouli et al. 2017). To measure the average iodine concentration within a ROI, a circle is placed on the iodine image at the tissue of interest. The iodine concentration of the marked space within the projection is displayed underneath (see chapter 3.4.1, Figure 19).

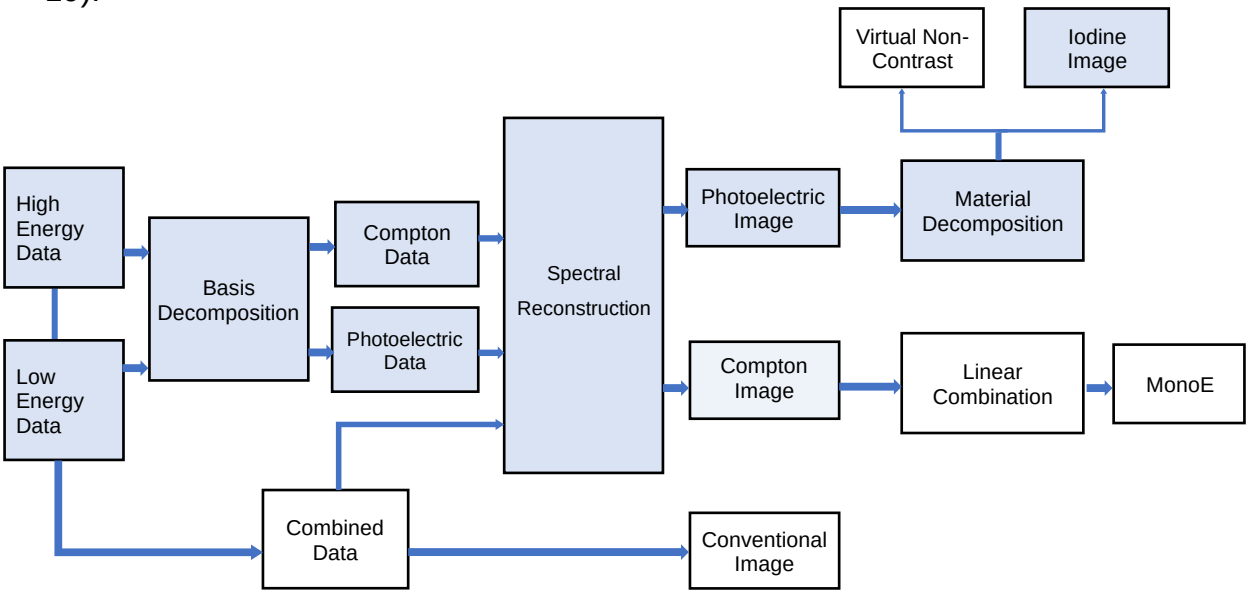

Figure 13: Flowchart showing the technique detector DL-DECT image generation (see Chapter 1.2.2). The blue colored squares are most relevant for the iodine map from which the iodine concentration of the present study is extracted. MonoE = equivalent monoenergetic image. Modified, based on (Rassouli et al. 2017).

1.3 Investigation of Lymph Nodes

The main subject of this study is the investigation of the iodine concentration for healthy cervical, axillary and groin lymph nodes in DECT. The human body contains an estimated number of 600 lymph nodes, present in various parts of the body (Figure 20) (Ghirardelli, Jemos, and Gobbi 1999). As secondary lymphoid organs, lymph nodes filter the lymph of the body and initiate a specific immune defense, in which lymphocytes are activated as part of the regular immune response (Willard-Mack 2006).

1.3.1 Physiological Morphology of Lymph Nodes

The macroscopy of a lymph node is described as a bean-like shape. The draining lymphatic vessel (*vas efferens*) as well as the supplying and draining blood vessels are located at the concave side. On the opposite convex side the afferent lymphatic vessels (*vasa afferentia*) enter a lymph node (Figure 13) (Lüllmann-Rauch and Asan 2019; Bélisle and Sainte-Marie 1981).

The microscopic structure includes the capsule, subcapsular sinus, cortex (B cell zone with follicles and germinal centers), paracortex (T cell zone), medullary sinuses, medullary cords and hilus (Figure 13) (Elmore 2006). The short axis diameter of a normal lymph node varies between 5-10 mm (Hansen et al. 2018).

The blood enters the lymph node via *vas afferens* at the hilus. Inside the medulla, the blood vessels fan out into medullary arteries. Beyond the corticomedullary junction, arterioles and a dense capillary network are located within the paracortex and peripheral cortex. An article from Jafarnejad et al. presented results from MicroCT imaging showing that these peripheral capillaries of lymph nodes in mice make up for 75% of the blood vessel surface, which suggests the paracortex and peripheral cortex to be the area of highest perfusion within a lymph node (Jafarnejad et al. 2015). After the transfer of oxygen, the blood flows from the capillary network over the high endothelial and corticomedullary venules into the *vas efferens* and exits the lymph node at the hilus (Willard-Mack 2006; Semeraro and Davies 1986; Jafarnejad et al. 2019; Bélisle and Sainte-Marie 1990).

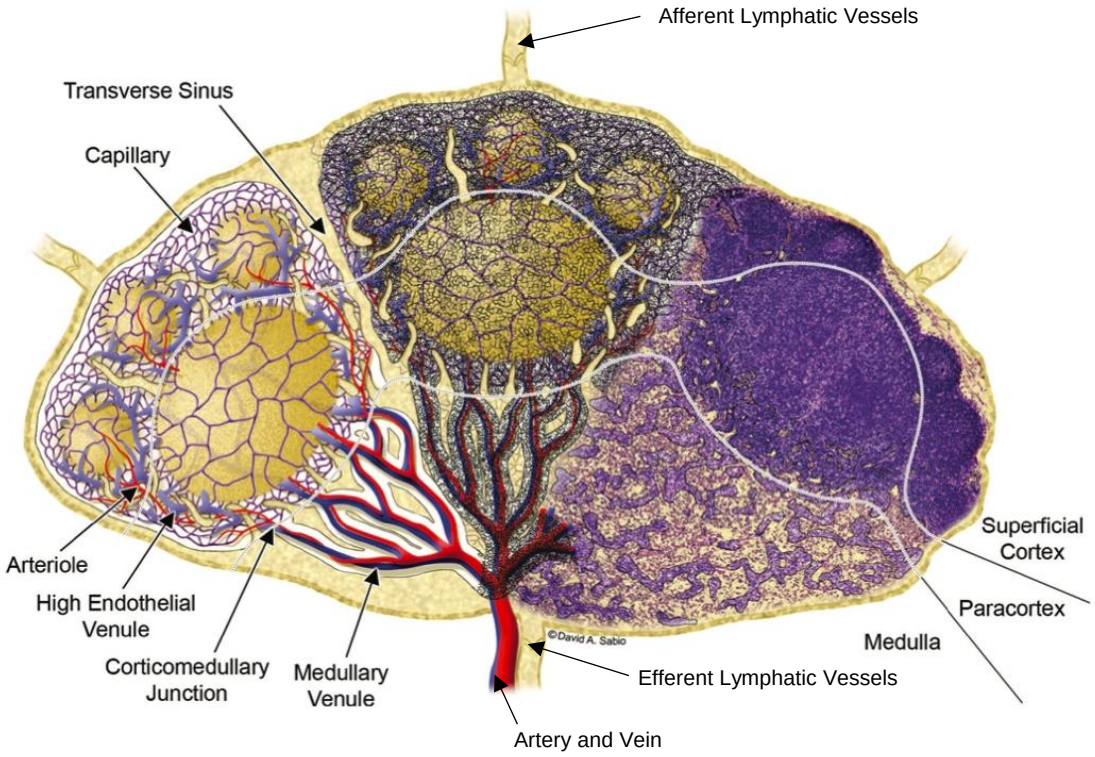

Figure 14: Detailed illustration of a midsagittal lymph node slice and its internal structure with a focus on vessel distribution. Left lobe: schema of arterioles and venides, center lobe: reticular meshwork superimposed on the vasculature, right lobe: appearance in histological section. Adapted from (Willard-Mack 2006).

Administered intravenously iodine follows the bloodstream as described above and visualizes the degree of perfusion within the lymph node depending on the blood vessel surface and the phase of the scan. In the portal venous phase contrast opacification of the majority of the solid abdominal organs is near optimal (Alkadhi et al. 2011). Therefore, the mass concentration of iodine and attenuation of x-ray beams is highest in the outer region of a normal lymph node. Therefore, the appearance of a normal lymph node in CT in the portal venous phase can be deduced (Figure 14).

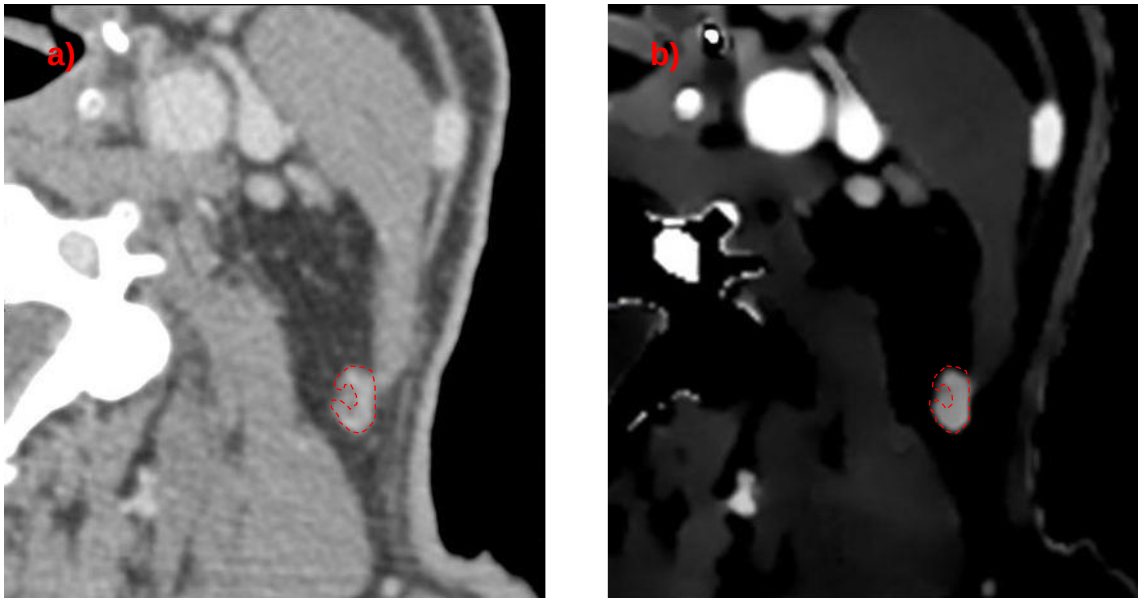

Figure 15: a) CT image of morphological unobtrusive lymph node subauricular on the left side (red dashed line) with HU b) with iodine concentration map. The bright area represents a high uptake of iodine congruent with the microanatomical dens capillary net in the peripheral part (Willard-Mack 2006; Bélisle and Sainte-Marie 1990).

1.3.2 Pathological Morphology of Lymph Nodes

In response to immunological stimuli such as an infection or autoimmune disease, the blood and lymph flow can increase approximately 25-fold. The proliferation and differentiation of lymphocytes cause morphological change of the anatomy of lymph nodes that can increase the size of the lymph nodes approximately 15 times (Ghirardelli, Jemos, and Gobbi 1999). Besides immunological stimuli, malignant diseases with spreading of tumor cells, their filtration and unregulated proliferation in lymph nodes alter the anatomy and perfusion parameters. Therefore, the description of the morphological change of lymph nodes is essential for a precise diagnosis of a disease and its stage in an assessment of a CT scan (Tawfik et al. 2014). A commonly used parameter in CT for abnormalities represents the lymph node's size. Lymph nodes with a short axis diameter > 10 mm and a long axis diameter > 15 mm arranged in conglomerates are likely to be part of a pathological process (Dorfman et al. 1991; Hansen et al. 2018; Eisenhauer et al. 2009). Additionally, internal heterogeneity and irregularity of the border are additional morphological parameters potentially indicating pathological processes (Rollvén et al. 2017).

Possible differential diagnoses of morphologically changed lymph nodes include infectious, immunologic and endocrine diseases as well as cancer or lymphoproliferative diseases (Uptodate “lymphadenopathy” 2019). Besides healthy lymph nodes, the present study investigates lymph nodes affected by lymphomata to test a potential clinical application of the reference values.

The estimated incidence of lymphomata in Germany has been approximately 25 per 100.000 inhabitants in 2014 (Koch-Institut 2017). As an imaging device, CT plays a major role for the initial and follow-up staging of lymphoma patients. Not only the short duration of a CT examination (approximately 3 minutes) but also the high contrast to the surrounding tissue of lymph nodes, underlines the clinical practicability for lymphoma patients (Herold 2019; Mugnaini and Ghosh 2016).

Lymph nodes affected by lymphomata typically loose the beans-like shape and assume a roundish form (Figure 15). The space-filling disproportional proliferation of lymphocytes eventually leads to a macroanatomic expansion and microanatomic homogenous cell clusters possibly conveying necrosis. Hence, the ordered structure and distribution of capillary vessels is disturbed. Accordingly, besides expected difference in HU values, altered behavior of iodine uptake seems plausible as well. A deviation in iodine concentration might be a more sensitive parameter to detect microanatomical changes before a detectable

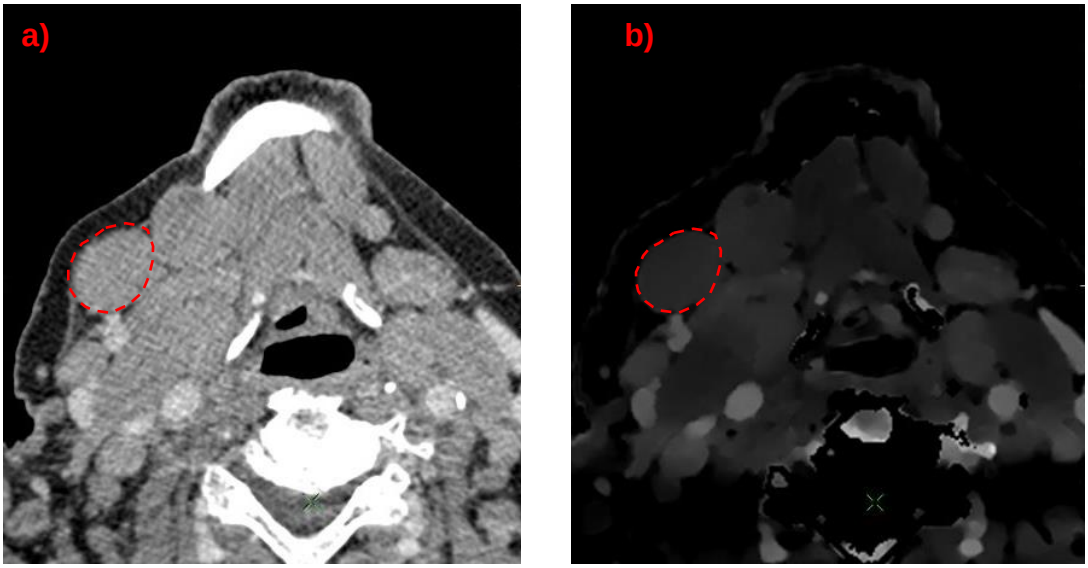

Figure 16: a) CT image in venous portal phase of pathological lymph node submandibular to the right in Hounsfield scale, primary diagnosis of a lymphoma b) Corresponding iodine concentration map.

change in HU or macroanatomy of the lymph node occurs. Several previous studies investigated DECT's clinical usefulness for imaging to discriminate lymph nodes affected by lymphoma (Yang et al. 2016; Seidler et al. 2019; Martin et al. 2018).

1.3.3 Investigated Regions: Neck, Axilla, Groin

The regions of lymph nodes investigated in the present study constitute lymph collection stations from major parts of the body.

Lymph nodes of the neck receive lymph fluid from the head. Frequent changes of lymph nodes of the neck occur due to local inflammation of the mouth, throat and ear or without any detectable cause. A typical location to suspect malignancy is supraclavicular, however, lymph nodes in all anatomical levels of the neck can be affected by lymphoma or metastatic disease. Oxygenated blood for the neck is mostly provided by the common and external carotid artery and the thyrocervical truncus. The venous outflow takes place via jugular veins (Aumüller et al. 2020).

Axillary lymph nodes are relevant for the drainage of lymph fluid from the arms and, partially, the chest wall. Lymph node swelling within this area is often associated with lymph node metastasis of breast cancer or more rarely, with local infections, e.g. erysipelas. The blood supply originates from the subclavian vessels (Aumüller et al. 2020).

Lymph nodes of the groin take over the lymph fluid of the legs and of the external genitalia (excluding testicles). Therefore, local infections of the lower limbs, sexually transmitted diseases such as syphilis or genital herpes may cause enlargement of the lymph nodes as well as squamous cell cancer of the penis or vagina or anal cancer. The blood supply derives from the abdominal aorta. Down the flow, the abdominal aorta divides into the right and left common iliac artery. The iliac veins are located next to the aforementioned arteries and drain into the inferior vena cava (Aumüller et al. 2020; Herold 2019).

Lymph nodes of the neck, axilla and groin are categorized as superficial, peripheral and palpable. A difference in the internal distribution of blood vessels between superficial and deep lymph nodes has scarcely been investigated so far (Semeraro and Davies 1986).

1.4 Quantitative Imaging Biomarkers and Reference Values

1.4.1 General Concept of Quantitative Imaging Biomarkers and Reference Values

In the past two decades technological innovations have fostered the possibility to objectively measure characteristics *"from an in vivo image as an indicator of normal biological process, pathogenic process, or response to a therapeutic intervention*" conceptionally similar to a laboratory assay which is referred to as QIB. The popularity of QIB blends into the general trend towards precision medicine which offers patients individualized treatment options through meticulous diagnostics up to a molecular level (Sullivan et al. 2015).

To reach the level of clinical usefulness that is evaluated by the benefit for a patient outcome, an interdisciplinary approach and statistical standards for QIBs' discovery and validation must be followed (Poste 2011). Firstly, a QIB needs to be closely linked to the presence of the target disease or condition and secondly a QIB's measurement need to be accurate, reproducible and feasible over time (Prescott 2013).

Mathematically, a QIB can only be a ratio or an interval variable. A ratio variable encompasses a clear definition of zero, such as the iodine concentration in DECT. An interval variable would have a meaningful difference between two values, but is missing a clear definition of zero, such as the Hounsfield scale. Furthermore, a QIB only approximate towards the true value because the truth for in vivo imaging in clinical setting is more of a philosophical expression even with surgery or autopsy confirmation of disease measurements as any kind of measurement entails an error. A common substitute for a true value is generally accepted to be the mean of a large number of replicates with a suitable small measurement uncertainty known as a reference value. Obtaining such a reference value is hampered by limitations and expenses of imaging subjects' multiple times which may pragmatically be overcome by digital or phantom studies. Measurements of digital or physical phantoms demonstrate high repeatability being suitable for the evaluation of the technical performance, however, fail to comply with all characteristics of a human target and can overestimate technical precision. Clinical studies, on the contrary, may prove reproducibility helping to establish clinical validation but cannot offer identical conditions for multiple repetitions and face sources of inherent variability such as

characteristics of living tissue. For both, technical performance and clinical validation the thorough disclosure of the methodical framework, in which a reference value is obtained, is fundamental for physicians' judgement of clinical applicability (Sullivan et al. 2015).

Methods to utilize QIBs in form of reference values are often conceptualized as cut-off points or thresholds for clinical decision-making with diagnostic accuracy varying in sensitivity and specificity which are basic parameters of the contingency table. While the sensitivity describes the thresholds' ability to correctly detect pathogenic processes, the specificity relates to the correct categorization of normal biological processes. The relationship between the sensitivity and specificity is commonly visualized as Receiver Operating Characteristic (ROC) curve. The curves integral, named area under the curve (AUC), quantifies the discriminative validity of the threshold from 0 to 1 with 1 being the optimal value. (Hilgers et al. 2013). Further mathematical parameters to quantify technical performance and clinical validation of QIBs is beyond the scope of this dissertation and can be found in (Sullivan et al. 2015).

1.4.2 Normalization

In general, normalization implies a process to conform something to a similar scale making samples more comparable (Yang et al. 2020; Välikangas, Suomi, and Elo 2016). The term "normalization" has a widespread usage across biomedical, computer and economical science. In literature, principal concepts of normalization methods for QIBs are scarcely described. However, a proper normalization method can be a pivotal task for the reliability of the downstream analysis and results.

1.4.3 Opportunities for Iodine Quantification with DECT as a quantitative imaging biomarker

The potential of material decomposition and quantification of iodine uptake with DECT as a QIB is not fully elucidated. The assessment of spectral imaging data is still rarely integrated in clinical practice at present (George et al. 2017). However, multiple clinical applications, as mentioned in the previous chapters and Table 3, indicate promising diagnostic benefits of DECT.

Drawing the line between previous explanations of DECT material decomposition, lymph nodes and iodine contrast agent, exogenous iodine can

serve as a contrast agent and as a kind of a tracer as its quantification yields accurate information about the level of perfusion (Lennartz, Abdullayev, et al. 2019). DL-DECT technology allows to differentiate between soft tissue and exogenous iodine precisely (Van Hedent et al. 2020). In SECT, values of a ROI might be measured before and after the administration of contrast agents in order to obtain functional information about the perfusion indirectly through the change in total density. One example of a threshold-based assessment is to categorize adrenal masses in adenomas and nonadenomas with an attenuation value of 10 HU or less in combination with a percentage enhancement washout above 60% being typical for adenomas (Caoili et al. 2002). Studies have even shown a similar specificity of SECT compared to PET-CT regarding functional imaging information (Nakagawa, Yamada, and Suzuki 2008; Ng et al. 2005). However, the difference in total density expressed in HU is difficult to compare with other patients or with different exams of the same patient because the HU scale is calibrated to the baseline attenuation value within one exam respectively. Furthermore, the difference in total density could also be confounded by other inherent elements with high atomic numbers e.g. calcium. DECT, with its feature to reveal ratio values of the contrast agent uptake, does not need to rely on the Hounsfield scale, exclusively. Iodine quantification could become a QIB that provides an accurate metric of differences in perfusion between different pathologies because of a lower probability to be affected by confounding factors that alter attenuation depicted in HU (Martin et al. 2018; Al-Najami et al. 2017). The specified unit of iodine concentration in DECT is mg/ml which is transferable to the International System of Units (SI). A reference range for exogenous iodine uptake of healthy tissue in SI units, similar to a laboratory parameter, seems to be favorable QIB comparable between patients. A reference range can be characterized as a basis for increased CT data comparability (Stedman's 2011). In accordance with the latter reasoning, the concept of iodine quantification could enhance the radiologist’s detection for various diseases (

Table **5**).

Over the last couple of years, several studies investigated iodine quantification for the evaluation of complex cystic renal disease, incidental adrenal nodules, the differentiation between intrapulmonary and primary tumors, staging and monitoring of treatment response of gastrointestinal tumors (Ascenti et al. 2012; Mileto et al. 2014a; Deniffel et al. 2019; Iwano et al. 2015; Xu et al.

2020; Lennartz, Le Blanc, et al. 2019). Following this trend, iodine quantification seems especially suitable for oncological diagnosis and staging by differentiating between malignant and healthy tissue or predicting treatment response (Simons, Kachelriess, and Schlemmer 2014; Zopfs et al. 2020). Furthermore, features such as improving vascular contrast and lesion conspicuity, decreasing artefacts and radiation exposure represent promising benefits of DECT (Albrecht et al. 2018).

Table 5: Variety of possible applications of iodine quantification in DECT in a clinical setting. Based on Patino et al. 2016.

Region	Iodine
Head, Neck, cerebrovascular (Hsu et al. 2016; Rajiah 2019; Odisio et al. 2018)	Hemorrhage vs contrast-medium extravasation, intracranial hemorrhage of unknown etiology, tumorous invasion of cartilaginous structure
Chest (Albrecht et al. 2018)	Pulmonary perfusion, pulmonary emboli, pulmonary nodules
Abdomen (George et al. 2017; Schmidt et al. 2018)	Lesion detection and characterization, tumor staging, metal-related artifact reduction, fibrosis
Lymph nodes (Liu et al. 2015; Martin et al. 2018; Yang et al. 2016)	Differentiation between benign or malignant process
Musculoskeletal (Carotti et al. 2019; Fukuda et al. 2017)	Inflammatory arthritis, improvement of arthrography, bone density

Current clinical trials tap into new fields to apply DECT, for example the comparison of *“the value of DECT to an invasive diagnostic needle Aspiration”* for gout (NCT03038386) or the diagnostic values of DECT for “*Solid Organ Cancer With Intracranial Metastasis*” (NCT03685539) (U.S. National library of Medicine).

2 Objectives

2.1 Current In-Clinic Situation: Assessment of Lymph Nodes

Lymph nodes can be examined in many different ways which vary in sensitivity, specificity and the respective indication.

Palpation of lymph nodes is part of a standard physical examination, a straightforward technique to screen for pathologies of superficial lymph nodes. Possible findings are categorized in painfulness, consistency, flexibility, appearance and progress that can point to either a benign or malignant process. Additionally, blood tests, such as inflammation parameters or serological testing for various types of infections, can narrow differential diagnosis for enlarged lymph nodes.

Ultrasound is another examination technique for suspect lymph nodes requiring little effort. Since ultrasounds are sound waves, no potential harm or side effects have been reported so far. Among the imaging techniques ultrasound is safe, the least expensive and widely accessible (Buscarini, Lutz et al. 2013). The suspect lymph node's size with long to short axis ratio, shape, contour, vascularity, internal architecture, including echotexture of the hilum, cystic/necrotic change and calcification can be visualized in detail using ultrasound (Bell 2020). A sensitivity between 89% and 94% for detecting lymph node metastasis is reported (Griffith, Chan et al. 2000). Furthermore, articles increasingly address the potential use of contrast agent-enhanced ultrasound to predict lymph node metastasis (Wu, Gu et al. 2012, Nielsen Moody, Bull et al. 2017, Mori, Mugikura et al. 2019). However, the assessment of lymph node groups in mediastinum, retroperitoneum and deep pelvis face limitations (Torabi, Aquino et al. 2004).

A fine-needle aspiration cytology is often combined with an ultrasound examination. The procedure is essentially safe, rapid to apply, not expensive and almost painless. An experienced cytopathologist is able to distinguish between a benign or malignant process (Gütz and Knappe 2015).

Magnetic Resonance Tomography (MRI), CT and Positron Emission Tomography-CT (PET-CT) are known to have a relatively high sensitivity and specificity for soft tissue pathologies on one hand, but on the other hand, may induce damage from ionizing radiation or adverse reactions to contrast agent and may require more organizational and monetary effort. Thus, these imaging

modalities are especially suitable for further clarification of ambiguous results and, if necessary, search for a primary cancer (AWMF 2020).

MRI is a sectional image technology as well as CT. The image acquisition works with the support of a strong magnetic field. Unlike CT, MRI does not depend upon the use of X-rays or other ionizing rays. Long-term consequential damages without contrast agents are not known. During an MRI exam, each region (e.g. thorax, abdomen, pelvis) has to be examined individually, with an examination time of approx. 30 minutes each. In MRI, soft tissue structures and nerve tissue are displayed in high resolution. Lymph nodes are assessed by size, shape, number, cystic/necrotic change, enhancement kinetics, flow kinetics, blood volume and microvascular permeability (Bell 2020). Several studies propose a high sensitivity and specificity of MRI to detect affected lymph nodes (Taupitz 2007, Klerkx, Bax et al. 2010, Mizukami, Ueda et al. 2011). However, a whole-body scan to identify a complete lymph node status would require the patient to lay on a narrow table in a 70cm diameter tube without moving for about 1 hour at least.

The general principles of CT have been described in previous chapters. In clinical practice, the size, shape, number, attenuation characteristics, enhancement with contrast, internal architecture, cystic/necrotic change and calcification of lymph nodes are described as typical criteria for characterisation of lymph nodes (Torabi, Aquino et al. 2004, Bell 2020). Although the soft tissue contrast is, in principle, higher in MRI, the contrast of the surrounding tissue for the assessment of lymph nodes is still very good in CT, because lymph nodes are mostly embedded in adipose tissue which presents with negative HU values (approximately -80 HU). Sounding out the additional value of DECT in detecting pathological lymph nodes is part of the present study. Another study compared MRI and DECT for the evaluation of *“Cartilage Invasion by Laryngeal and Hypopharyngeal Squamous Cell Carcinoma”* stating a higher specificity of DECT and similar sensitivity as MRI (Kuno et al. 2018).

PET-CT is a reliable technique in clinical practice for functional imaging of suspicious lesions. For oncological indications, F^{18}-Fluordesoxyglucose (F-FDG) is administered as a common intravenous tracer. Fluorodeoxyglucose (FDG) is taken up by cells with intensified glycolysis. The metabolization of ^{18}F-FDG-6-phosphate leads to a deposit in cells that lack in 6-Glucosephosphatase, predominantly tumor cells. The radioactive isotope of fluorine (^{18}F) attached to

FDG is recorded with an appropriate scanner. Deposits of FDG indicate an increased metabolic activity and tumor vitality (Torabi, Aquino et al. 2004). For various tumor types, more specific tracers are applicable, e.g. ^{11}C-methionin for prostate cancer (Oyama, Akino et al. 2002). Adverse effects arise from radiation exposure during a PET-CT and might cause short- and long-term harm to the patient, in addition, the exam is costly and time-consuming (Nakagawa, Yamada et al. 2008). The fusion of CT and PET exhibits higher sensitivity and specificity to delineate metastatic lymph nodes from healthy ones while preserving a high spatial accuracy (Cronin et al. 2010; Pieterman et al. 2000; Tawfik et al. 2014; Lardinois et al. 2003).

A lymph node biopsy takes a small portion of lymph node tissue for a subsequent histological examination. Extirpation of a lymph node involves a surgical approach requiring intubation or local anaesthesia and an aseptic environment. If examination techniques, named above, indicate a strong suspicion toward a malignant disease, the histological assessment provides information of the underlying disease at the cellular level (e.g. lymphoma, metastatic disease).

2.2 Future Trends and Context of Objectives

Albeit the concept of DECT has been developed in the 1970s and even was mentioned by Hounsfield himself, however clinical applications stalled until the introduction of the dual-source technology in 2006 (Schoepf and Colletti 2012). Since then, the field of DECT research is emerging and results of an increasing number of published studies underpin the numerous potentials uses of this technology (Gong, Wu et al. 2017).

To pave the road towards clinical application for oncological diseases, the measurement of healthy lymph nodes could be a pivotal step. As mentioned in chapter 1.4.3., lymph nodes represent a possible metastatic pathway in many different tumors (e.g. melanoma, tumors of the lung, breast, prostate, head and neck etc.). Some studies have made preliminary investigations on lymph nodes in DECT for oncological diseases by comparing the iodine uptake of different types of metastatic lymph nodes, which might enhance the specificity of the radiologist's judgement in classifying a specific tumor type (Tawfik, Razek et al. 2014, Kato, Uehara et al. 2015, Martin, Czwikla et al. 2018). However, only a few

studies measured the iodine uptake of healthy lymph nodes which might enhance the sensitivity to detect metastatic lymph nodes. None of the studies focused on the comparison of healthy lymph node iodine uptake in different regions in particular. To the best of the authors knowledge, a reference value for healthy lymph nodes has not been introduced, the iodine concentration of different regions has not been compared and no consensus is documented about the way to normalize values in order to account for the interpersonal differences in patients. Parts of the results of this work are already published (Sauter et al. 2020). One article, published later on, shares the similar reasoning and proposes the *"quantitative distribution of iodinated contrast media in body computed tomography"* from a large reference cohort including the measurement of axillary, inguinal, periaortic and mediastinal lymph nodes (Zopfs et al. 2020).

In future, the results may assist radiologists to classify between healthy and pathological lymph nodes even more precisely which may imply an earlier detection of diseases or more accurate staging and prognosis for the patient, especially in the case of an oncological disease.

2.3 Research Questions/Objectives

The following research questions arose and will accompany this thesis:

1. Is a normalization of the absolute mean values of iodine concentration of cervical, axillary and inguinal lymph nodes necessary?

2. Are there regional differences in lymph node iodine uptake?

3. Is there a significant difference in the mean value of normal and abnormal lymph nodes in the context of lymphomata?

3 Methods

3.1 Study Design

According to the study classification for clinical research, the present study belongs to the main group of observational studies and the subgroup of retrospective studies (Latin *retrospectare*, “to look back”). Retrospective, because the patient image datasets were acquired before the start of the study. In contrast, in a prospective study, the data would be collected after the start of the study only. However, the whole process of image analysis in terms of iodine concentration measurements and analysis was performed after the start of the study and patient image datasets, of a date past the study’s start date, were also included as the study continued.

This retrospective study was conducted in accordance with the guidelines of the institutional review board. Due to the retrospective design of the study, informed consent was waived by the institutional review board.

3.2 Study Population

3.2.1 Selection Process

The imaging data was collected from the hospital’s picture archiving and communication system (PACS). In general, scans needed to be

- performed with the hospital's DL-DECT scanner,
- enhanced with iodine-based contrast agent,
- acquired in a portal-venous phase and
- needed to picture the neck, thorax, abdomen/pelvis or a combination.

During the time period from January 2017 to July 2018, 11485 CT-scans on 8356 patients fulfilled the general criterions. From this pool, data sets for study group 1 and 2 were selected according to following steps.

Study cohort 1: Morphological unobtrusive lymph nodes

Data sets with a radiological report claiming lymph nodes as “morphologically normal” were chosen. Reports were written by two radiologists, where one radiologist was a senior physician with a minimum of 6 years of

experience. In order to confirm the diagnosis, a second evaluation for confirmation was performed by two radiologists with 5 and 9 years of experience in CT before study enrollment, respectively.

Furthermore, data sets were aggregated at random to assess for exclusion criteria, if the report mentioned

- a present history of malignancy,
- acute inflammation,
- polytrauma
- or an artefact due to a prosthesis.

A group containing 99 consecutive patients was formed for each region. A total number of 216 patients were selected. In some cases, a patient's data set was used for one, two or three regions, if inclusion and exclusion criteria were being meet respectively (Figure 17).

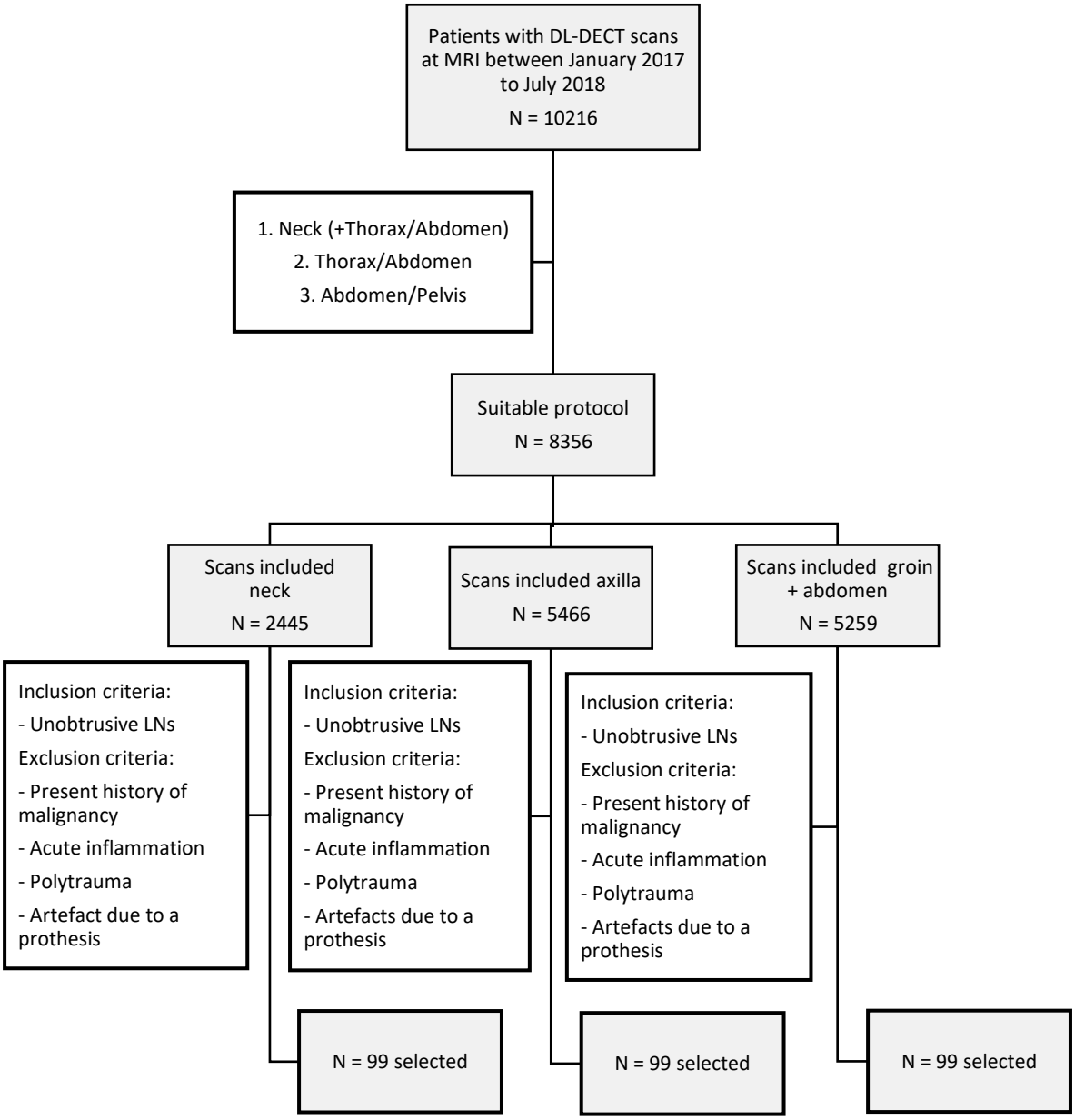

Figure 17: Flowchart of the selection process for study cohort 1. N = number of patients.

Study cohort 2: Lymph nodes with initial diagnosis of lymphoma

For the second cohort, patients with

- initial diagnosis of lymphoma or
- untreated lymphoma

were preselected from the pool of datasets. Due to the distribution of the disease within the patient body, patient's data sets could only be included if at least one or more of the investigated regions were affected.

Exclusion criteria were

- recent treatments for lymphoma (radiotherapy or chemotherapy)
- lymphadenectomy in a respected region.

Again, one group for each of the three regions was composed of the datasets of 56 patients in total. A patient's data set was used for one, two or three regions from the same date.

3.2.2 Characteristics of Study Population 1 and 2

Table 6 and Table 7 display the characteristics of both study populations.

Table 6: Gender and age information of the 216 included patients of study cohort 1. Overall, more men were included. The age and its standard deviation (SD) are consistent in all groups and genders.

	Neck		**Axilla**		**Groin**	
n	99		99		99	
Gender %	Male	Female	Male	Female	Male	Female
	67.7	32.3	67.7	32.3	48.5	51.5
Age in years	55.9	58.2	56.7	58.6	58.7	58.0
SD of age	17.8	14.4	17.4	14.8	19.2	18.5

Table 7: Gender and age information of the 56 included patients of study cohort 2.

	Neck		**Axilla**		**Groin**	
n	47		17		25	
Gender %	Male	Female	Male	Female	Male	Female
	61.7	38.3	52.9	47.1	52.0	48.0
Age in years	56.8	63.6	57.8	63.9	56.2	61.0
SD of age	17.4	11.7	23.5	11.4	19.3	13.5

3.3 Technical Specifics

3.3.1 CT Settings

From September 2016 on, the institution has been using a DL-CT scanner model IQon from Philips Healthcare, produced in Cleveland, USA, with standardized protocols for chest, abdomen, pelvis and neck scans. The CT settings of a scan were: a craniocaudal direction with a pitch of 0.9, a tube voltage of 120 kV and a 64 x 0.625 mm detector configuration (Sauter et al. 2020).

3.3.2 Protocol and Contrast Agent

The investigated datasets include scans that have been following a standard protocol. The standard contrast agent administered at the University Hospital Rechts der Isar is Imeron 400 mg iodine/dl from Bracco Imaging, Konstanz, Germany with a standard dose of 80 ml and flow rate of 2.5 ml/s. For the injection, a dual syringe injection system from Stellant, MEDRAD, Indianola, Pennsylvania, was applied. A 50 ml saline chaser added after the injection of contrast agent ensured the proper circulation of contrast agent. 70 s after the intravenous administration of the contrast agent, portal-venous phase images of thorax, abdomen and pelvis were obtained and saved in DICOM format in PACS.

If the neck was intended to be assessed in addition to a thorax-abdomen-pelvis scan, an extra 70 ml plus a 30 ml saline chaser was administered. Another scan was performed after 70s.

The original protocols of the University Hospital Rechts der Isar for the thorax/abdomen and thorax/abdomen plus neck are provided in the appendix 9.4.

3.3.3 Radiation Exposure

The CTDIvol and DLP of a random sample of seven per region of study cohort 1 were documented for an estimation of the effective radiation dose. The diagnostic reference value of CTDIvol and DLP was generally not exceeded (Table 8) (Bundesamt für Strahlenschutz 2016).

Table 8: Average radiation exposure of the random sample (n=7) with SD of study cohort 1 compared to reference values of the “Announcement of the updated diagnostic reference values for diagnostic and interventional X-ray applications” for “Diagnostic reference values for CT examinations in adults” of the “Bundesamt für Strahlenschutz” (Bundesamt für Strahlenschutz 2016).

	Neck	**Axilla**	**Groin**
CTDIvol [mGy]	10.0 ± 2.3	8.9 ± 3.9	8.0 ± 2.4
Reference CTDIvol [mGy]	15	10	15
DLP [mGy*cm]	310 ± 70	630 ± 260	440 ± 140
Reference DLP [mGy*cm]	330	450	700

3.4 CT Image Analysis

The imaging data set of an included patient was transferred from PACS to a spectral imaging software provided by Philips (IntelliSpace Portal (v. 8.0.2), Philips Healthcare, USA). Viewing preferences were set to axial slices with a thickness of 3 mm and a 512-image matrix (Figure 18). The HU map in soft tissue windowing (see Chapter 1.1.1) and iodine density map (see Chapter 1.2.1) were arranged next to each other and simultaneously investigated (Figure 18). The HU image facilitates orientation and the iodine map allowed measuring of iodine uptake in mg/ml.

Figure 18: Workstation settings of image analysis in IntelliSpace Portal.

3.4.1 Lymph Node Measurement

For study cohort 1, three lymph nodes of the respected regions with a short axis diameter < 10 mm were selected as a short axis diameter >10 mm are more likely to be pathological (Hansen et al. 2018). All measurements were taken from axial sections as shown in Figure 19. The cursor was navigated to the brightest

area within the respected lymph nodes which resembles the maximum iodine uptake. A circular ROI was expanded at this point. The largest possible ROI was drawn, not exceeding a SD equal to or under 0.2. The average value (“Av”) of the iodine mass concentration and the standard deviation (“SA”), depicted in green on the right side, were inserted into an excel table (see Figure 19).

For study cohort 2, up to three affected lymph nodes per region were measured. The ROI was placed in the most homogenous area with a SD equal or under 0.2. For reasons of consistent measurements, the lymph node should be covered as much as possible by the ROI, excluding areas of necrosis (see chapter 5.2.3)

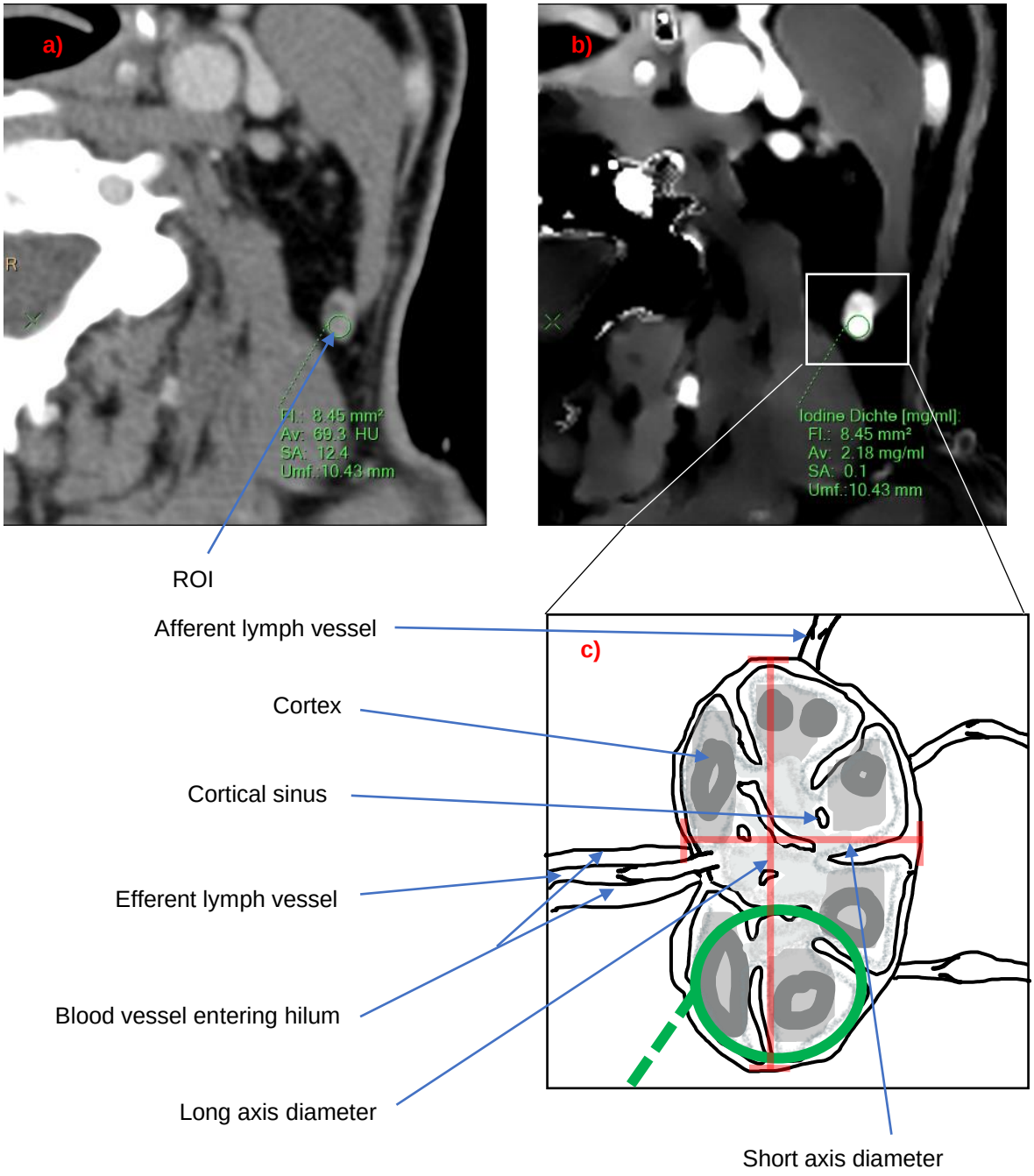

Figure 19: a) The conventional HU map of a healthy lymph node was used for orientation. b) In the iodine map the ROI was placed as shown (green circle). c) Schematic sketch of a healthy lymph node with ROI covering the paracortex and cortex, which tend to have the highest iodine uptake in the portal-venous phase.

3.4.2 Local Tissue Assessment for Normalization

Apart from the iodine concentration of lymph nodes, the iodine concentration of a local artery, vein and muscle for every patient of study cohort 1 and 2 was obtained to test a normalization method. Figure 20 depicts an overview of the location of lymph nodes and the corresponding tissue used for normalization measurements.

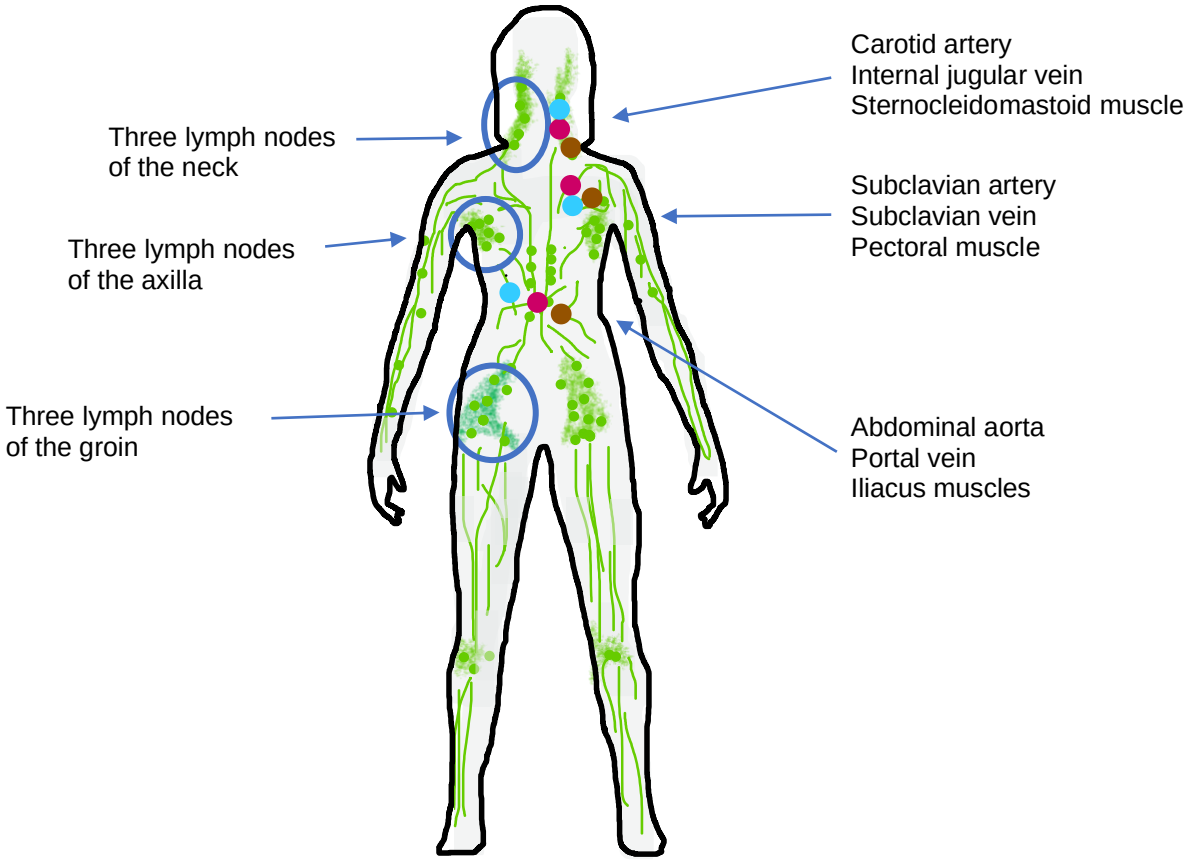

Figure 20: Sketch of lymphatic system with investigated lymph nodes regions (blue circles): cervical, axillary and groin lymph nodes. The colorful dots (red = artery, blue = vein, brown = muscle) represent the locations at the axial landmark for normalization measurements. Modified, based on (Blausen 2014).

Like the measurement of a lymph node, a ROI was placed at the lumen of the local artery and vein and at the maximum iodine uptake of the local muscle of the region. The measurements were taken at consistent axial landmarks (Table 9). The values were listed in an excel table.

Table 9: Lymph node regions with respective examined arteries, veins and muscles and axial landmarks for normalization.

Region	Scan	Artery, landmark	Vein, landmark	Muscle, landmark
Neck	Head/neck	Common carotid artery, right above larynx	Internal jugular vein, right above larynx	Sternocleidomastoid muscle, right above larynx
Axilla	Thorax	Subclavian artery, posterior of clavicula, medial	Subclavian artery, posterior of clavicula, medial	Pectoralis major muscle, same slice
Groin	Abdomen/ pelvis	Abdominal aorta, entrance of portal vein into liver	Portal vein, entrance of vena porta into liver	Iliopsoas muscle, just cranial of iliac spine

3.5 Statistical Analysis

3.5.1 Software

Statistical analysis was conducted with software applications Excel 2019 (Microsoft, Washington, USA) and R (Bell Laboratories, New Jersey, USA). Unless otherwise indicated, all data are given as mean ± SD.

3.5.2 Mathematical Methods

The mean iodine concentration of the three lymph nodes per region and patient was calculated with the goal to reduce the impact of outliers on the SD and set for the basis of all further analysis.

The first research question dealt with the hypothesis, whether the normalization method can reduce individual variation caused by the patient's circulation or examination variables. Equation 4, 5 and 6 were applied to normalize the absolute value to the value of the respective local artery, vein or muscle (Figure 20).

$$\rho_i(nLN) = \rho_i(LN) \times \frac{\rho_i(a)}{\frac{1}{n}\sum_{i=1}^{n}\rho_i(a)}$$

$$\rho_i(nLN) = \rho_i(LN) \times \frac{\rho_i(v)}{\frac{1}{n}\sum_{i=1}^{n}\rho_i(v)}$$

$$\rho_i(nLN) = \rho_i(LN) \times \frac{\rho_i(m)}{\frac{1}{n}\sum_{i=1}^{n}\rho_i(m)}$$

Equation 4, 5 and 6: Normalization method for the artery, vein and muscle. With ρ = mass concentration mg/ml, $_i$ = patient number, LN = mean value of lymph nodes of patient, a = value of artery, v = value of vein, m = value of muscle, nLN = mean value of normalized lymph nodes of patient.

The parameter utilized in this study to assess the normalization method was set as a narrowing in variation compared to the absolute value for the respective region (Välikangas, Suomi, and Elo 2016). The difference in variations was visually determined by inspecting the graphs and mathematically described with the coefficient of variation (CoV) of each normalized mean value. The corresponding p-value was applied as the criterion for significance with a cut-off of > 0.05.

Research question 2 investigates whether a reference value for each region is necessary rather than one for healthy lymph nodes in general. The mean absolute value of the iodine concentration with SD and confidence intervals for study cohort 1 of each region was analyzed for significant difference between the three regions. Both the two-sided Wilcoxon test and the two-sided unpaired t-test were performed.

The “Wilcoxon rank-sum test”, also named “Mann-Whitney U Test”, is used to test for the difference in central tendencies of the medians of unpaired samples (groups of regions) with following conditions.

- Firstly, the sample´s distribution is not necessarily deemed to be normal, but at least ordinally scaled. In contrary, the t-test requires a normal distribution.

- Secondly, the two samples need to be formed by an independent variable for both tests (here: different regions) which is referred to as unpaired samples.

To test for normal distribution the Shapiro-test was applied. However, for big sample sizes the Shapiro-test tends to overweight departures from normal distribution (see chapter 9.3, Figure 28). Furthermore, the “Central limit theorem” stresses that sampling distribution tends to be normal if the sample is large enough (n > 30) (Kwak and Kim 2017). Normal distribution in study cohort 1 can theoretically be presumed regardless of the results of the Shapiro-test. The three regions were considered to be independent variables, not depending on any other variable within the scope of the experiment (see also chapter 5.2.7) (Aris 2012).

Albeit samples are interval scaled and unpaired, not all requirements for the “unpaired t-test” were formally met. Respecting the results of the Shapiro-test, two of three samples were not normally distributed and did not derive from populations with almost identical variance. Therefore the “Wilcoxon rank-sum test” seems most suitable. The latter is referred to as a nonparametric test meaning "prerequisite-free" because of its lower demands on the distribution of the measured values (Wilcoxon 1945; Bortz and Schuster 2011; Sauter et al. 2020). Still, the unpaired t-test can be considered an appropriate option for mathematical analyses of research question 2 as well, when normal distribution is presumed along with the reasoning of the previous paragraph.

The third research question encompasses the analysis of pathological lymph nodes being characterized by a different iodine concentration compared to morphologically unobtrusive lymph nodes. Lymphoma affected patients of study cohort 2 were compared to the reference value derived from study cohort 1. Firstly, lymph nodes of a particular region per patient were averaged. While the average value in the first cohort was based on three lymph nodes, the respective results in cohort 2 have been deduced from one or more lymph nodes per region. Secondly, the absolute mean values were calculated and were compared to the reference value with the Wilcoxon rank-sum test.

- None of the groups of Table 13 are declared to be normally distributed by the Shapiro test, nor by the Central limit Theorem or QQ-Plot.

- Both samples are independent as different patients' groups (here: healthy vs. lymphoma) are compared.

Additionally, ROC analyses and AUC were conducted to display the diagnostic value of the reference value for lymphoma patients.

3.6 Reference and Citations

Pubmed (https://www.ncbi.nlm.nih.gov/pubmed/), PMC (https://www.ncbi.nlm.nih.gov/pmc/), eRef (https://eref.thieme.de), Google.books (https://books.google.com/) served as search engines for literature research. The citation manager EndNote X9 organized all references and linked them to Microsoft word 2019.

In October 2021 the literature search was updated via Medline. Identical or similar search strategies had been used for PMC eReF and Google.scholar.

4 Results

4.1 Research Question 1: Is a Normalization of the Absolute Mean Values of Iodine Concentration of Cervical, Axillary and Inguinal Lymph Nodes Necessary?

For each patient from study cohort 1, the average iodine concentration of three healthy lymph nodes per region were calculated. The absolute mean value of the 99 patients per region, SD and 95%-confidence interval (95%-CI) of the absolute iodine concentration are displayed in Table 10.

For the normalized values, the iodine concentration of the lymph node, the respective local artery, vein and muscle were deployed to Equation 4, 5 and 6 to mathematically eliminate individual variability and test for the best tissue to normalize to (see Table 9). The normalized values to the artery, vein and muscle for every lymph node were calculated and again averaged for each patient per region. The means per region, SD and 95%-CI are summarized in Table 10. Compared to absolute values (grey), consistent higher SD and 95%-CI suggest a greater variation for normalized values.

The effect of normalization on the variation of the individual values (dots) are visualized in

Figure **21**, 21, 22. In each region, the absolute value has the smallest spread. The grey dots are less scattered than the red, blue or brown ones in all three figures. The SD is visualized by the whiskers and is shortest in the group of absolute values (grey dots).

Table 10: Mean of iodine concentration [mg/ml] of the cervical, axillary and inguinal lymph nodes normalized to a local artery, vein and muscle with SD and 95%-confidence interval using Equation 4-6.

	Neck				Axilla				Groin			
Normalized to	Absolute	Artery	Vein	Muscle	Absolute	Artery	Vein	Muscle	Absolute	Artery	Vein	Muscle
Mean	2.09	2.16	2.15	2.07	1.21	1.29	1.32	1.21	1.11	1.11	1.18	1.11
SD	0.44	1.00	0.91	1.13	0.43	0.80	0.95	0.77	0.34	0.43	0.74	0.70
95%-CI	0.09	0.20	0.18	0.22	0.08	0.16	0.19	0.15	0.07	0.09	0.15	0.14

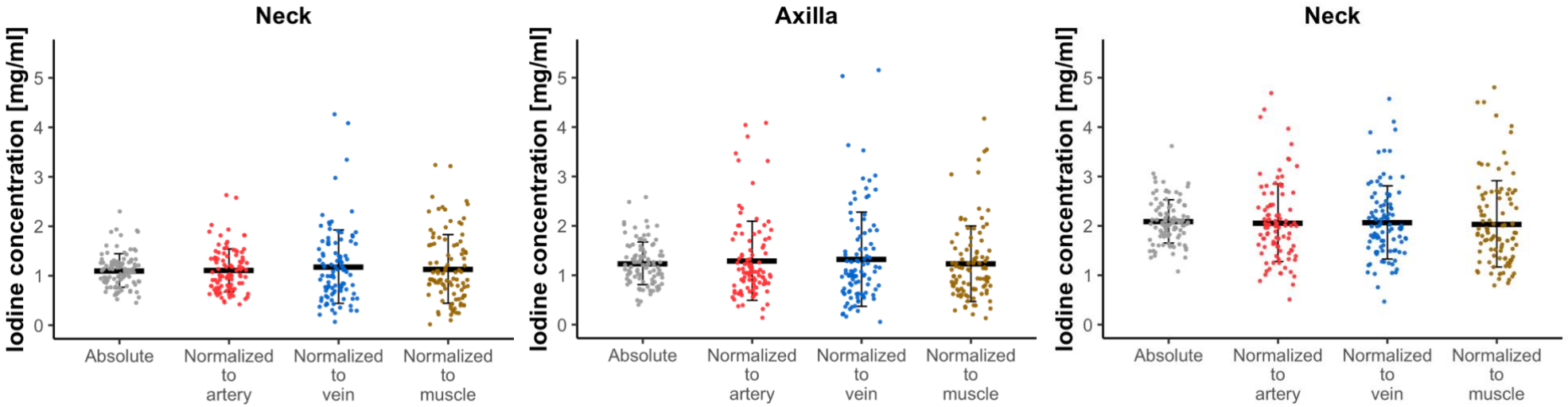

Figure 21, 22 and 23: Individual iodine concentration [mg/ml] values shown for the neck, axilla and groin as dots. Grey represents the absolute value. The normalized values are represented in red for the respective artery, blue for the respective vein and brown for the respective muscle. The mean value is displayed with the thick black line. The whiskers depict the SD.

The visualized findings of

Figure **21**, 21, 22 can also be mathematically described. To test for significant differences in variation, coefficients of variation were calculated (Table 11). A constantly lower CoV for the absolute values compared to the normalized values is observed.

Table 11: Summary of CoVs for absolute and normalized values. While comparing the absolute CoV (black) to the normalized CoVs (red) of the respective row, an increase is observed in all cases.

	Absolute	**Normalized to artery**	**Normalized to vein**	**Normalized to muscle**
Neck	0.21	0.47	0.42	0.55
Axilla	0.35	0.62	0.72	0.64
Groin	0.31	0.39	0.62	0.63

In conclusion, the absolute values had the lowest variation. Normalization did not lead to an overall reduction in variation. Taking variation as an indicator for judging the reliability of normalization, the absolute value appears the more robust reference value. Therefore, the mean values (SD interval) of the absolute iodine concentration in mg/ml for each region is used for all further calculations.

4.2 Research Question 2: Are there Regional Differences in Lymph Node Iodine Uptake?

Research questions 2 examined the necessity of a separate reference value for each region. Table 12 and Figure 24 outline the absolute values. The comparison of means across the groups revealed a 1.7- and 1.9-fold higher iodine concentration for the neck lymph nodes while axilla and groin lymph nodes only differ by a factor of 1.1.

Table 12: Absolute iodine concentration [mg/ml] of morphological unobtrusive lymph nodes in region with SD and 95%-confidence interval.

	Neck	Axilla	Groin
Mean	2.1	1.2	1.1
SD	0.4	0.4	0.3
95%-CI	0.1	0.1	0.1

The Shapairo-Test, Wilcoxon rank-sum test and unpaired t-test were applied. The Shapiro-test was negative ($p > 0.05$) for the deviation from a normal distribution of the neck and positive for the axilla and groin (see R-Script output, Appendix 9.3, Figure 27). Thus, the Wilcoxon rank-sum test was used for all three comparisons, because none of the pairs would have a normal distribution in both cases. Extended analyses regarding the type of distribution revealed strong arguments supporting a normal distribution for all groups. Hence, the t-test was applied. The results with the t-test were compared with the results of the Wilcoxon rank-sum test. No discrepancy in results were found.

Although the values of the axilla and groin resemble one another, a significant difference in central tendencies between all region's medians were calculated (see R-Script output, Appendix 9.3, Figure 27). Along with other reasons, such as different scan protocols for a region, an individual reference value for each region is necessary (see chapter 2.3).

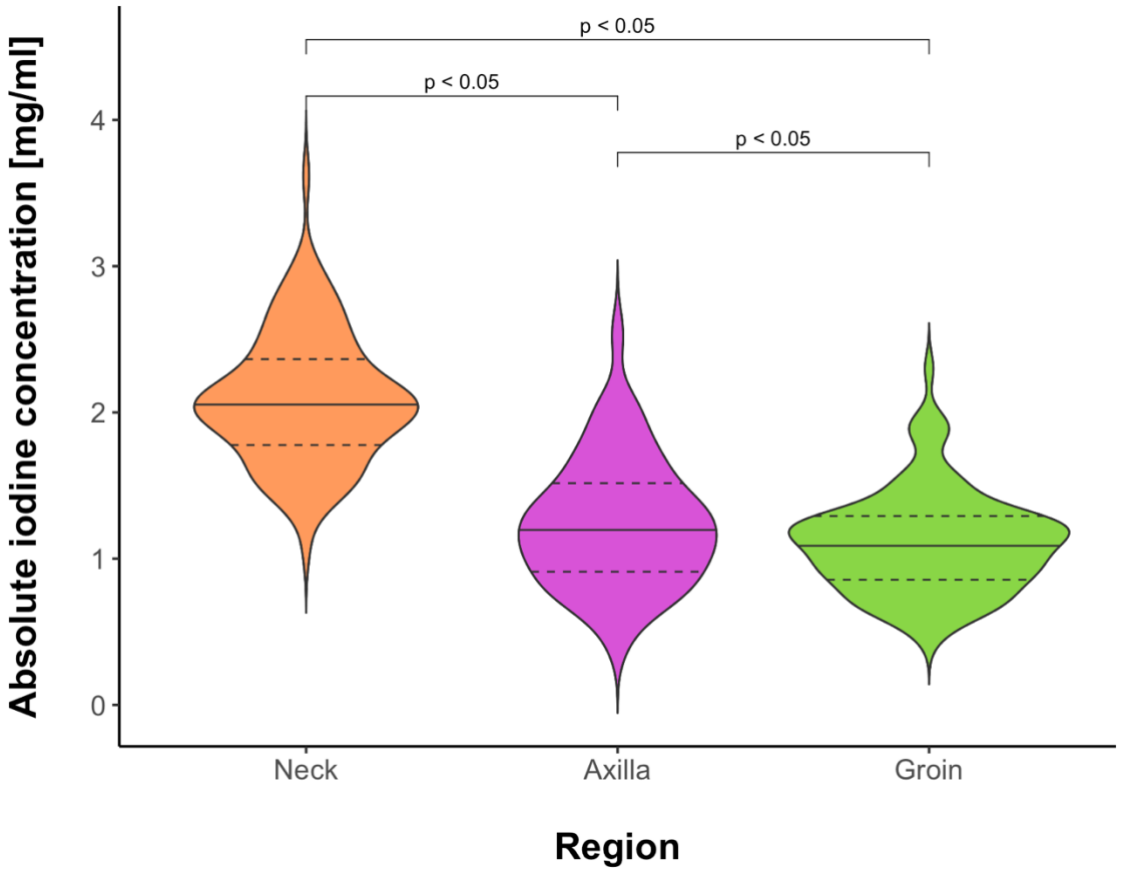

Figure 24: Violin plots of absolute iodine concentration of morphological unobtrusive lymph nodes of the neck (light grey) axilla (grey) groin (dark grey). Middle line represents the mean and the dashed lines the 25% and 75% quartile. Significant difference in means was determined using the Wilcoxon rank-sum test with $p < 0.05$.

4.3 Research Question 3: Is there a Significant Difference in Mean Value of Normal and Abnormal Lymph Nodes in the Context of Lymphomata?

For the third research question, a separate patient cohort (study cohort 2) with pathological lymph nodes were analyzed analogous to study cohort 1. The previous analysis of chapter 4.1 revealed the smallest CoV for the absolute values in comparison to the normalized values. Accordingly, the following results of study cohort 2 focus on the absolute mean values of lymph nodes affected by lymphoma in comparison with the reference iodine concentration values proposed above.

The summary of the absolute mean values is displayed in Table 13. The mean iodine concentration of the neck is higher by factors of 1.2 and 1.1, which is less when compared to study cohort 1. The factor between axilla and groin is 0.9.

Table 13: Absolute iodine concentration [mg/ml] of lymph nodes affected by lymphoma in different regions with SD and 95%-CI.

	Neck	Axilla	Groin
mean	1.8	1.5	1.6
SD	0.4	0.4	0.5
95%-CI	0.1	0.2	0.2

In addition, the distributions and mean value of study cohort 1 and 2 were compared. Here, the Wilcoxon test clearly seems more appropriate than the paired t-test. Since the Wilcoxon test is considered to be non-parametric, great discrepancies in the variation, distribution and sample size (Table 7) between the training (study cohort 1) and test (study cohort 2) groups are acceptable but might limit the informative value (Figure 24, bars). Figure 24 visualizes these considerations, highlighting the difference in variation with box plots and distribution of the individual values with dots.

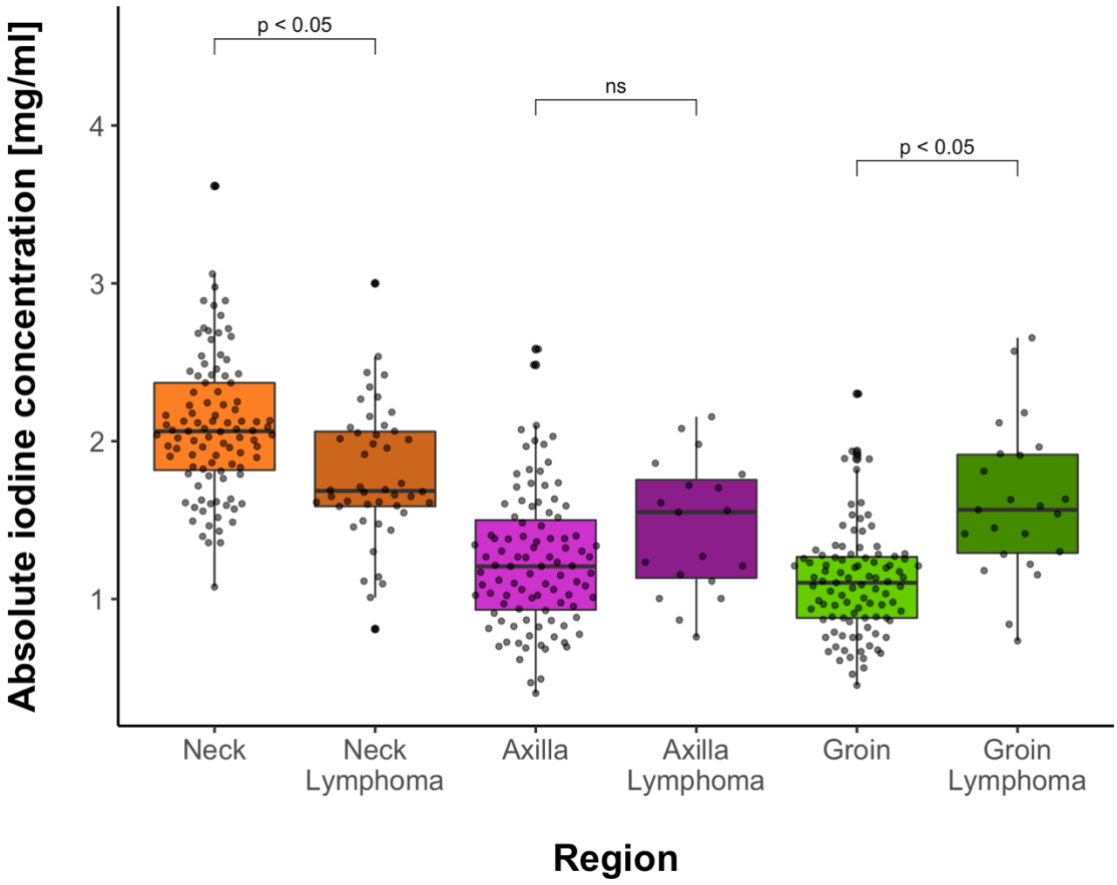

Figure 25: Box plot with 25% quartile and 75% quartile and dot plot of individual absolute iodine concentration of lymph nodes for different anatomical regions and healthy and lymphoma affected lymph nodes. Comparison of iodine concentration between healthy lymph nodes and lymph nodes affected by lymphoma in respected regions with unpaired Wilcoxon test (bars above).

Mathematical analysis revealed opposing tendencies for the neck and groin. For the neck, lymph nodes affected by a lymphoma tend to show a lower uptake of iodine, whereas for the groin and axilla, lymph nodes affected by lymphoma showed a higher iodine uptake compared to healthy lymph nodes.

ROC and AUC are depicted in Figure 26 challenging the diagnostic value of a binary classifier (lymphoma yes or no) with the data of study cohort 1 and 2. The ROC lines of the neck and axilla are close to the diagonal line and have an AUC of < 0,7. The line for the groin has an AUC of 0.82 coming the closest to the optimal value of 1. The optimal threshold for the neck is 1,75 mg/ml, for the axilla 1,55 mg/ml and for the groin 1,28 mg/ml. The answer to research question 3 remains to be elucidated.

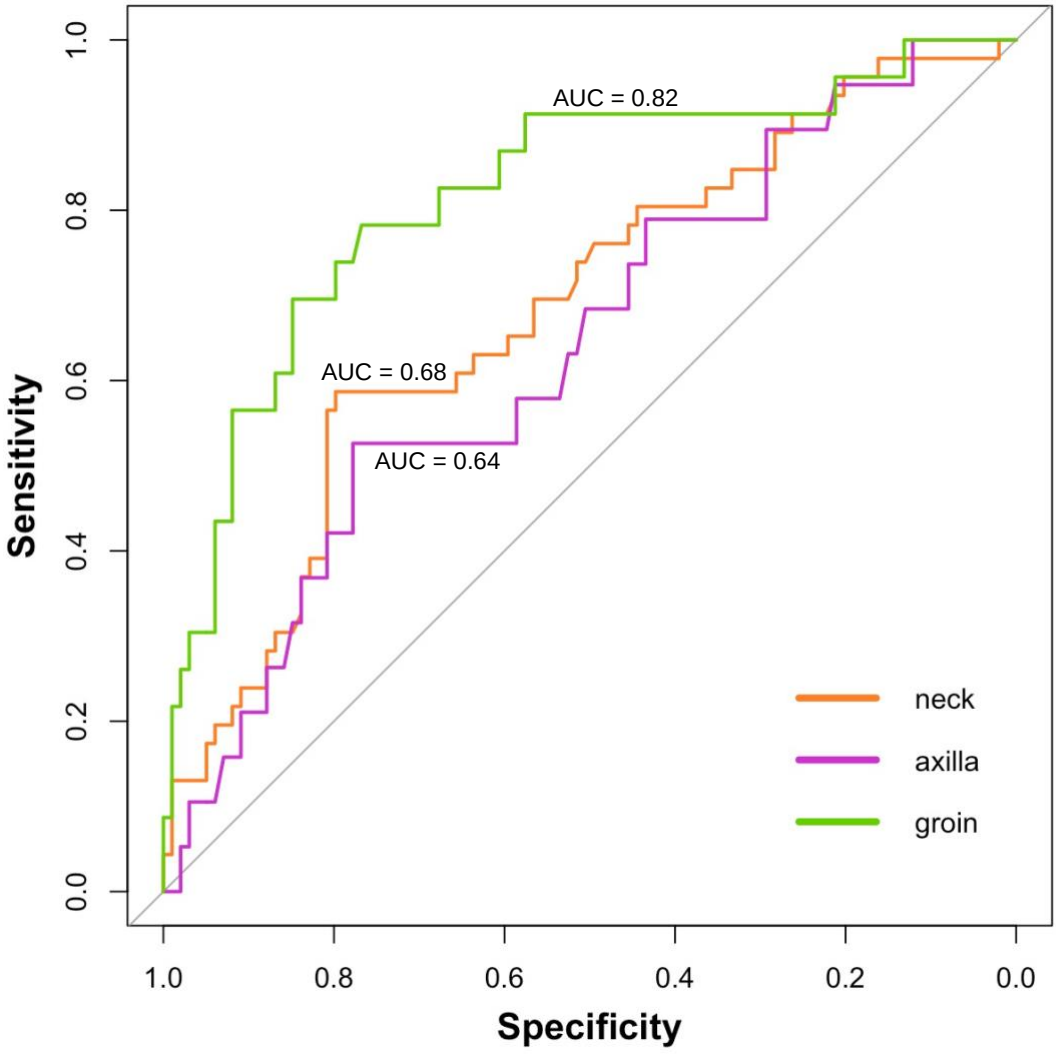

Figure 26: ROC analyses for performance of the binary classifier system (healthy vs. pathologic) for lymph nodes of the neck, axilla and groin as its discrimination threshold is varied. AUC to quantify the discriminative validity of the reference value of the respective region.

5 Discussion

The differentiation between healthy and inflammatory lymph nodes, lymph node metastases and malignant lymphoma occasionally presents a challenge in daily CT evaluation. Limited to the evaluation of size and shape on the basis of HU contrast, current CT reports lack functional statements about lymph nodes (Hansen et al. 2018). Prior studies have highlighted DECT's capability of material characterization. DECT's iodine quantification has already been tested to distinguish between various tumor subtypes, lymph node metastasis or lymphoma and to evaluate the response to chemotherapy (Mileto et al. 2014a; Hellbach et al. 2017; Martin et al. 2018; Rizzo et al. 2018). However, until the initiation of the study, there was no study available which systematically analyzed the averaged iodine uptake of healthy lymph nodes.

5.1 Summary of Main Results

To the best of my knowledge, this retrospective study presents results of systematically evaluating the quantitative iodine uptake of three morphological unobtrusive lymph nodes of the neck, axilla and groin in 99 patients per region for the first time.

In chapter 4.1, a normalization method was tested to account for the interpatient variation of lymph node perfusion but did not reduce the variation of the mean values compared to the absolute iodine concentration values. This study proposes a reference value ± SD for the neck, axilla and groin with 2.1 ± 0.4 mg/ml, 1.2 ± 0.4 mg/ml and 1.1 ± 0.3 mg/ml respectively (Table 12). In chapter 4.2, a significant difference in iodine concentration between the regions is ascertained suggesting the need for a reference value for each location. Finally in chapter 4.3, a ROC graph and AUC values between 0.64 - 0.82 were calculated challenging the diagnostic value of a binary classifier (lymphoma yes or no) with the data of study cohort 1 and 2.

5.2 Discussion of Methods

5.2.1 Study Cohort 1: Study Design, Internal and External Validity

An analysis of the study design, sample composition and population can assess the internal and external validity of the reference values and provide assistance in the interpretation of the results.

Showing internal validity requires a representative sample of a healthy population which is unencumbered by confounding variables. The confirmation of the external validity warrants a sample being generalizable and applicable to the heterogenous group of patients with a justifying indication for a CT scan. These conflicting goals require resolution (Bortz and Schuster 2011).

The study cohort 1 is not perfectly representative of the target population that is entirely healthy which hampers internal validity. The retrospective design encompasses a selection bias as an inherent flaw because image datasets have not been collected entirely at random. The inclusion and exclusion criteria were precisely defined (see Figure 17) and resemble comparable studies (Tawfik et al. 2014; Martin et al. 2018). Two radiologists with 5 and 9 years of professional experience reviewed the selection process of the patient's image datasets. Nonetheless, a patient's image dataset was more likely to be included in the study if the patient had a certain quality, namely a disease or suspicion that confirms a justifying indication for a CT exam. Consequently, the composition of the study's sample diverges from a sample of an ideally healthy target population. For prospective randomized controlled studies, sample bias occurs less frequently because randomization minimizes the statistical insecurity associated with individual variables (Bortz and Schuster 2011). Prospective radiologic CT investigations have rarely been conducted in healthy volunteers, presumably on account of the high radiation exposure. One study from Sweden gathered imaging data sets of 426 volunteers to investigate the short axis of visible healthy lymph nodes, as a parallel project of the prospective Swedish Cardiopulmonary bioimage study (SCAPIS) (Hansen et al. 2018). The informative value of the healthy lymph node's assessment is limited in the Swedish study by the recruiting process being established for a different primary outcome rather than evaluation of healthy lymph nodes. The study cohorts' characteristics, inclusion and exclusion criteria, however, lay down the tracks for a representative sample for the general population's short axis of healthy lymph nodes. Additionally, the

testing conditions, namely the CT protocol, targeted at screening for cardiopulmonary risk factors. There is no optimized and standardized CT protocol to image healthy lymph nodes. All these variables may have an impact on the results for characterization of healthy lymph nodes, representativeness of the sample and the study's internal validity. A possible solution may imply the stratification by subgroups. The results of Zopfs et al. indicate a cohort specific variance and promote a subdivision of reference values by individual variables, like age (Zopfs et al. 2020).

The chosen study design and population of patients of the present study might also partially overcome the previously mentioned limitations, because of a rather high external validity. The application of a reference value for healthy lymph nodes would aim at a study population that is not entirely healthy but diagnosed with or suspected to have a disease. The latter suggests the reference value to be applicable and generalizable among patients with a rectifying indication for a CT exam.

Since there is a justifying indication for each included patient, the underlying medical condition justifying the indication should not interfere with the perfusion structure of the lymph node's tissue for analyzing healthy lymph nodes. A restructuring process of cells and angiogenesis in the T-zone can be a nonspecific response to various stimuli that might influence the iodine uptake in the lymph node (Woznialis et al. 2016). The microanatomically changed lymph node with potentially altered perfusion parameters may have contributed to the reference value by being displayed in an unobtrusive manner in the HU image. The claimed unobtrusive lymph node could display histomorphological differences compared to a healthy lymph node which could be excluded by an extirpation and pathological analysis. However, an extirpation of an unobtrusive lymph node is medically and ethically highly contentious. A significant difference between the reference value and the value of a potentially affected lymph node, especially in early oncological staging, should be confirmed in further studies. It would be more adequate to refer to the proposed reference values as "mean iodine concentration of morphological unobtrusive lymph nodes of a clinical population in HU image" to emphasize the field studies' character.

5.2.2 Study Cohort 1: Sample Size

Being aware about the diversity within the investigated study population, the variation in iodine concentration of healthy lymph nodes might be expanded, due to the diverse composition with various states of health as possible unknown confounders. In order to address this circumstance, the present study aimed for a large sample size of healthy lymph nodes. A larger sample size enhances the statistical power of a potential comparison, here, between the reference value and the iodine concentration of an affected lymph node by broadening the range of potential differences in the population and limiting analytical errors caused by a small number of outliers (Malterud, Siersma, and Guassora 2015). Table 14 summarizes sample characteristics and provides an overview of technical specifics and image analysis of similar studies. One comparable study for cervical lymph nodes, relates to a much smaller sample size. A SD of 0.37 mg/ml results from a sample size of 16 patients with 36 measured lymph nodes indicating similar variation (Tawfik et al. 2014; Martin et al. 2018). The present study computed a SD of 0.4 mg/ml with a sample size of 99 and 216 cervical lymph nodes. Another study investigated 182 abdominal lymph nodes of 60 patients as a control group for abdominal lymphoma with a SD of 0.8 mg/ml (Martin et al. 2018). Zopfs et al. reported a SD of 0.6 to 0.9 mg/ml for axillary and inguinal lymph nodes from a sample size of 571 patients.

However, a very big sample size tends to produce significant differences more likely, because of the enhanced power. Whether the significant difference between the regions of this study is clinically relevant, needs to be judged separately (see chapter 5.3.2, research question 2) (Bortz and Schuster 2011).

5.2.3 Investigated Regions, Image Analysis and ROI Size

Most of the studies only evaluate a single region of lymph nodes (Tawfik et al. 2014; Martin et al. 2018; Kato et al. 2015). A systematic evaluation of three anatomical regions and their comparison had not been done before. Later, an article published by Zopfs et al. includes axillary, inguinal, periaortic and mediastinal lymph nodes. The present study intended to measure the periaortic and mediastinal as well. However, healthy lymph nodes of the neck, axilla and groin proved to be consistently delimitable because of their short axis generally exceeding 5 mm unlike e. g. periaortic and mediastinal lymph nodes (see chapter 5.2.5, “Protocol: Phase, lymph nodes per region, Contrast agent”). In addition, a

small-volume lymph node impedes to place a ROI (see chapter 3.4.1) without enclosing adjacent tissue which promotes partial-volume effects. Therefore, empirically spoken, the inclusion of healthy lymph nodes with a short axis above 5 mm seems reasonable to ensure measurements of high repeatability. In literature, phantom studies that emphasize the accuracy of iodine concentration measurements in DECT chose a consistent ROI size ranging from 1,7 - 12,5 cm^2, but none consider the variability of ROI sizes in clinical practice ascribed to individual anatomy and different investigated organ (Li, Du, and Huang 2015; Ahnfelt et al. ; Ehn et al. 2018; Sellerer et al. 2018). However, the influence of the ROI size on the accuracy of iodine quantification can be derived from studies of other imaging modalities. A study on the effect of ROI size in quantitative brain imaging biomarkers of repeated MRI scans observed a higher rate of change in repeatability measures for smaller ROI sizes (e.g. 36 mm^2) and suggests a method to adjust thresholds for healthy brain tissue depending on the ROI's size (Jafari-Khouzani et al. 2019). Another study on the impact of ROI size in contrast-enhanced ultrasound of canine splenic perfusion constituted a lower CoV for lager ROIs (Morabito et al. 2021). In conclusion, the ROI sizes for iodine concentration should be as large as possible which is limited by the fact that healthy lymph nodes are small organs (in average 5 mm in short axis compared to the liver with up to 16cm in longitudinal axis) (Hansen et al. 2018; Debus, Delorme, and Jenderka 2012). Measuring smaller lymph nodes may compromise the accuracy which limits the assessment of iodine concentration in DECT of lymph nodes in specific regions. However, a short axis exceeding 10 mm proliferation of cells or microvascular modification is more likely (Hansen et al. 2018).

Additionally, all three regions mark major and superficial stations of lymph circulation. One study suggests a difference in the internal distribution of blood vessels between superficial and deep lymph nodes which has not been further investigated (Semeraro and Davies 1986).

5.2.4 Scanner Models

The accuracy of iodine concentration measurements in DECT has been described in several papers. Phantom studies constitute precise measurements for 1 mg/ml and less (Patino et al. 2016; Sellerer et al. 2018; Sommer et al. 2012; Ehn et al. 2018). The CT exams of the present study are consistently conducted

with a DL-DECT scanner, which has the lowest SD for iodine concentration measurements compared to DS-DECT or KVSCT for 20 mGy. While DL-DECT tends to underestimate, DS-DECT is prone to overestimate the iodine concentration which is a potential systematic error limiting the external validity (Sellerer et al. 2018).

5.2.5 Protocol: Phase, Lymph Nodes per Region and Contrast Agent

Compared to other studies the number of lymph nodes per region (three) as well as the phase (portal venous, 60s-80s after injection) are similar (Table 14). The amount of contrast agent administered varies across comparable studies and could explain differences and contradicting tendencies when comparing results between studies (see next chapter 5.3).

5.2.6 Measurements for Normalization

From a physiological point of view, the iodine uptake can differ due to age, gender, body-mass-index, activity with increased heart rate or the application method of the contrast agent. In literature, no standardized procedure has been implemented so far to account for this interindividual variability in the distribution of iodinated contrast agent (Pan et al. 2013; Tawfik et al. 2014; Liu et al. 2015).

Along with the following reasoning, a local artery, vein and muscle as normalization locations were chosen. After being intravenously injected the contrast agent eventually reaches the respective region via the small and large blood circulation through a local artery and returns via local veins to the heart, to be excreted through the kidneys. Measurements of the iodine concentration in vessels reveal information about the actual contrast agents in- and outflow parameters. Therefore, a local artery and vein that are clearly delineable in every scan of the respective region were measured. Kato et al. chose to measure the common iliac artery for normalization of the pelvic lymph nodes. The studies of Zopfs et al., Patel et al. and the present study measured healthy tissue of the lower trunk and normalized to the abdominal aorta. The aorta seems to be an applicable indicator for the actual delivered volume of intravenous contrast agent for an individual patient. However, in the case of lymph node regions distant to the abdominal aorta, the measurement of the iodine concentration in the abdominal aorta might be impossible as the abdominal aorta will not be included into the scan range in all protocols.

The measurement of a local muscle tissue is more independent from the intravascular fluctuation of iodine concentration, but maybe less representative due to the variability of muscle constitution.

5.2.7 Mathematical Analysis

For the second research question, the absolute values of the three regions are analyzed for significant difference, applying the Wilcoxon-test and unpaired t-test. The proposed independence of the groups (here: three regions) is arguable. As stressed in chapter 3.2.1, *"In some cases, one patient's data set was used for one, two or three regions".* Since the body of a patient is a coherent entity and variables that influence perfusion of organs such as cardiac output vary in patients, a complete independence between the groups is not given. Additionally, even though standard protocols were applied, the mean iodine uptake groups depend on the amount of contrast agent given which is different between neck and abdomen/pelvic scans limiting independence between groups. In case of complete independence, one patient image data set could only be included in one group and the same amount of contrast agent needed to be applied for every scan. Although the mathematical accuracy would benefit, the size of the sample would decrease, inevitably together with its representativeness for the target population.

5.2.8 Study Cohort 2: Sample of Patient with Lymphomata

A potential area for clinical implementation of the reference values of the first cohort study was chosen by comparing the suggested reference value of healthy lymph nodes to a sample of 56 patients with initially diagnosed lymphomata. As a frequent malignancy of children and adults, lymphoma often constitute an indication of a whole body CT-staging being less stressful and time consuming for patients than an MRI (Mugnaini and Ghosh 2016, Yang, Luo et al. 2016, Martin, Czwikla et al. 2018).

For study cohort 2, all patients from January 2017 to July 2018 with the initial diagnosis of lymphoma were checked for suitability and selected as described in chapter 3.2.1. Albeit patients with lymphomata seemed to be frequently examined with a CT for primary staging and follow-up examination, the number of included patients appears to be small (n = 56) but still relatively high compared to previous studies. During the selection process no subgroups for

different entities of lymphomata, age or gender were formed which makes it difficult to exclude confounders. Since the sample size is relatively small a breakdown of reference values by variables, like entity etc., would lead to very small sample sizes with higher variability and decreasing representativeness. Further studies need to include more patient’s data sets and stratify by possible confounders.

Table 14: Comparison of methods between studies that investigated the iodine concentration of normal LN (= lymph nodes) in DECT.

	Present study	**(Tawfik et al. 2014)**	**(Kato et al. 2015)**	**(Martin et al. 2018)**	**(Zopfs et al. 2020)**
Regions	Neck, axilla, groin	Neck	Pelvis	Abdomen	Axillary, inguinal, periaortic, mediastinal
Number of patients per region	99, 99, 99	16	17	60	571
Number of LN per patient	3, 3, 3	2	3	3	2
Min or Max. short axis of LN	< 10 mm	> 5mm	> 2mm	< 10mm	?
Scanner models	DL-DECT (IQon, Philips Healthcare, Cleveland, USA)	DS-DECT (SOMATOM Definition Flash; Siemens, Erlangen, Germany)	DS-DECT (SOMATOM Definition Flash; Siemens, Erlangen, Germany)	DS-DECT (SOMATOM Force, Siemens, Erlangen, Germany)	DL-DECT (IQon, Philips Healthcare, Cleveland, USA)
Contrast agent	Imeron, 400 mg iodine/dl (Bracco, Konstanz, Germany)	Imeron, 400 mg iodine/dl (Altana, Konstanz, Germany)	?	Imeron 350 mg iodine/dl (Bracco, Milan, Italy)	Accupaque, 350 mg/ml (GE Healthcare)
Amount of contrast agent per patient	Neck: 80 ml + 70 ml thorax: 80 ml abdomen/pelvis: 80 ml	100 ml, single bolus	?	1.2 ml per kg, max. of 120ml, single bolus	100 ml, single bolus
Phase	Portal-venous, 70s	Portal-venous, 70s	Late-arterial phase, 40s portal-venous, 70s	Portal-venous, 70s	Portal-venous, 50s (threshold of 150HU)
Normalization	$\rho_i(nLN) = \rho_i(LN) \times \frac{\rho_i(a)}{\frac{1}{n}\sum_{i=1}^{n}\rho_i(a)}$	-	$(nLN) = \frac{\rho_i(LN)}{\rho_i(a)}$	-	$(nLN) = \frac{\rho_i(LN)}{\rho_i(a)}$

5.3 Discussion of Results

5.3.1 Research Question 1: Is a Normalization of the Absolute Mean Values of Iodine Concentration of Cervical, Axillary and Inguinal Lymph Nodes Necessary?

The iodine maps in DECT provide a quantitative imaging parameter in mg/ml and no longer dependent on any CT system, tube voltage settings, or underlying tissue HU parameters. Standardized injection protocols of contrast agent and normalization of iodine concentrations may enable quantitative assessment more independent of the individual contrast distribution time which facilitates comparison of quantitative enhancement characteristics in patients undergoing CT exams on different occasions and scanners (Pfeiffer et al. 2018).

The method presented for normalization in this work multiplies the absolute value by the fraction of the value of the tissue for normalization over its average across the group (Equation 4, 5 and 6) which preserves the unit offering a quantitative normalized value in mg/ml. For the first research question, the application of the described normalization method reveals the largest confidence interval for the value normalized to the muscle and smallest for absolute value in all cases. The range of CoV of the normalized values was consistently and significantly larger. Only one comparison of CoV between the absolute and the normalized values of artery lacked significance, but visualisation of this particular data show a more dispersed distribution (Figure 21)(Sauter et al. 2020).

The normalization method does not narrow the variation of mean values raising questions about its drawbacks. Including the average of the tissue for normalization across the group adds variance to the normalized value as an average value brings along its own insecurity. Outliers within values of tissues for normalization are indirectly represented in each value after normalization. In contrast, a simple fraction of the absolute lymph node iodine concentration over the value of the tissue for normalization would exclusively and directly depend on the patient's individual blood circulation variables. The equation of normalization for lymph node iodine concentration in DECT has been repeatedly discussed among following authors with no consensus being found (see Table 14, "Normalization" row).

Kato et al. tested the ratio of the individual iodine concentration of a pelvic lymph node divided by the iodine concentration of the iliac artery but questioned

the need of such normalisation. Liu et al. divided the iodine concentration of cervical lymph node by the one of the carotic artery and found a combination of venous and arterial phase normalized IC to be of value for preoperative evaluation of cervical nodal metastasis (Liu et al. 2015). Patel et al. documented a decrease in variability also using the ratio of the iodine concentration of the investigated tissue and an local artery, but not for lymph nodes, namely for differentiation of renal lesion (Patel et al. 2019). The results of Zopfs et al. suggest a decrease in variation of the mean of lymph node iodine concentration of the trunk when dividing the lymph node iodine concentration value by the abdominal aorta iodine concentration value (Zopfs et al. 2020). The previously mentioned results are repeating the proposal towards an arterial based simple fraction as normalization method (see Table 14). This normalization method forms a ratio of two iodine concentration values (lymph node / abdominal aorta) ending up with relative values without the unit “mg/ml”.

The results of the present study promote the absolute mean value for a reference value and questions a need for normalization. In accordance with Kato et al. and the present study the possibility to derive scientific statements from absolute value for lymph nodes in DECT should be considered.

Retrospective normalization to a local artery, preferably the abdominal aorta, or usage of the absolute value are two options repeatedly described in literature. Another or even additional method to reduce variation of a QIB reference value is to thoroughly normalize the imaging protocol to enhance reproducibility and repeatability, prospectively. In the context of the present study, latter could demand individualised and normalized CT protocols for the assessment of lymph nodes including an amount of contrast agent systematically adjusted to the age and weight of the patient and personalised phase triggered by a certain HU value in the respective local artery after admission of contrast agent etc.. A limitation of normalized CT protocols would be the increased organizational effort contradicting restricted resources of clinical practice.

5.3.2 Research Question 2: Are there Regional Differences in Lymph Node Iodine Uptake?

Based on current literature, it has not been clarified yet, whether one general reference value or a separate reference value for different healthy lymph node regions is requisite. If three different regions of healthy lymph nodes are

investigated within one single study, the mean values of regions can be directly compared with each other due to similar testing conditions and analytical methods. The present results identify a significant difference in mean iodine concentration between the regions and therefore suggests a separate reference value for each region. However, several aspects of this approach appear noteworthy.

The Wilcoxon test indicates a small but significant difference in medians between axillary and inguinal lymph nodes and the intervals greatly overlap. Visually and numerically the mean values seem almost to be equal (1.2 ± 0.4 vs. 1.1 ± 0.3 mg/ml (SD)). The relatively large sample size can promote such a narrow significance. For clinical use, it can be assumed that there is no significant clinical relevance of this minor difference in iodine concentration values for lymph nodes of the axillary and groin.

The iodine concentration of the neck is higher by a factor of up to 1.88 for normal and 1.23 for abnormal lymph nodes compared to a factor of 1.1 and 0.9 for axilla and groin respectively. This circumstance might be ascribed to the amount of contrast agent in full body scans. The two-stage examination stipulates an additionally 70ml of contrast agent for the head after the thorax and abdomen were scanned. A total amount of 150ml contrast agent for a full body scan is applied according to the institutional protocol (see Appendix 9.4, Figure 30). In most of the cases, scans of the neck were combined with the thorax and abdomen scans, but the influence of the protocol or amount of contrast agent needs to be contemplated as it may affect the iodine concentration in a lymph node.

The protocol and amount of contrast agent becomes conspicuous when comparing results among similar studies (Table 14). On one hand, Zopfs et al. reported results for the axillary and inguinal lymph nodes (1.5-2.0 ± 0.6-0.9 mg/ml) coincide with the values of the present study (1.1-1.2 ± 0.3-0.4 mg/ml) using the same scanner model, similar protocol and amount of contrast agent for thorax and abdomen scans (100ml, Accupaque, 350 mg/ml GE Healthcare vs 80ml Imeron, 400 mg iodine/dl Altana, Konstanz, Germany). On the other hand, Tawfik et al. presented absolute values for the neck (2.86 ± 0.37 mg/ml), which diverge significantly from the findings of the present study (2.09 ± 0.44 mg/ml), using a different scanner model and protocol for neck scans. An impact of a different CT protocol with a 100ml (Imeron, 400 mg iodine/dl; Altana, Konstanz,

Germany) single bolus compared to a 150ml (Imeron, 400 mg iodine/dl; Altana, Konstanz, Germany) in two boluses, cannot be excluded. Thus, there is a possibility that a significant difference between the regions can be attributed to specifics of the examination process.

Furthermore, the use of different technical concepts of the DECT technology described in chapter 1.2.2 might play a role as well. The DS-DECT concept applied by Tawfik et al. tends to overestimate the IC, whereas DL-DECT concept tends to slightly underestimate the iodine concentration (see chapter 5.2.4) (Sellerer et al. 2018).

5.3.3 Research Question 3: Is there a Significant Difference in Mean Value of Normal and Abnormal Lymph Nodes in the Context of Lymphomata?

Several studies advocate to utilize the iodine concentration as a perfusion parameter representative for microanatomical changes. Studies published data in favor of this hypothesis stressing DECT applications for oncological imaging regarding tumor characterization and therapy response (Mileto et al. 2014b; Baxa et al. 2016; Deniffel et al. 2019; Jiang et al. 2017; Tawfik et al. 2014; Martin et al. 2018).

Normal lymph nodes of the neck showed an iodine concentration of 2.1 ± 0.4 mg/ml, which significantly departed from lymph nodes affected by lymphoma (1.8 ± 0.4 mg/ml, $p < 0.05$). For the axillary lymph nodes, healthy lymph nodes and lymph nodes affected by lymphoma did not show a significant difference ($p = 0.054$). The difference of the groin lymph nodes was significant, but with an opposite tendency compared to the neck (Figure 24).

Besides the smallness and heterogeneity of study cohort 2, other aspects inferred from current literature may have contributed to inconclusive results. Several studies assume increased number of blood vessels and changes in tumor-associated patterns to be an anatomical correlate for increased iodine uptake in tumor and malignant status of lymph nodes (Liu et al. 2015; Miles 1999; Vogl et al. 2012). In contrast, other studies have demonstrated a decreased iodine uptake for metastatic lymph nodes compared to healthy lymph nodes attributed to unhindered cell proliferation with the displacement of blood vessels (Tawfik, Razek et al. 2014, Kato, Uehara et al. 2015, Liu, Ouyang et al. 2015). Immunohistochemical and morphometric studies on the degree of angiogenesis

within lymph nodes affected by lymphoma showed a dependency on entity, surface protein expression and Ann Arbor stage with an angiogenesis level of normal lymph nodes in between extremes questioning the iodine uptake to be a valid QIB for differentiating between healthy and lymphoma lymph nodes (Korkolopoulou et al. 2005; Woznialis et al. 2016; Mazur et al. 2004; Kadowaki et al. 2005). Besides angiogenesis, the heterogeneous tissue of lymph nodes affected by lymphoma can range from being necrotic to hyperproliferative areas (Yang, Luo et al. 2016). The malignant transformation of the lymph node tissue contains avital cells or areas that are devoid of blood circulation and thus, contrast agent (Sakai, Curtin et al. 2000). When placing and expanding the ROI to the maximum of the lymph node's border, while not exceeding a SD of 0.2 mg/ml, only part of the lymph node is included and may not represent heterogeneity of tissue formation within a lymph node affected by lymphoma. In healthy lymph nodes the placement of a ROI in a consistent manner is possible due to the recurring physiological anatomy (see chapter 3.4.1). For a pathological lymph node, consistent placement of a ROI is difficult to execute due to high variability in tissue structures. In concordance with the result of the present study, an article from Martin et al. reported an insignificant difference between healthy lymph nodes of the abdomen compared to lymph nodes affected by lymphoma (Martin et al. 2018).

These seemingly contradicting hypothesis and results of the previous paragraph are also reflected in ROC and AUC analysis of studies using iodine concentration thresholds as a QIB. A study with a near optimal discriminative threshold up to an AUC of 0.96 was reported for differentiation of vascular and nonvascular renal lesions (Patel et al. 2019). Jiang et al. stated an AUC of 0.875 for therapeutic prediction of chemoradiotherapy of cervical cancer. For lymph nodes, an article of Tawfik et al. reported an AUC of up to 0.923 to delimit metastatic lymph node of squamous cell carcinoma with lower iodine concentration compared to healthy lymph nodes. Well along with the results of the present study, Al-Najami et al. showed an AUC of 0.698 to detect metastatic lymph nodes of rectal carcinoma with a higher iodine concentration compared to benign lymph nodes.

6 Summary and Conclusion

DECT has the capability to quantify tissue compositions by exploiting energy-related attenuation characteristics of different elements. Lymph nodes are secondary lymphatic organs and involved in many processes of the immune system. In diagnostics of malignant diseases, the appearance of lymph nodes is of great relevance for classification and staging which justifies its description as part of every report. A reference value with a high repeatability and reproducibility to implement iodine concentration as a QIB may have the potential to substantially facilitate the assessment of lymph nodes in clinical practice.

Among others, the present study served the purpose to show benefits and limitations of methods for determining reference values for DECT's material decomposition. A prospective study design with specifically defined inclusion criteria for the primary outcome, an even larger cohort size, a standard protocol, a consistent CT system and tube voltage settings would be desirable to optimize internal and external validity on one hand and repeatability and reproducibility of the reference value on the other hand (Table 14)(Bortz and Schuster 2011).

To reduce the inherent variability of in vivo studies, normalization of the iodine concentration needs to be considered with no method agreed upon yet. The normalization method (Equation 4, 5 and 6) used in the present study did not lead to additional benefit. Therefore, following absolute values ± SD are proposed as a reference for the neck, axilla and groin with 2.1 ± 0.4 mg/ml, 1.2 ± 0.4 mg/ml and 1.1 ± 0.3 mg/ml, respectively. Alternatively, a normalization method dividing the absolute value by the aorta or other draining major artery is successfully mentioned in other studies.

The iodine concentration differed significantly between the investigated regions. From an empirical, physiological and technical point of view a separate reference value for each region is reasonable.

A difference in iodine uptake for healthy lymph nodes and lymph nodes affected by lymphoma was recognized. However, a low discriminative validity was seen either attributed to a relatively small and inhomogeneous study group of lymphoma patients, inhomogenous nature of lymphoma affected tissue or to a reference value with unacceptable uncertainty.

7 References

Ahnfelt, Anders, Pär Dahlman, Monica Segelsjö, Mats O Magnusson, and Anders Magnusson. 2021. "Accuracy of iodine quantification using dual-energy computed tomography with focus on low concentrations." *Acta Radiologica* 0 (0):02841851211009462. doi: 10.1177/02841851211009462.

Al-Najami, I., M. J. Lahaye, R. G. H. Beets-Tan, and G. Baatrup. 2017. "Dual-energy CT can detect malignant lymph nodes in rectal cancer." *European Journal of Radiology* 90:81-88. doi: https://doi.org/10.1016/j.ejrad.2017.02.005.

Albrecht, Moritz H., Carlo N. De Cecco, U. Joseph Schoepf, Adam Spandorfer, Marwen Eid, Domenico De Santis, Akos Varga-Szemes, Marly van Assen, Philipp L. von Knebel-Doeberitz, Christian Tesche, Valentina O. Puntmann, Eike Nagel, Thomas J. Vogl, and John W. Nance. 2018. "Dual-energy CT of the heart current and future status." *European Journal of Radiology* 105:110-118. doi: https://doi.org/10.1016/j.ejrad.2018.05.028.

Alkadhi, H., S. Leschka, P. Stolzmann, and H. Scheffel. 2011. *Wie funktioniert CT?*: Springer Berlin Heidelberg.

Alvarez, Robert E, and Albert Macovski. 1976. "Energy-selective reconstructions in x-ray computerised tomography." *Physics in Medicine & Biology* 21 (5):733.

Aris, R. 2012. *Mathematical Modelling Techniques*: Dover Publications.

Ascenti, G., S. Mazziotti, A. Mileto, S. Racchiusa, R. Donato, N. Settineri, and M. Gaeta. 2012. "Dual-source dual-energy CT evaluation of complex cystic renal masses." *AJR Am J Roentgenol* 199 (5):1026-34. doi: 10.2214/ajr.11.7711.

Aumüller, G., G. Aust, A. Conrad, J. Engele, J. Kirsch, and G. Maio. 2020. *Duale Reihe Anatomie*: Thieme.

Bashir, U., and D. Bell. 2012. "Pitch (CT)." Last Modified 05 May 2021, accessed 23 Dec 2021. https://radiopaedia.org/articles/18984.

Baxa, Jan, Tana Matouskova, Gabriela Krakorova, Bernhard Schmidt, Thomas Flohr, Martin Sedlmair, Jiri Bejcek, and Jiri Ferda. 2016. "Dual-phase dual-energy CT in patients treated with erlotinib for advanced non-small cell lung cancer: possible benefits of iodine quantification in response assessment." *European radiology* 26 (8):2828-2836.

Bélisle, C., and G. Sainte-Marie. 1981. "Topography of the deep cortex of the lymph nodes of various mammalian species." *Anat Rec* 201 (3):553-61. doi: 10.1002/ar.1092010311.

Bélisle, C., and G. Sainte-Marie. 1990. "Blood vascular network of the rat lymph node: Tridimensional studies by light and scanning electron microscopy." *American Journal of Anatomy* 189 (2):111-126. doi: 10.1002/aja.1001890203.

Blausen. 2014. "Medical gallery of Blausen Medical 2014." *WikiJournal of Medicine*. doi: 10.15347/wjm/2014.010.

Bortz, J., and C. Schuster. 2011. *Statistik für Human- und Sozialwissenschaftler: Limitierte Sonderausgabe*: Springer Berlin Heidelberg.

Bundesamt für Strahlenschutz. "Ionising radiation, Radiation effects." Bundesamt für Strahlenschutz, accessed 19th October. https://www.bfs.de/EN/topics/ion/effect/effect_node.html.

Bundesamt für Strahlenschutz. "What is the level of natural radiation exposure in Germany?", accessed 18th October 2020. https://www.bfs.de/EN/topics/ion/environment/natural-radiation-exposure/natural-radiation-exposure_node.html;jsessionid=76D7B9437758139B9E27FF0E7DFB01FE.1_cid391.

Bundesamt für Strahlenschutz. 2016. "Bekanntmachung der aktualisierten diagnostischen Referenzwerte für diagnostische und interventionelle Röntgenanwendungen, Tabelle 7." Bundesamt für Strahlenschutz, accessed 26th October 2020. https://www.bfs.de/SharedDocs/Downloads/BfS/DE/fachinfo/ion/drw-roentgen.pdf?__blob=publicationFile&v=9.

Burton, Christiane, Ian Cunningham, and John Mayo. 2015. *Theoretical and experimental comparison of image signal and noise for dual-energy subtraction angiography and conventional x-ray angiography*. Vol. 9412.

Buzug, T.M. 2008. *Computed Tomography: From Photon Statistics to Modern Cone-Beam CT*: Springer Berlin Heidelberg.

Caoili, Elaine M, Melvyn Korobkin, Isaac R Francis, Richard H Cohan, Joel F Platt, N Reed Dunnick, and Kartik I Raghupathi. 2002. "Adrenal masses: characterization with combined unenhanced and delayed enhanced CT." *Radiology* 222 (3):629-633.

Carotti, Marina, Fausto Salaffi, Giacomo Beci, and Andrea Giovagnoni. 2019. "The application of dual-energy computed tomography in the diagnosis of musculoskeletal disorders: a review of current concepts and applications." *La radiologia medica* 124 (11):1175-1183. doi: 10.1007/s11547-019-01015-x.

Cervantes, Guillermo Avendaño. 2016. *Technical Fundamentals of Radiology and CT*: IOP Publishing.

Chen, M. M., F. V. Coakley, A. Kaimal, and R. K. Laros, Jr. 2008. "Guidelines for computed tomography and magnetic resonance imaging use during pregnancy and lactation." *Obstet Gynecol* 112 (2 Pt 1):333-40. doi: 10.1097/AOG.0b013e318180a505.

Cronin, Carmel G, Ronan Swords, Mylene T Truong, Chitra Viswanathan, Eric Rohren, Francis J Giles, Michael O'Dwyer, and John F Bruzzi. 2010. "Clinical utility of PET/CT in lymphoma." *American Journal of Roentgenology* 194 (1):W91-W103.

Cynthia McCollough, Dianna Cody, Sue Edyvean, Rich Geise, Bob Gould, Nicholas Keat, Walter Huda, Phil Judy, Willi Kalender, Mike McNitt-Gray, Rick Morin, Tom Payne, Stanley Stern, Larry Rothenberg. 2008. The Measurement, Reporting, and Managementof Radiation Dose in CT. College Park, MD 20740-3846: Diagnostic Imaging Council CT Committee.

Danad, Ibrahim, Zahi A. Fayad, Martin J. Willemink, and James K. Min. 2015. "New Applications of Cardiac Computed Tomography: Dual-Energy, Spectral, and Molecular CT Imaging." *JACC: Cardiovascular Imaging* 8 (6):710-723. doi: https://doi.org/10.1016/j.jcmg.2015.03.005.

Debus, J., S. Delorme, and K.V. Jenderka. 2012. *Duale Reihe Sonografie*: Thieme.

Deniffel, D., A. Sauter, J. Dangelmaier, A. Fingerle, E. J. Rummeny, and D. Pfeiffer. 2019. "Differentiating intrapulmonary metastases from different primary tumors via quantitative dual-energy CT based iodine concentration and conventional CT attenuation." *Eur J Radiol* 111:6-13. doi: 10.1016/j.ejrad.2018.12.015.

Deutsche Gesellschaft für Unfallchirurgie. 2016. S3 – Leitlinie Polytrauma / Schwerverletzten-Behandlung. Berlin: AWMF, Deutsche Gesellschaft für Unfallchirurgie.

Dorfman, R. E., M. B. Alpern, B. H. Gross, and M. A. Sandler. 1991. "Upper abdominal lymph nodes: criteria for normal size determined with CT." *Radiology* 180 (2):319-322. doi: 10.1148/radiology.180.2.2068292.

Ehn, Sebastian, Thorsten Sellerer, Daniela Muenzel, Alexander A. Fingerle, Felix Kopp, Manuela Duda, Kai Mei, Bernhard Renger, Julia Herzen, Julia Dangelmaier, Benedikt J. Schwaiger, Andreas Sauter, Isabelle Riederer, Martin Renz, Rickmer Braren, Ernst J. Rummeny, Franz Pfeiffer, and Peter B. Noël. 2018. "Assessment of quantification accuracy and image quality of a full-body dual-layer spectral CT system." *Journal of Applied Clinical Medical Physics* 19 (1):204-217. doi: 10.1002/acm2.12243.

Eisenhauer, E. A., P. Therasse, J. Bogaerts, L. H. Schwartz, D. Sargent, R. Ford, J. Dancey, S. Arbuck, S. Gwyther, M. Mooney, L. Rubinstein, L. Shankar, L. Dodd, R. Kaplan, D. Lacombe, and J. Verweij. 2009. "New response

evaluation criteria in solid tumours: Revised RECIST guideline (version 1.1)." *European Journal of Cancer* 45 (2):228-247. doi: https://doi.org/10.1016/j.ejca.2008.10.026.

Elmore, Susan A. 2006. "Histopathology of the Lymph Nodes." *Toxicologic Pathology* 34 (5):425-454. doi: 10.1080/01926230600964722.

Feynman, R.P., R.B. Leighton, and M.L. Sands. 1989. *The Feynman Lectures on Physics: Commemorative Issue*: Addison-Wesley.

Flohr, Thomas. 2011. "Detektoren, Röntgenstrahler und Gantry." In *Wie funktioniert CT? Eine Einführung in Physik, Funktionsweise und klinische Anwendungen der Computertomographie*, 15-22. Berlin, Heidelberg: Springer Berlin Heidelberg.

Fukuda, Takeshi, Yoshinori Umezawa, Shinjiro Tojo, Takenori Yonenaga, Akihiko Asahina, Hidemi Nakagawa, and Kunihiko Fukuda. 2017. "Initial Experience of Using Dual-Energy CT with an Iodine Overlay Image for Hand Psoriatic Arthritis: Comparison Study with Contrast-enhanced MR Imaging." *Radiology* 284 (1):134-142. doi: 10.1148/radiol.2016161671.

George, Elizabeth, Jeremy R. Wortman, Urvi P. Fulwadhva, Jennifer W. Uyeda, and Aaron D. Sodickson. 2017. "Dual energy CT applications in pancreatic pathologies." *The British Journal of Radiology* 90 (1080):20170411. doi: 10.1259/bjr.20170411.

Ghirardelli, M. L., V. Jemos, and P. G. Gobbi. 1999. "Diagnostic approach to lymph node enlargement." *Haematologica* 84 (3):242-7.

Grajo, Joseph R, and Dushyant V Sahani. 2018. "Dual-Energy CT of the Abdomen and Pelvis: Radiation Dose Considerations." *Journal of the American College of Radiology* 15 (8):1128-1132.

Griesinger. 2017. " Leitlinie Lungenkarzinom, nicht-kleinzellig (NSCLC)." Deutsche Gesellschaft für Hämatologie und Medizinische Onkologie (DGHO), accessed 12.10.2017. https://www.onkopedia.com/de/onkopedia/guidelines/lungenkarzinom-nicht-kleinzellig-nsclc/@@guideline/html/index.html.

Hansen, T, M Nilsson, D Lindholm, J Sundström, and J Hedberg. 2018. "Normal radiological lymph node appearance in the thorax." *Diseases of the Esophagus*. doi: 10.1093/dote/doy120.

Healthineers Siemens. 2021. "Photon-counting CT." accessed December 23th 2021. https://www.siemens-healthineers.com/computed-tomography/technologies-and-innovations/photon-counting-ct.

Hellbach, K., A. Sterzik, W. Sommer, M. Karpitschka, N. Hummel, J. Casuscelli, M. Ingrisch, M. Schlemmer, A. Graser, and M. Staehler. 2017. "Dual

energy CT allows for improved characterization of response to antiangiogenic treatment in patients with metastatic renal cell cancer." *Eur Radiol* 27 (6):2532-2537. doi: 10.1007/s00330-016-4597-7.

Hendee, William R., and Michael K. O'Connor. 2012. "Radiation Risks of Medical Imaging: Separating Fact from Fantasy." *Radiology* 264 (2):312-321. doi: 10.1148/radiol.12112678.

Herold, Gerd. 2019. *Innere Medizin : eine vorlesungsorientierte Darstellung : 2019 : unter Berücksichtigung des Gegenstandskataloges für die Ärztliche Prüfung : mit ICD 10-Schlüssel im Text und Stichwortverzeichnis*. Köln: Gerd Herold.

Hilgers, R.D., K.U. Heitmann, P. Bauer, and V. Scheiber. 2013. *Einführung in die Medizinische Statistik*: Springer Berlin Heidelberg.

Hounsfield, Godfrey N. 1980. "Computed medical imaging." *Medical Physics* 7 (4):283-290. doi: 10.1118/1.594709.

Hsu, C. C., G. N. Kwan, D. Singh, J. Pratap, and T. W. Watkins. 2016. "Principles and Clinical Application of Dual-energy Computed Tomography in the Evaluation of Cerebrovascular Disease." *J Clin Imaging Sci* 6:27. doi: 10.4103/2156-7514.185003.

Hünerbein, Ralph. 2017. "Radiologische Verfahren." In *Duale Reihe Radiologie*, edited by Maximilian Reiser, Fritz-Peter Kuhn and Jürgen Debus. Georg Thieme Verlag.

Iwano, S., R. Ito, H. Umakoshi, S. Ito, and S. Naganawa. 2015. "Evaluation of lung cancer by enhanced dual-energy CT: association between three-dimensional iodine concentration and tumour differentiation." *Br J Radiol* 88 (1055):20150224. doi: 10.1259/bjr.20150224.

Jafari-Khouzani, K., K. Paynabar, F. Hajighasemi, and B. Rosen. 2019. "Effect of Region of Interest Size on the Repeatability of Quantitative Brain Imaging Biomarkers." *IEEE Transactions on Biomedical Engineering* 66 (3):864-872. doi: 10.1109/TBME.2018.2860928.

Jafarnejad, M., A. Z. Ismail, D. Duarte, C. Vyas, A. Ghahramani, D. C. Zawieja, C. Lo Celso, G. Poologasundarampillai, and J. E. Moore. 2019. "Quantification of the Whole Lymph Node Vasculature Based on Tomography of the Vessel Corrosion Casts." *Scientific Reports* 9 (1):13380. doi: 10.1038/s41598-019-49055-7.

Jafarnejad, M., M. C. Woodruff, D. C. Zawieja, M. C. Carroll, and J. E. Moore, Jr. 2015. "Modeling Lymph Flow and Fluid Exchange with Blood Vessels in Lymph Nodes." *Lymphat Res Biol* 13 (4):234-47. doi: 10.1089/lrb.2015.0028.

Jiang, C., P. Yang, J. Lei, J. Li, K. Yan, F. Li, R. Yan, and L. Xia. 2017. "The Application of Iodine Quantitative Information Obtained by Dual-Source Dual-Energy Computed Tomography on Chemoradiotherapy Effect Monitoring for Cervical Cancer: A Preliminary Study." *J Comput Assist Tomogr* 41 (5):737-745. doi: 10.1097/RCT.0000000000000603.

Kadowaki, I., R. Ichinohasama, H. Harigae, K. Ishizawa, Y. Okitsu, J. Kameoka, and T. Sasaki. 2005. "Accelerated lymphangiogenesis in malignant lymphoma: possible role of VEGF-A and VEGF-C." *Br J Haematol* 130 (6):869-77. doi: 10.1111/j.1365-2141.2005.05695.x.

Kak, A.C., and M. Slaney. 2001. *Principles of Computerized Tomographic Imaging*: Society for Industrial and Applied Mathematics.

Kalender, W.A. 2021. *Computed Tomography: Fundamentals, System Technology, Image Quality, Applications*: Wiley.

Kato, T., K. Uehara, S. Ishigaki, T. Nihashi, A. Arimoto, H. Nakamura, T. Kamiya, T. Oshiro, T. Ebata, and M. Nagino. 2015. "Clinical significance of dual-energy CT-derived iodine quantification in the diagnosis of metastatic LN in colorectal cancer." *Eur J Surg Oncol* 41 (11):1464-70. doi: 10.1016/j.ejso.2015.08.154.

Kaye, G. W. C. 1934. "Wilhelm Conrad Röntgen: and the Early History of the Roentgen Rays." *Nature* 133 (3362):511-513. doi: 10.1038/133511a0.

Kieranmaher. 2001. "The energy dependence of the Mass Attenuation Coefficient of muscle tissue, File MurhoMuscle.jpg." Wikimedia Commons, accessed 18th October. https://commons.wikimedia.org/wiki/File:MurhoMuscle.jpg.

Koch-Institut, Robert. 2017. Krebs in Deutschland für 2013/2014. Robert Koch-Institut.

Korkolopoulou, P, I Thymara, N Kavantzas, TP Vassilakopoulos, MK Angelopoulou, SI Kokoris, EM Dimitriadou, MP Siakantaris, K Anargyrou, and P Panayiotidis. 2005. "Angiogenesis in Hodgkin's lymphoma: a morphometric approach in 286 patients with prognostic implications." *Leukemia* 19 (6):894.

Kuhn, Norbert, and Thomas M. Klapötke. 2014. "Chemische Stoffe." In *Allgemeine und Anorganische Chemie: Eine Einführung*, edited by Norbert Kuhn and Thomas M. Klapötke, 7-8. Berlin, Heidelberg: Springer Berlin Heidelberg.

Kuno, H., K. Sakamaki, S. Fujii, K. Sekiya, K. Otani, R. Hayashi, T. Yamanaka, O. Sakai, and M. Kusumoto. 2018. "Comparison of MR Imaging and Dual-Energy CT for the Evaluation of Cartilage Invasion by Laryngeal and

Hypopharyngeal Squamous Cell Carcinoma." *AJNR Am J Neuroradiol* 39 (3):524-531. doi: 10.3174/ajnr.A5530.

Kwak, Sang Gyu, and Jong Hae Kim. 2017. "Central limit theorem: the cornerstone of modern statistics." *Korean journal of anesthesiology* 70 (2):144-156. doi: 10.4097/kjae.2017.70.2.144.

Lardinois, D., W. Weder, T. F. Hany, E. M. Kamel, S. Korom, B. Seifert, G. K. von Schulthess, and H. C. Steinert. 2003. "Staging of non-small-cell lung cancer with integrated positron-emission tomography and computed tomography." *N Engl J Med* 348 (25):2500-7. doi: 10.1056/NEJMoa022136.

Lennartz, Simon, Nuran Abdullayev, David Zopfs, Jan Borggrefe, Victor-Frederic Neuhaus, Thorsten Persigehl, Stefan Haneder, and Nils Große Hokamp. 2019. "Intra-individual consistency of spectral detector CT-enabled iodine quantification of the vascular and renal blood pool." *European Radiology* 29 (12):6581-6590. doi: 10.1007/s00330-019-06266-w.

Lennartz, Simon, Markus Le Blanc, David Zopfs, Nils Große Hokamp, Nuran Abdullayev, Kai Roman Laukamp, Stefan Haneder, Jan Borggrefe, David Maintz, and Thorsten Persigehl. 2019. "Dual-energy CT–derived iodine maps: use in assessing pleural carcinomatosis." *Radiology* 290 (3):796-804.

Li, J. H., Y. M. Du, and H. M. Huang. 2015. "Accuracy of dual-energy computed tomography for the quantification of iodine in a soft tissue-mimicking phantom." *J Appl Clin Med Phys* 16 (5):418–426. doi: 10.1120/jacmp.v16i5.5519.

Liu, X., D. Ouyang, H. Li, R. Zhang, Y. Lv, A. Yang, and C. Xie. 2015. "Papillary thyroid cancer: dual-energy spectral CT quantitative parameters for preoperative diagnosis of metastasis to the cervical lymph nodes." *Radiology* 275 (1):167-76. doi: 10.1148/radiol.14140481.

Liu, Xin, Lifeng Yu, Andrew N. Primak, and Cynthia H. McCollough. 2009. "Quantitative imaging of element composition and mass fraction using dual-energy CT: three-material decomposition." *Medical physics* 36 (5):1602-1609. doi: 10.1118/1.3097632.

Lüllmann-Rauch, R., and E. Asan. 2019. *Taschenlehrbuch Histologie*: Thieme.

Lusic, Hrvoje, and Mark W. Grinstaff. 2013. "X-ray-Computed Tomography Contrast Agents." *Chemical Reviews* 113 (3):1641-1666. doi: 10.1021/cr200358s.

Malterud, Kirsti, Volkert Dirk Siersma, and Ann Dorrit Guassora. 2015. "Sample Size in Qualitative Interview Studies: Guided by Information Power."

Qualitative Health Research 26 (13):1753-1760. doi: 10.1177/1049732315617444.

Marin, D., D. T. Boll, A. Mileto, and R. C. Nelson. 2014. "State of the art: dual-energy CT of the abdomen." *Radiology* 271 (2):327-42. doi: 10.1148/radiol.14131480.

Martin, S. S., R. Czwikla, J. L. Wichmann, M. H. Albrecht, L. Lenga, R. H. Savage, C. Arendt, R. Hammerstingl, T. J. Vogl, and B. Kaltenbach. 2018. "Dual-energy CT-based iodine quantification to differentiate abdominal malignant lymphoma from lymph node metastasis." *Eur J Radiol* 105:255-260. doi: 10.1016/j.ejrad.2018.06.017.

Masuhr, K.F., F. Masuhr, and M. Neumann. 2013. *Duale Reihe Neurologie*, *Zerebrale Ischämien*: Thieme.

Maximilian Reiser, Fritz-Peter Kuhn, Jürgen Debus. 2017. *Duale Reihe Radiologie*. 4 ed. Stuttgart: Georg Thieme Verlag.

Mazur, Grzegorz, Tomasz Wróbel, Piotr Dziegiel, Michał Jeleń, Kazimierz Kuliczkowski, and Maciej Zabel. 2004. "Angiogenesis measured by expression of CD34 antigen in lymph nodes of patients with non-Hodgkin's lymphoma." *Folia histochemica et cytobiologica* 42 (4):241-243.

Mehran, Roxana, George D Dangas, and Steven D Weisbord. 2019. "Contrast-associated acute kidney injury." *New England Journal of Medicine* 380 (22):2146-2155.

Menten, Martin J., Martin F. Fast, Simeon Nill, and Uwe Oelfke. 2015. "Using dual-energy x-ray imaging to enhance automated lung tumor tracking during real-time adaptive radiotherapy." *Medical Physics* 42 (12):6987-6998. doi: https://doi.org/10.1118/1.4935431.

Miles, KA. 1999. "Tumour angiogenesis and its relation to contrast enhancement on computed tomography: a review." *European journal of radiology* 30 (3):198-205.

Mileto, A., D. Marin, M. Alfaro-Cordoba, J. C. Ramirez-Giraldo, C. D. Eusemann, E. Scribano, A. Blandino, S. Mazziotti, and G. Ascenti. 2014a. "Iodine quantification to distinguish clear cell from papillary renal cell carcinoma at dual-energy multidetector CT: a multireader diagnostic performance study." *Radiology* 273 (3):813-20. doi: 10.1148/radiol.14140171.

Mileto, Achille, Daniele Marin, Marcela Alfaro-Cordoba, Juan Carlos Ramirez-Giraldo, Christian D. Eusemann, Emanuele Scribano, Alfredo Blandino, Silvio Mazziotti, and Giorgio Ascenti. 2014b. "Iodine Quantification to Distinguish Clear Cell from Papillary Renal Cell Carcinoma at Dual-Energy Multidetector CT: A Multireader Diagnostic Performance Study." *Radiology* 273 (3):813-820. doi: 10.1148/radiol.14140171.

Millner, Michael R., William D. McDavid, Robert G. Waggener, Michael J. Dennis, William H. Payne, and Victor J. Sank. 1979. "Extraction of information from CT scans at different energies." *Medical Physics* 6 (1):70-71. doi: 10.1118/1.594555.

Morabito, Simona, Simona Di Pietro, Luca Cicero, Annastella Falcone, Luigi Liotta, Rosalia Crupi, Giovanni Cassata, and Francesco Macrì. 2021. "Impact of region-of-interest size and location on quantitative contrast-enhanced ultrasound of canine splenic perfusion." *BMC Veterinary Research* 17 (1):271. doi: 10.1186/s12917-021-02973-z.

Mugnaini, Emiliano N, and Nilanjan Ghosh. 2016. "Lymphoma." *Primary Care: Clinics in Office Practice* 43 (4):661-675.

Nakagawa, T., M. Yamada, and Y. Suzuki. 2008. "18F-FDG uptake in reactive neck lymph nodes of oral cancer: relationship to lymphoid follicles." *J Nucl Med* 49 (7):1053-9. doi: 10.2967/jnumed.107.049718.

Ng, S. H., T. C. Yen, C. T. Liao, J. T. Chang, S. C. Chan, S. F. Ko, H. M. Wang, and H. F. Wong. 2005. "18F-FDG PET and CT/MRI in oral cavity squamous cell carcinoma: a prospective study of 124 patients with histologic correlation." *J Nucl Med* 46 (7):1136-43.

Odisio, E. G., M. T. Truong, C. Duran, P. M. de Groot, and M. C. Godoy. 2018. "Role of Dual-Energy Computed Tomography in Thoracic Oncology." *Radiol Clin North Am* 56 (4):535-548. doi: 10.1016/j.rcl.2018.03.011.

Oettle. 2017. " Leitlinie Pankreaskarzinom." Deutsche Gesellschaft für Hämatologie und Medizinische Onkologie (DGHO), accessed 07.11.2017.

Pan, Z., L. Pang, B. Ding, C. Yan, H. Zhang, L. Du, B. Wang, Q. Song, K. Chen, and F. Yan. 2013. "Gastric cancer staging with dual energy spectral CT imaging." *PLoS One* 8 (2):e53651. doi: 10.1371/journal.pone.0053651.

Patel, B. N., F. Vernuccio, M. Meyer, B. Godwin, M. Rosenberg, N. Rudnick, S. Harring, R. Nelson, J. C. Ramirez-Giraldo, A. Farjat, and D. Marin. 2019. "Dual-Energy CT Material Density Iodine Quantification for Distinguishing Vascular From Nonvascular Renal Lesions: Normalization Reduces Intermanufacturer Threshold Variability." *AJR Am J Roentgenol* 212 (2):366-376. doi: 10.2214/ajr.18.20115.

Patino, M., A. Prochowski, M. D. Agrawal, F. J. Simeone, R. Gupta, P. F. Hahn, and D. V. Sahani. 2016. "Material Separation Using Dual-Energy CT: Current and Emerging Applications." *Radiographics* 36 (4):1087-105. doi: 10.1148/rg.2016150220.

Percuoco, Robert. 2014. "Chapter 1 - Plain Radiographic Imaging." In *Clinical Imaging (Third Edition)*, edited by Dennis M. Marchiori, 1-43. Saint Louis: Mosby.

Pfeiffer, D., A. Parakh, M. Patino, A. Kambadakone, E. J. Rummeny, and D. V. Sahani. 2018. "Iodine material density images in dual-energy CT: quantification of contrast uptake and washout in HCC." *Abdom Radiol (NY)* 43 (12):3317-3323. doi: 10.1007/s00261-018-1636-7.

Phan, C. M., A. J. Yoo, J. A. Hirsch, R. G. Nogueira, and R. Gupta. 2012. "Differentiation of Hemorrhage from Iodinated Contrast in Different Intracranial Compartments Using Dual-Energy Head CT." *American Journal of Neuroradiology* 33 (6):1088. doi: 10.3174/ajnr.A2909.

Pieterman, Remge M, John WG van Putten, Jacobus J Meuzelaar, Eduard L Mooyaart, Willem Vaalburg, Gerard H Koëter, Vaclav Fidler, Jan Pruim, and Harry JM Groen. 2000. "Preoperative staging of non–small-cell lung cancer with positron-emission tomography." *New England Journal of Medicine* 343 (4):254-261.

Poste, G. 2011. "Bring on the biomarkers." *Nature* 469 (7329):156-7. doi: 10.1038/469156a.

Prescott, Jeffrey William. 2013. "Quantitative imaging biomarkers: the application of advanced image processing and analysis to clinical and preclinical decision making." *Journal of digital imaging* 26 (1):97-108. doi: 10.1007/s10278-012-9465-7.

Prokop, M., and C. Engelke. 2007. *Ganzkörper-Computertomographie: Spiral- und Multislice-CT ; 328 Tabellen*: Thieme.

Purcell, E.M., and D.J. Morin. 2013. *Electricity and Magnetism*: Cambridge University Press.

Radiological Society of North America. 2020. "RadReport reporting templates." Radiological Society of North America, accessed 2nd November 2020. https://www.rsna.org/en/practice-tools/data-tools-and-standards/radreport-reporting-templates.

Rajendran, Kishore, Martin Petersilka, André Henning, Elisabeth R. Shanblatt, Bernhard Schmidt, Thomas G. Flohr, Andrea Ferrero, Francis Baffour, Felix E. Diehn, Lifeng Yu, Prabhakar Rajiah, Joel G. Fletcher, Shuai Leng, and Cynthia H. McCollough. 2021. "First Clinical Photon-counting Detector CT System: Technical Evaluation." *Radiology* 0 (0):212579. doi: 10.1148/radiol.212579.

Rajiah, P. 2019. "Dual-Energy Computed Tomography in Thoracic Imaging-Current Practices and Utility: Survey of the Society of Thoracic Radiology." *J Thorac Imaging*. doi: 10.1097/rti.0000000000000450.

Rassouli, N., M. Etesami, A. Dhanantwari, and P. Rajiah. 2017. "Detector-based spectral CT with a novel dual-layer technology: principles and

applications." *Insights Imaging* 8 (6):589-598. doi: 10.1007/s13244-017-0571-4.

Rizzo, S., D. Radice, M. Femia, P. De Marco, D. Origgi, L. Preda, M. Barberis, R. Vigorito, G. Mauri, A. Mauro, and M. Bellomi. 2018. "Metastatic and non-metastatic lymph nodes: quantification and different distribution of iodine uptake assessed by dual-energy CT." *Eur Radiol* 28 (2):760-769. doi: 10.1007/s00330-017-5015-5.

Rollvén, Erik, Mirna Abraham-Nordling, Torbjörn Holm, and Lennart Blomqvist. 2017. "Assessment and diagnostic accuracy of lymph node status to predict stage III colon cancer using computed tomography." *Cancer Imaging* 17 (1):3. doi: 10.1186/s40644-016-0104-2.

Romman, Z., I. Uman, Y. Yagil, D. Finzi, N. Wainer, and D. Milstein. 2014. "Detector technology in simultaneous spectral imaging." Philips Healthcare. https://www.documents.philips.com/doclib/enc/fetch/2000/4504/577242/577249/586938/587315/IQon_Spectral_CT_detector_technology_white_paper.pdf.

Ronda CR, Srivastava AM. 2008. "Scintillators. In: Ronda CR, editors. Luminescence: from theory to applications." *Weinheim: Wiley*:105–32.

Rubin, G. D. 2014. "Computed tomography: revolutionizing the practice of medicine for 40 years." *Radiology* 273 (2 Suppl):S45-74. doi: 10.1148/radiol.14141356.

Rutherford, R. A., B. R. Pullan, and I. Isherwood. 1976. "Measurement of effective atomic number and electron density using an EMI scanner." *Neuroradiology* 11 (1):15-21. doi: 10.1007/bf00327253.

Sauter, A. P., S. Ostmeier, J. Nadjiri, D. Deniffel, E. J. Rummeny, and D. Pfeiffer. 2020. "Iodine concentration of healthy lymph nodes of neck, axilla, and groin in dual-energy computed tomography." *Acta Radiol*:284185120903448. doi: 10.1177/0284185120903448.

Schmidt, D., M. Soderberg, M. Nilsson, H. Lindvall, C. Christoffersen, and P. Leander. 2018. "Evaluation of image quality and radiation dose of abdominal dual-energy CT." *Acta Radiol* 59 (7):845-852. doi: 10.1177/0284185117732806.

Schmidt, Dennis. 2019. "Number of computed tomography (CT) scan examinations in Germany from 2005 to 2017." statistica, accessed 23.12.2019. https://www.statista.com/statistics/963439/computed-tomography-scan-examinations-in-germany/.

Seidler, M., B. Forghani, C. Reinhold, A. Perez-Lara, G. Romero-Sanchez, N. Muthukrishnan, J. L. Wichmann, G. Melki, E. Yu, and R. Forghani. 2019.

"Dual-Energy CT Texture Analysis With Machine Learning for the Evaluation and Characterization of Cervical Lymphadenopathy." *Comput Struct Biotechnol J* 17:1009-1015. doi: 10.1016/j.csbj.2019.07.004.

Sellerer, T., P. B. Noel, M. Patino, A. Parakh, S. Ehn, S. Zeiter, J. A. Holz, J. Hammel, A. A. Fingerle, F. Pfeiffer, D. Maintz, E. J. Rummeny, D. Muenzel, and D. V. Sahani. 2018. "Dual-energy CT: a phantom comparison of different platforms for abdominal imaging." *Eur Radiol* 28 (7):2745-2755. doi: 10.1007/s00330-017-5238-5.

Sellerer, Thorsten, Sebastian Ehn, Korbinian Mechlem, Manuela Duda, Michael Epple, Peter B. Noël, and Franz Pfeiffer. 2019. "Quantitative dual-energy micro-CT with a photon-counting detector for material science and non-destructive testing." *PLOS ONE* 14 (7):e0219659. doi: 10.1371/journal.pone.0219659.

Semeraro, D., and J. D. Davies. 1986. "The arterial blood supply of human inguinal and mesenteric lymph nodes." *Journal of anatomy* 144:221-233.

Shefer, Efrat, Ami Altman, Rolf Behling, Raffy Goshen, Lev Gregorian, Yalon Roterman, Igor Uman, Naor Wainer, Yoad Yagil, and Oren Zarchin. 2013. "State of the Art of CT Detectors and Sources: A Literature Review." *Current Radiology Reports* 1 (1):76-91. doi: 10.1007/s40134-012-0006-4.

Silverman, Paul M., Willi A. Kalender, and John D. Hazle. 2001. "Common Terminology for Single and Multislice Helical CT." *American Journal of Roentgenology* 176 (5):1135-1136. doi: 10.2214/ajr.176.5.1761135.

Simons, D., M. Kachelriess, and H. P. Schlemmer. 2014. "Recent developments of dual-energy CT in oncology." *Eur Radiol* 24 (4):930-9. doi: 10.1007/s00330-013-3087-4.

Sommer, C. M., C. B. Schwarzwaelder, W. Stiller, S. T. Schindera, U. Stampfl, N. Bellemann, M. Holzschuh, J. Schmidt, J. Weitz, L. Grenacher, H. U. Kauczor, and B. A. Radeleff. 2012. "Iodine removal in intravenous dual-energy CT-cholangiography: is virtual non-enhanced imaging effective to replace true non-enhanced imaging?" *Eur J Radiol* 81 (4):692-9. doi: 10.1016/j.ejrad.2011.01.087.

Stedman's. 2011. *Stedman's Medical Dictionary*. 7th edition ed: Stedman's.

Stevenson, Angus. 2010. *Oxford dictionary of English*: Oxford University Press, USA.

Stolzmann, Paul. 2011. "Strahlenexposition." In *Wie funktioniert CT? Eine Einführung in Physik, Funktionsweise und klinische Anwendungen der Computertomographie*, 197-200. Berlin, Heidelberg: Springer Berlin Heidelberg.

Stolzmann, Paul, and Robert Götti. 2011. "Protokollparameter und Bildqualität." In *Wie funktioniert CT? Eine Einführung in Physik, Funktionsweise und klinische Anwendungen der Computertomographie*, 23-29. Berlin, Heidelberg: Springer Berlin Heidelberg.

Sullivan, Daniel C., Nancy A. Obuchowski, Larry G. Kessler, David L. Raunig, Constantine Gatsonis, Erich P. Huang, Marina Kondratovich, Lisa M. McShane, Anthony P. Reeves, Daniel P. Barboriak, Alexander R. Guimaraes, Richard L. Wahl, and For the RSNA-QIBA Metrology Working Group. 2015. "Metrology Standards for Quantitative Imaging Biomarkers." *Radiology* 277 (3):813-825. doi: 10.1148/radiol.2015142202.

Tawfik, A. M., A. A. Razek, J. M. Kerl, N. E. Nour-Eldin, R. Bauer, and T. J. Vogl. 2014. "Comparison of dual-energy CT-derived iodine content and iodine overlay of normal, inflammatory and metastatic squamous cell carcinoma cervical lymph nodes." *Eur Radiol* 24 (3):574-80. doi: 10.1007/s00330-013-3035-3.

The Nobel Foundation. "The Nobel Prize in Physics 1901." accessed Fri. 3 Dec 2021. https://www.nobelprize.org/prizes/physics/1901/summary/.

The Nobel Foundation. 1979. "The Nobel Prize in Physiology or Medicine 1979." Nobel Media AB 2020, Last Modified 7th November 2020, accessed 8th November 2020. https://www.nobelprize.org/prizes/medicine/1979/summary/, https://www.nobelprize.org/prizes/medicine/1979/press-release/.

U.S. National library of Medicine. https://clinicaltrials.gov.

Uptodate “lymphadenopathy”. 2019. accessed 13.12.2019. https://www.uptodate.com/contents/image?imageKey=PC%2F77382&topicKey=PC%2F8386&search=lymphadenopathie&rank=1~150&source=see_link&sp=0.

Välikangas, Tommi, Tomi Suomi, and Laura L Elo. 2016. "A systematic evaluation of normalization methods in quantitative label-free proteomics." *Briefings in Bioinformatics* 19 (1):1-11. doi: 10.1093/bib/bbw095.

Van Hedent, S., C. Tatsuoka, S. Carr, K. R. Laukamp, B. Eck, N. Große Hokamp, R. Kessner, P. Ros, and D. Jordan. 2020. "Impact of Patient Size and Radiation Dose on Accuracy and Precision of Iodine Quantification and Virtual Noncontrast Values in Dual-layer Detector CT-A Phantom Study." *Acad Radiol* 27 (3):409-420. doi: 10.1016/j.acra.2019.02.013.

Vogl, Thomas J, Boris Schulz, Ralf W Bauer, Timo Stöver, Robert Sader, and Ahmed M Tawfik. 2012. "Dual-energy CT applications in head and neck imaging." *American Journal of Roentgenology* 199 (5_supplement):S34-S39.

Wilcoxon, Frank. 1945. "Individual Comparisons by Ranking Methods." *Biometrics Bulletin* 1 (6):80-83. doi: 10.2307/3001968.

Willard-Mack, Cynthia L. 2006. "Normal Structure, Function, and Histology of Lymph Nodes." *Toxicologic Pathology* 34 (5):409-424. doi: 10.1080/01926230600867727.

Woznialis, N., B. Gierej, L. Poplawska, M. Ziarkiewicz, E. Wolinska, E. Kulczycka, and B. Ziarkiewicz-Wroblewska. 2016. "Angiogenesis in CD5-positive Diffuse Large B Cell Lymphoma: A Morphometric Analysis." *Adv Clin Exp Med* 25 (6):1149-1155. doi: 10.17219/acem/61427.

www.philips.co.uk. 2017. "IQon Spectral CT." accessed 26.12.2019. https://images.philips.com/is/image/philipsconsumer/1a2be9d266ff4305976fa82c0100a466?wid=470&$pnglarge$.

Xu, J. J., M. Taudorf, P. S. Ulriksen, M. P. Achiam, T. A. Resch, M. B. Nielsen, L. B. Lönn, and K. L. Hansen. 2020. "Gastrointestinal Applications of Iodine Quantification Using Dual-Energy CT: A Systematic Review." *Diagnostics (Basel)* 10 (10). doi: 10.3390/diagnostics10100814.

Yang, L., D. Luo, L. Li, Y. Zhao, M. Lin, W. Guo, and C. Zhou. 2016. "Differentiation of malignant cervical lymphadenopathy by dual-energy CT: a preliminary analysis." *Sci Rep* 6:31020. doi: 10.1038/srep31020.

Yang, Qingxia, Jiajun Hong, Yi Li, Weiwei Xue, Song Li, Hui Yang, and Feng Zhu. 2020. "A novel bioinformatics approach to identify the consistently well-performing normalization strategy for current metabolomic studies." *Briefings in bioinformatics* 21 (6):2142-2152. doi: 10.1093/bib/bbz137.

Zeng, G. 2010. *Medical Image Reconstruction: A Conceptual Tutorial*: Springer Berlin Heidelberg.

Zink, F. E. 1997. "X-ray tubes." *Radiographics : a review publication of the Radiological Society of North America, Inc* 17 (5):1259-1268. doi: 10.1148/radiographics.17.5.9308113.

Zopfs, David, Josefine Graffe, Robert Peter Reimer, Sebastian Schäfer, Thorsten Persigehl, David Maintz, Jan Borggrefe, Stefan Haneder, Simon Lennartz, and Nils Große Hokamp. 2020. "Quantitative distribution of iodinated contrast media in body computed tomography: data from a large reference cohort." *European Radiology*. doi: 10.1007/s00330-020-07298-3.

8 Publications/Conferences

Sauter, A. P., **S. Ostmeier,** J. Nadjiri, D. Deniffel, E. J. Rummeny, and D. Pfeiffer. 2020. "Iodine concentration of healthy lymph nodes of neck, axilla, and groin in dual-energy computed tomography." Acta Radiol:284185120903448. doi: 10.1177/0284185120903448.

Ostmeier, S, A Sauter, D Pfeiffer, E Rummeny, and D Deniffel. 2020. "Referenzwerte für die Iodkonzentration zervikaler, axillärer und inguinaler Lymphknoten im Dual Energy CT." RöFo-Fortschritte auf dem Gebiet der Röntgenstrahlen und der bildgebenden Verfahren.

Sauter, A. P., **S. Ostmeier**, J. Nadjiri, D. Deniffel, E. J. Rummeny, and D. Pfeiffer. 2020. "Iodine concentration of healthy lymph nodes of neck, axilla, and groin in dual-energy computed tomography." European Congress of Radiology 2021, Vienna, digital, Saturday, March 14.

9 Appendix

9.1 List of Figures

9.2 List of Tables

9.3 R-script Outputs

```
> # significant difference between groups with wilcoxon test
>    difw_n_a    <-    wilcox.test(data_wide_H[[1]],    data_wide_H[[2]],
alternative = "two.sided", var.equal = FALSE) # Comparison neck:axilla
with wilcoxon test
>   difw_a_g   <-      wilcox.test(data_wide_H[[1]],   data_wide_H[[3]],
alternative = "two.sided", var.equal = FALSE) # Comparison neck:groin
with wilcoxon test
>   difw_g_g   <-      wilcox.test(data_wide_H[[2]],   data_wide_H[[3]],
alternative = "two.sided", var.equal = FALSE) # Comparison neck:groin
with wilcoxon test
>
> # significant difference between groups with t-test
> dift_n_a <- t.test(data_wide_H[[1]], data_wide_H[[2]], alternative =
"two.sided", var.equal = FALSE) # Comparison neck:axilla with t-test
> dift_a_g <-  t.test(data_wide_H[[1]], data_wide_H[[3]], alternative =
"two.sided", var.equal = FALSE) # Comparison neck:groin with t-test
> dift_g_g <-  t.test(data_wide_H[[2]], data_wide_H[[3]], alternative =
"two.sided", var.equal = FALSE) # Comparison neck:groin with t-test
>
> # Results
> difw_n_a

        Wilcoxon rank sum test with continuity correction

data:  data_wide_H[[1]] and data_wide_H[[2]]
W = 9001, p-value < 2.2e-16
alternative hypothesis: true location shift is not equal to 0

> difw_a_g

        Wilcoxon rank sum test with continuity correction

data:  data_wide_H[[1]] and data_wide_H[[3]]
W = 9463.5, p-value < 2.2e-16
alternative hypothesis: true location shift is not equal to 0

> difw_g_g

        Wilcoxon rank sum test with continuity correction

data:  data_wide_H[[2]] and data_wide_H[[3]]
W = 5811, p-value = 0.02399
alternative hypothesis: true location shift is not equal to 0

> dift_n_a

        Welch Two Sample t-test

data:  data_wide_H[[1]] and data_wide_H[[2]]
```

```
t = 13.738, df = 195.96, p-value < 2.2e-16
alternative hypothesis: true difference in means is not equal to 0
95 percent confidence interval:
 0.7274951 0.9713803
sample estimates:
mean of x mean of y
 2.090919  1.241481

> dift_a_g

        Welch Two Sample t-test

data:  data_wide_H[[1]] and data_wide_H[[3]]
t = 17.688, df = 184.44, p-value < 2.2e-16
alternative hypothesis: true difference in means is not equal to 0
95 percent confidence interval:
 0.8753949 1.0951977
sample estimates:
mean of x mean of y
 2.090919  1.105623

> dift_g_g

        Welch Two Sample t-test

data:  data_wide_H[[2]] and data_wide_H[[3]]
t = 2.4614, df = 185.63, p-value = 0.01475
alternative hypothesis: true difference in means is not equal to 0
95 percent confidence interval:
 0.02696818 0.24474900
sample estimates:
mean of x mean of y
 1.241481  1.105623
```

Figure 27: Output: R script for Shapairo-Test and Wilcoxon-Test.

```
> # Library
> rm(list=ls())
> library(readxl)
> library(dplyr)
> library(iemisc)
> library("car")
> # library(DT) to view data with datatable()
>
> # create a dataset
> setwd
("/Users/sophieostmeier/Desktop/Medizin/DR_Arbeit/doctoral_thesis_tabl
es")
```

```
> healthyLN <- read_excel("Auswertung_gesund_1.xlsx", sheet =
"gemitteltеDaten")
> absoluteLN <- healthyLN %>% select(2,3,4)
> normalizedLNavm <- healthyLN %>% select(5,6,7,8,9,10,11,12,13)
>
> # test for normality
> # absolute values
> nd_a_n <-shapiro.test(absoluteLN$neck) # normal distribution of neck
> nd_a_a <-shapiro.test(absoluteLN$axilla) # normal distribution of
axilla
> nd_a_g <-shapiro.test(absoluteLN$groin) # normal distribution of
groin
> nd_a_n

        Shapiro-Wilk normality test

data:  absoluteLN$neck
W = 0.97846, p-value = 0.1043
```

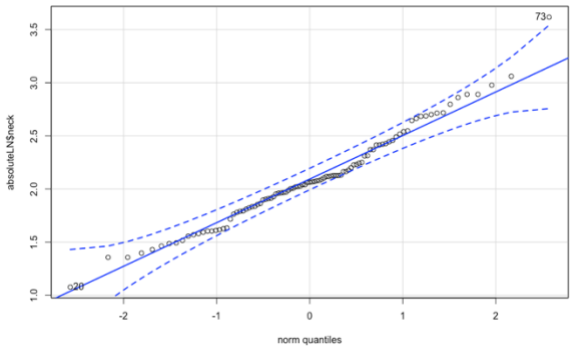


```
> qqPlot(absoluteLN$neck)
[1] 73 20
> nd_a_a

        Shapiro-Wilk normality test

data:  absoluteLN$axilla
W = 0.97227, p-value = 0.03457
```

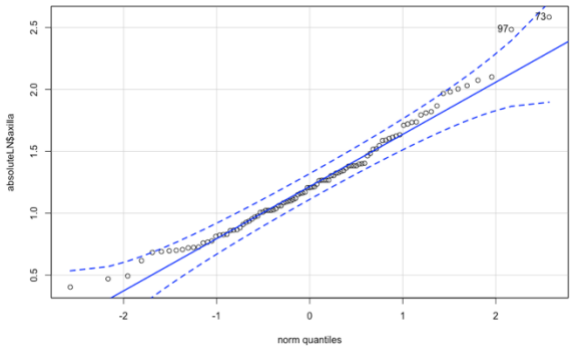


```
> qqPlot(absoluteLN$axilla)
[1] 73 97
> nd_a_g

        Shapiro-Wilk normality test

data:  absoluteLN$groin
W = 0.95935, p-value = 0.003837
```

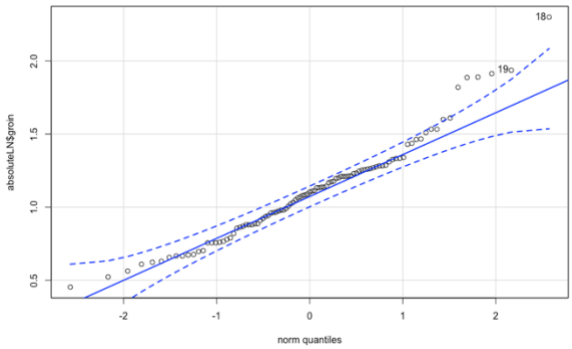


```
> qqPlot(absoluteLN$groin)
[1] 18 19
> # normalized values
> nd_na_n <-shapiro.test(normalizedLNavm$neck_artery) # normal
distribution of neck
> nd_na_a <-shapiro.test(normalizedLNavm$axilla_artery) # normal
distribution of axilla
```

```
> nd_na_g <-shapiro.test(normalizedLNavm$groin_artery) # normal
distribution of groin
> nd_na_n

        Shapiro-Wilk normality test

data:  normalizedLNavm$neck_artery
W = 0.84029, p-value = 5.994e-09

> qqPlot(normalizedLNavm$neck_artery)
[1]  4 73
> nd_na_a
```

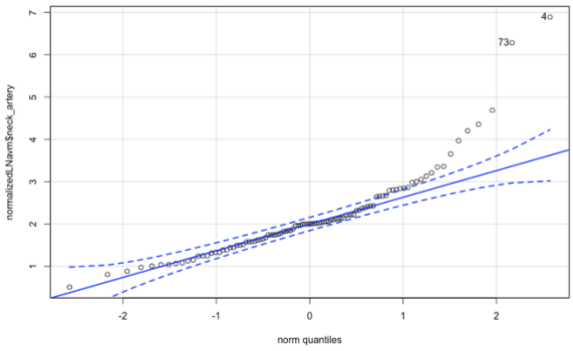


```
        Shapiro-Wilk normality test

data:  normalizedLNavm$axilla_artery
W = 0.83456, p-value = 3.781e-09

> qqPlot(normalizedLNavm$axilla_artery)
[1]  9 97
> nd_na_g
```

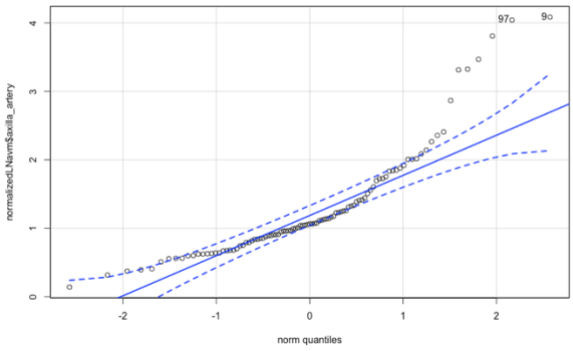


```
        Shapiro-Wilk normality test

data:  normalizedLNavm$groin_artery
W = 0.94083, p-value = 0.000234

> qqPlot(normalizedLNavm$groin_artery)
[1] 76 26
>
> nd_nv_n <-
shapiro.test(normalizedLNavm$neck_vein) #
normal distribution of neck
> nd_nv_a <-shapiro.test(normalizedLNavm$axilla_vein) # normal
distribution of axilla
> nd_nv_g <-shapiro.test(normalizedLNavm$groin_vein) # normal
distribution of groin
> nd_nv_n

        Shapiro-Wilk normality test

data:  normalizedLNavm$neck_vein
W = 0.8685, p-value = 6.861e-08

> qqPlot(normalizedLNavm$neck_vein)
[1]  4 73
> nd_nv_a
```

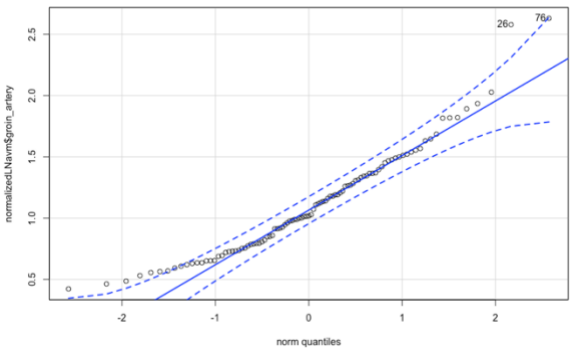

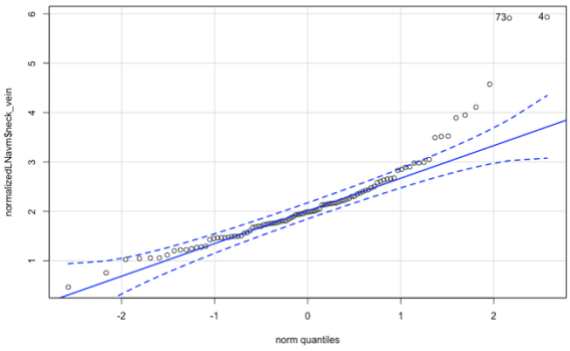

```
        Shapiro-Wilk normality test

data:  normalizedLNavm$axilla_vein
W = 0.85246, p-value = 1.656e-08

> qqPlot(normalizedLNavm$axilla_vein)
[1] 73  9
> nd_nv_g
```

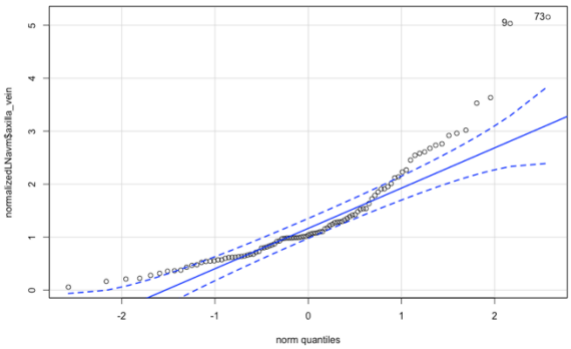


```
        Shapiro-Wilk normality test

data:  normalizedLNavm$groin_vein
W = 0.8767, p-value = 1.478e-07

> qqPlot(normalizedLNavm$groin_vein)
[1] 18 26
>
> nd_nm_n <-
shapiro.test(normalizedLNavm$neck_muscle)
# normal distribution of neck
> nd_nm_a <-
shapiro.test(normalizedLNavm$axilla_muscle) # normal distribution of
axilla
> nd_nm_g <-shapiro.test(normalizedLNavm$groin_muscle) # normal
distribution of groin
> nd_nm_n

        Shapiro-Wilk normality test

data:  normalizedLNavm$neck_muscle
W = 0.78556, p-value = 1.055e-10

> qqPlot(normalizedLNavm$neck_muscle)
[1] 67  4
> nd_nm_a
```

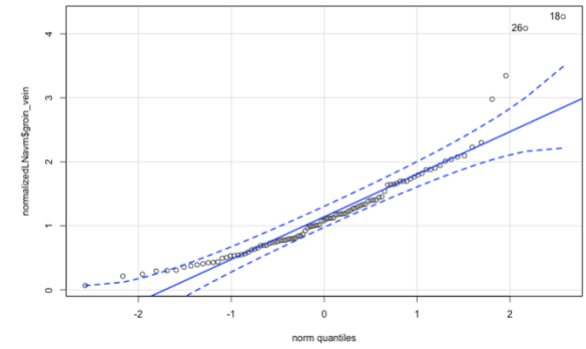

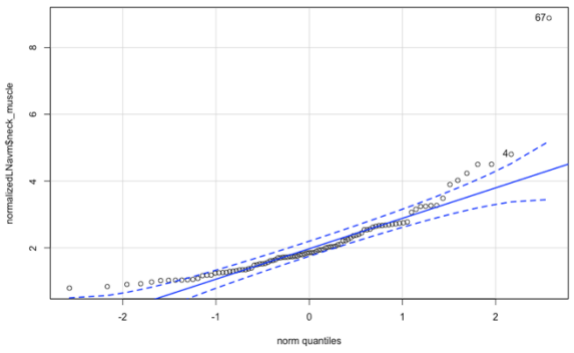


```
        Shapiro-Wilk normality test

data:  normalizedLNavm$axilla_muscle
W = 0.86899, p-value = 7.176e-08

> qqPlot(normalizedLNavm$axilla_muscle)
[1] 63  9
> nd_nm_g

        Shapiro-Wilk normality test

data:  normalizedLNavm$groin_muscle
W = 0.94184, p-value = 0.0002701
```

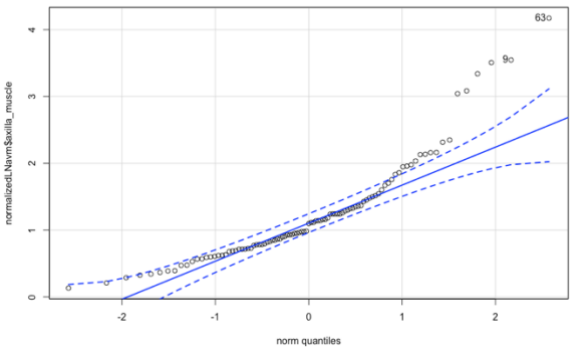

```
> qqPlot(normalizedLNavm$groin_muscle)
[1] 14 91
```

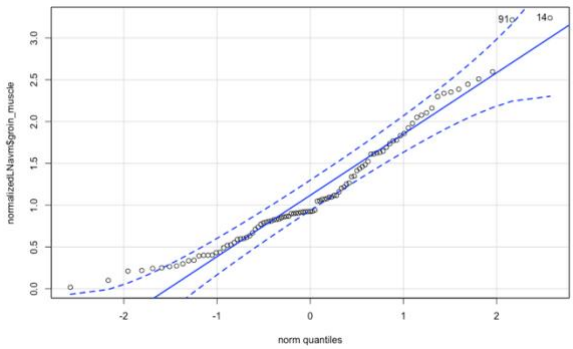

Figure 28: R-Output of Shaiparo-Test indicating a significant departure from normal distribution, QQ-plot visualizing normal distribution and suggesting normal distribution. Besides outliers the majority of dots do not exceed the dashed line corridor. Results comply with the “Central limit Theorem”.

9.4 Hospital protocols “Rechts der Isar“

Ausgedruckt unterliegt das Dokument nicht dem Änderungsdienst

Arbeitsanweisung

Klinikum rechts der Isar — Technische Universität München

CT4 – Thorax Abdomen Becken

Hauptindikation

Staging, Fokussuche

Kontraindikation

Schwangerschaft, Niereninsuffizienz, SD

Patientenvorbereitung

Administrativ (Anmeldung SAP-Bezeichnung der Untersuchung, ggf. Pat.-Aufnahme)
CT → CT-Kombinationen
Unter Bemerkungen: Gewünschter Bereich (z.B. Hals-Thorax-Abdomen-Becken)
Am Vortag (auf Station)
Aktueller Kreatinin- + TSH-Wert
Am Tag der Untersuchung (ggf. auf Station)
Keine

Untersuchungsvorbereitung

Untersuchungsmaterial (ohne Kontrastmittel)
Venöser Zugang
Kontrastmittel
Jodhaltiges KM
Geräteparameter (Voreinstellungen vor Untersuchung)

Patienten – Lagerung
Kopf voran – Rückenlage

Untersuchungsdurchführung (Protokolle Projektionen...)

1. Scanprotokoll: Kombi → Th/Abd/Be dünn
   Th/Abd/Be normal
   Th/Abd/Be dick
   Th/Abd/Be + Hals dünn
   Th/Abd/Be + Hals normal
   Th/Abd/Be + Hals dick
2. Planung: Thoraxapertur bis Beckenkamm
   (bei Th-Becken: inklusive Symphyse)
3. Delay: 70 Sekunden
4. Kontrastmittelprotokoll: Fow 2,5ml/s
   80ml Kontrastmittel + 30ml NaCl
5. Falls erforderlich noch Hals-Protokoll anhängen

Rekonstruktionen:

1. 5.0mm ax WT
2. 3.0mm cor WT
3. 3.0mm sag KF

Patientenversorgung nach der Untersuchung

Patient vom Tisch nehmen

Verhaltenshinweise für Patienten / Nachkontrollen

Keine

Bilddokumentation / -versand ins PACS / Untersuchungsspezifische Besonderheiten Quittierung

siehe MRO_AA_CT1/3-4

Mitgeltende Dokumente

MRO_AA_CT1/3-4
MRO_AA_CT4_Hals
MRO_VA_CT-Kontrastmittelvorbereitung

Erstellt von: N.Meißner — MRO_AA_CT4 ThoraxAbdBecken_190316 — Seite 1 von 1

Figure 29: Original standard protocol for CT scans of the thorax, abdomen and pelvis at University Hospital “Rechts der Isar” in Munich.

Arbeitsanweisung

Klinikum rechts der Isar — Technische Universität München

CT4 – Hals

Hauptindikation

Weichteilveränderungen, Abszess, Tumor, Lymphknoten

Kontraindikation

Schwangerschaft, Niereninsuffizienz, Schilddrüse

Patientenvorbereitung

Administrativ (Anmeldung SAP-Bezeichnung der Untersuchung, ggf. Pat.-Aufnahme)
CT → CT Hals
Am Vortag (auf Station)
Aktueller Kreatinin und TSH-Wert
Am Tag der Untersuchung (ggf. auf Station)
Keine

Untersuchungsvorbereitung

Untersuchungsmaterial (ohne Kontrastmittel)
Venöser Zugang
Kontrastmittel
Jodhaltiges KM
Geräteparameter (Voreinstellungen vor Untersuchung)

Patienten – Lagerung
Kopf voran – Rückenlage

Untersuchungsdurchführung (Protokolle Projektionen...)

1. Scanprotokoll: Hals → Hals pv
2. Planung: Aortenbogen bis Orbitaunterkante
   (Bei MKG-Patienten gesamte NNH abbilden)
3. Caudocraniale Spirale
4. Delay: 70 Sekunden
5. Kontrastmittelprotokoll: Flow 2,5ml/s
   70ml KM + 30ml NaCl

Rekonstruktionen:

1. 3.0mm WT ax
2. 3.0mm WT cor
3. 3.0mm WT sag

Patientenversorgung nach der Untersuchung

Patient vom Tisch nehmen

Verhaltenshinweise für Patienten / Nachkontrollen

Keine

Bilddokumentation / -versand ins PACS / Untersuchungsspezifische Besonderheiten Quittierung

siehe MRO_AA_CT1/3-4

Mitgeltende Dokumente

MRO_AA_CT1/3-4
MRO_VA_CT-Kontrastmittelvorbereitung

Figure 30: Original standard protocol for CT scan of the thorax, abdomen and pelvis plus neck at University Hospital “Rechts der Isar” in Munich.

10 Acknowledgments

I would like to thank Prof. Dr. Daniela Pfeiffer, MHBA for her excellent supervision and guidance through each stage of my doctoral thesis.
I am grateful for the help of PD Dr. med. Andreas Sauter who provided answers to my many questions and assistance in all concerns regarding publications.
Thank you, Julia Dangelmaier, for being my mentor.
My special thanks go to Bernhard Renger and supporters involved in providing me the workstation, patient data and support in case of technical hindrances.
I would also like to thank Prof. Dr. Marcus R. Makowski and all employees of the Institute for Diagnostic and Interventional Radiology at Klinikum Rechts der Isar who contributed to my enjoyment in working on this study.
I would like to especially thank my parents and my brother for their extraordinary support and encouragement both during my studies and beyond.